The Dissertation Committee for Chad Blaine Williams certifies that this is the approved version of the following dissertation:

Characterization of Instability Regimes in the Helimak, a Simple Magnetic Torus

Committee:

Kenneth W. Gentle, Supervisor

Roger Bengtson

Herbert Berk

Boris Breizman

Gary Hallock

Characterization of Instability Regimes in the Helimak, a Simple Magnetic Torus

by

Chad Blaine Williams, B.S.

Dissertation

Presented to the Faculty of the Graduate School
of the University of Texas at Austin
in Partial Fulfillment
of the Requirements
for the Degree of

Doctor of Philosophy

The University of Texas at Austin
May 2017

Acknowledgments

I would be very ungrateful if I didn't acknowledge several important people who have helped me arrive at this point.

First of all, a sincere thank you to those whose help has been so valuable in the lab these several years. Thanks are due to my fellow graduates students, Dr. Ken Liao, Mike Brookman, and Eddie Taylor, for many useful discussions. A huge thank–you as well to Keith Carter for his help with probes, vacuum systems, RF systems, and really anything and everything else that needed to be done around the lab. He was an invaluable resource. Sincere thanks also to Dr. Bill Rowan for useful discussions and advice, as well as the flow measurements data that will be briefly discussed in this dissertation. A further thank–you to our colleagues at WVU, Dr. Mark Koepke and Sam Nogami, for the opportunity to work with them on the baffled probe project.

Dr. Ken Gentle deserves more thanks than I can possibly give him for his help on this journey. He is a nearly bottomless fount of plasma physics knowledge which was essential over and over again. I sincerely appreciate his patience, his encouragement, and his hands–off leadership style that encouraged me to figure things out on my own. This was vital to my growth as a scientist. On the other hand, I also appreciate his critiques and suggestions when I was stuck at various times.

Thanks are also due to various family members and friends for their support over the years. All of the times they asked, "Aren't you done yet?" served as a sort of motivation to finish. I appreciate their encouragement and reassurances. I especially want to mention my mother, Carol Williams, for teaching me how to work hard, since that is exactly what this undertaking required.

On a lighter note, my father, Clark Williams, deserves most of the blame for this whole enterprise. As soon as I found out, decades ago, that he had a Ph.D. (from the University of Texas at Austin, no less), I determined that I had to have one too. I'm grateful that he raised me to be a scientist by encouraging me to ask good questions, find the answers on my own, and love learning. His fascination with the world around him was contagious and I owe my own scientific leanings to the way he raised me.

Closer to home, I never would have made it through graduate school without

the support of my wonderful wife, Leilani. Her patience and love were vital. I also appreciate that, as a scientist, she understands the vicissitudes of experimentation and was thus understanding when things went wrong and excited when they went well. Faraday, my son, has been an absolute joy this past year. I'm not sure what exactly to thank him for, but his very existence has made life that much better.

Finally, I must express my eternal gratitude to my Father in Heaven for all that I am, was, and can become. His guidance has been the single most important factor in my life to this point and I thank Him for the multiplicity of blessings that I have received in my life, including, but not limited to, those involved in my time in graduate school.

Characterization of Instability Regimes in the Helimak, a Simple Magnetic Torus

by

Chad Blaine Williams, Ph.D.

The University of Texas at Austin, 2017

Supervisor: Kenneth W. Gentle

Plasma instability regimes are investigated in the Texas Helimak, a toroidal magnetic confinement device that acts as a physical approximation of the theoretical sheared cylindrical slab. The transition from a regime dominated by the ideal interchange instability to one dominated by drift waves is investigated through experimental measurements of the parallel wavenumber, $k_{\|}$, and other statistics, such as the measurement of applicable power spectra. It is shown that the ideal interchange instability dominates in Helimak plasma at high pitch while drift waves dominate at low pitch. Investigations relative to the effects of an applied bias voltage, both positive and negative, are also carried out. In these it is shown that the application of bias greatly influences both the nature and the amplitude of the turbulence.

Table of Contents

List of Tables **ix**

List of Figures **xiii**

1 Motivation and Introduction **1**

2 Experimental Background **3**

2.1 The Texas Helimak 3

2.1.1 The Helimak Device 3

2.1.2 Helimak Parameters 8

2.1.3 The Helimak and the Tokamak Scrape–off Layer 9

2.2 Langmuir Probes 10

2.2.1 Plasma Sheath 10

2.2.2 Sheath Densities 11

2.2.3 Sheath Currents 13

2.2.4 Probe Use 15

2.3 Statistical and Computational Methods 17

2.3.1 Sampling 18

2.3.2 Fast Fourier Transform 19

2.3.3 Power Spectrum 20

2.3.4 Autocorrelation 21

2.3.5 Cross–Correlation 21

2.3.6 Cross–Spectrum and Significant Cross–Phase 22

2.3.7 Bispectrum and Bicoherence 24

3 Helimak Instabilities **26**

3.1 Ideal Interchange Instability 26

3.2 Drift Waves 29
3.3 Methods of Differentiation Between Drift Waves and Interchange Instabilities 32
3.4 Other Modes Not Considered 34

4 Equilibrium and Turbulent Profiles **36**
4.1 Equilibrium Helimak Data 36
4.1.1 Density 36
4.1.2 Electron Temperature 43
4.1.3 Floating Potential 47
4.2 Helimak Turbulent Amplitude Profiles 52
4.2.1 Grounded Turbulence Profiles 52
4.2.2 Biased Turbulence Profiles 53

5 Experimental Considerations **58**
5.1 Shielding Effects 58
5.2 Magnetic Field Line Alignment 60

6 Grounded Results and Analysis **64**
6.1 Parallel Wavenumber 64
6.2 Perpendicular Wavenumber 68
6.3 Power Spectra 72
6.4 Bicoherence 77

7 Bias Results and Analysis **82**
7.1 Parallel Wavenumber 82
7.2 Perpendicular Wavenumber 88
7.2.1 Low–Field Side 88
7.2.2 High–Field Side 92
7.3 Power Spectra 95
7.3.1 Low–Field Side 95
7.3.2 High–Field Side 99
7.4 Bicoherence 102

8 Conclusion **106**

8.1 Concluding Remarks 106
8.2 Future Work 109

A Table of Pitches and Radii **111**

Bibliography **112**

Vita **114**

List of Tables

2.1 Controllable Helimak variables with typical values 8
2.2 Measured Helimak plasma parameters..... 9
2.3 Comparison of Helimak and DIII–D SOL parameters 9

3.1 Theoretical $\alpha_\perp$ and $\alpha_\parallel$ values for Helimak plasma 33

5.1 Theoretical pitch and shielding at the MPD radius..... 59
5.2 Values of z for the MPD which maximize the cross-correlation at each pitch. 63

6.1 $k_\parallel$ values (m^{-1}) for all pitches and pressures 64
6.2 Connection length as a fraction of parallel wavelength for all pitches 66

7.1 Comparison of λ and pitch at multiple bias voltages (all λ values are given in meters) 87

A.1 Pitch values in centimeters per revolution for all pitches and a collection of radii 111
A.2 Magnetic connection length, L_c, in meters for all pitches and a collection of radii 111

List of Figures

2.1 Cross Section of the Helimak showing dimensions, endplates, and magnetic field punctures 4
2.2 Photograph of the L plates. L1, the innermost plate, is on the right and the radius increases to the left of the photograph. The probes are visible as the small whitish circles 6
2.3 Theoretical semi-infinite plasma set-up for derivation of Langmuir probe characteristics 11
2.4 Sample Langmuir Probe Trace when Swept Voltage is Applied 16
2.5 Sample MDSplus traces as shown by DWScope 18

3.1 Illustration of the interchange, or flute, instability in a cylindrical plasma 26
3.2 Simplified illustration of the Rayleigh–Taylor Instability 27
3.3 Illustration of a drift wave propagating in a cylindrical plasma 30
3.4 Shape of drift wave dispersion relation with Helimak parameters 31

4.1 Density profile from the top of the machine using grounded plates 37
4.2 Density profile from the bottom of the machine using grounded plates .. 37
4.3 Density profile from the top of the machine using plates biased to $-20\,\mathrm{V}$ 38
4.4 Density profile from the bottom of the machine using plates biased to $-20\,\mathrm{V}$ 39
4.5 Average slope for each resistance at large radius, $R > 1.2\,\mathrm{m}$, with and without bias 39
4.6 Density profile from the top of the machine using plates biased to $+10\,\mathrm{V}$ 40
4.7 Density profile from the bottom of the machine using plates biased to $+10\,\mathrm{V}$ 41
4.8 Density profile from the bottom of the machine showing all biases for pitch of $5\,\Omega$ 42

4.9 Density profile from the bottom of the machine showing all biases for pitch of 20 Ω 42
4.10 Electron temperature profile from the top of the machine using grounded plates 43
4.11 Electron temperature profile from the bottom of the machine using grounded plates 44
4.12 Equilibrium (left) and relative (right) electron temperature profiles from the top of the machine using plates biased to −20 V 45
4.13 Equilibrium (left) and relative (right) electron temperature profiles from the bottom of the machine using plates biased to −20 V 45
4.14 Equilibrium (left) and relative (right) electron temperature profiles from the top of the machine using plates biased to +10 V 46
4.15 Equilibrium (left) and relative (right) electron temperature profiles from the bottom of the machine using plates biased to +10 V 47
4.16 Floating potential profile from the top of the machine using grounded plates 48
4.17 Floating potential profile from the bottom of the machine using grounded plates 48
4.18 Equilibrium (left) and relative (right) floating potential profiles from the top of the machine using plates biased to −20 V 49
4.19 Equilibrium (left) and relative (right) floating potential profiles from the bottom of the machine using plates biased to −20 V 49
4.20 Equilibrium (left) and relative (right) floating potential profiles from the top of the machine using plates biased to +10 V 51
4.21 Equilibrium (left) and relative (right) floating potential profiles from the bottom of the machine using plates biased to +10 V 51
4.22 Turbulent amplitudes in the grounded case 53
4.23 Turbulent amplitudes at a bias of −5 V 54
4.24 Turbulent amplitudes at a bias of −20 V 55
4.25 Turbulent amplitudes at a bias of +20 V 56
4.26 Turbulent amplitudes at a bias of 5 Ω 57
4.27 Turbulent amplitudes at a bias of 20 Ω 57

5.1 FFT amplitudes for the probes used in the shielding test 60

5.2 Sample cross–correlation maximization plot for R=15 Ω..... 63

6.1 $k_{\|}$ versus pitch at a pressure of 20 μT..... 65
6.2 $k_{\|}$ versus pitch at a pressure of 40 μT..... 65
6.3 Minimum theoretical value of $k_{\|}$ versus pitch..... 67
6.4 Perpendicular wavenumber vs resistance on the LFS with P=20μT 69
6.5 Perpendicular wavenumber vs resistance on the HFS with P=20μT..... 69
6.6 Dispersion relations for all pitches at radius of 1.345 m with no bias at a pressure of 20 μT..... 70
6.7 Dispersion relations for all pitches at radius of 0.895 m with no bias 71
6.8 Dispersion relations for all pitches at radius of 1.345 m with no bias at a pressure of 40 μT..... 72
6.9 Power spectra for all pitches at radius of 0.82 m and P = 40 μT 74
6.10 Power spectra for all pitches at radius of 1.305 m and P = 40 μT..... 75
6.11 Power spectra for all pitches at radius of 1.305 m and P = 20 μT..... 76
6.12 Bicoherence for a pitch of 5 Ω at 20 μT in the grounded case. 79
6.13 Bicoherence for a pitch of 25 Ω at 20 μT in the grounded case. 79
6.14 Bicoherence for a pitch of 5 Ω at 40 μT in the grounded case..... 80
6.15 Bicoherence for a pitch of 25 Ω at 40 μT in the grounded case. 80

7.1 Parallel wavenumber with −5 V of applied bias 83
7.2 Parallel wavenumber with −20 V of applied bias 83
7.3 Parallel wavenumber with +20 V of applied bias 84
7.4 Parallel wavenumber at a pitch of 3.3 Ω versus bias 85
7.5 Parallel wavenumber at a pitch of 20 Ω versus bias 86
7.6 Perpendicular wavenumber on the LFS vs resistance at several radii with Bias = −20 V and P = 20μT 89
7.7 Perpendicular wavenumber on the LFS vs resistance at several radii with Bias = +20 V and P = 20μT 89
7.8 Difference between biased and grounded perpendicular wavenumbers on the LFS vs pitch at several radii with P = 20μT 90
7.9 Normalized theoretical growth rate of drift waves on the LFS vs pitch at several radii with P = 20μT..... 91

7.10 Perpendicular wavenumber on the HFS vs resistance at several radii with Bias = −20 V and P = 20μT 92
7.11 Perpendicular wavenumber on the HFS vs resistance at several radii with Bias = +20 V and P = 20μT 93
7.12 Difference between biased and grounded perpendicular wavenumbers on the HFS vs resistance at several radii with P = 20μT 94
7.13 Difference between biased and grounded perpendicular wavenumbers on the LFS vs resistance at several radii with P = 20μT..... 94
7.14 Power spectra for all pitches at radius of 1.305 m and P = 20 μT with −40 V of applied bias 96
7.15 Power spectra for all pitches at radius of 1.305 m and P = 20 μT with +10 V of applied bias 98
7.16 Power spectra for all pitches at radius of 0.82 m and P = 20 μT with −40 V of applied bias 100
7.17 Power spectra for all pitches at radius of 0.82 m and P = 20 μT with +20 V of applied bias 101
7.18 Bicoherence for a pitch of 5 Ω at 20 μT with −40 V of bias..... 103
7.19 Bicoherence for a pitch of 25 Ω at 20 μT with −40 V of bias. 103
7.20 Bicoherence for a pitch of 5 Ω at 20 μT with +20 V of bias..... 104
7.21 Bicoherence for a pitch of 25 Ω at 20 μT with +20 V of bias. 105

8.1 Turbulent amplitudes in the grounded case 109

Chapter 1

Motivation and Introduction

For at least the past 60 years, physicists have had their sights set on plasma fusion as a potential alternative energy source for the future. From the earliest toroidal vessels pioneered in the United Kingdom to the much–improved Soviet tokamaks of the 1960's [1], the goal has been the same: produce thermonuclear fusion inside of a man–made device in a laboratory. With relatively abundant fuel, comparatively little radioactivity, and the promise of a smaller environmental footprint, fusion research has continued through the years. Since those early days the number of devices has multiplied and their heating capabilities have increased correspondingly, but fusion has remained an elusive goal.

While much of the initial tokamak work focused on improving conditions in the core of the device, more recent work has focused on the edge, the so–called "scrape off layer," or SOL. It is now known that the edge conditions are an important factor in determining confinement because this is where the hot dense core plasma escapes to the wall or divertor. Steep gradients in the edge lead to improved confinement but also trigger ELMs and other instabilities. Hence, a better understanding of the tokamak SOL is essential in order to make plasma fusion a viable energy source.

In order to better study some of the relevant SOL physics, other classes of devices have been employed, including the simple magnetic tori, or SMTs. The Texas Helimak is one of these devices and functions as, in many respects, a tokamak SOL without the rest of the tokamak. It has been described as a "wind tunnel" for tokamak physics. While it operates at much lower densities, temperatures, and magnetic fields than a tokamak (see Section 2.1.2), many interesting parallels can be drawn based on the similarities in dimensionless parameters between the Helimak and the tokamak SOL (see Section 2.1.3). Conversely, the Helimak's lower temperatures and pressures allow for the extensive use of Langmuir probes which would be destroyed in many tokamak applications. These allow for straightforward and accurate measurements of many key plasma parameters. In short, it is a useful testbed for tokamak physics at lower operating cost in terms of both materials and manpower.

However, the simplicity of the device does not imply that it is without its intricacies. In particular, several questions about which instabilities dominate in the

machine and how they behave under certain conditions are particularly interesting. Various journal articles and theses over the past decade have reached incongruous results about the machine's dominate instabilities. Buoyed by more recent theory and experiments, it is the purpose of this present work to firstly, describe the Helimak and its outstanding problems in more detail, secondly, describe the methods used to answer these questions, and finally, to shed some interpretative light on the results of these experiments.

Chapter 2 contains an explanation of the design and operation of the Helimak device, as well as a discussion of the theory of Langmuir probes, its primary diagnostic. That chapter finishes with a brief overview of the most applicable statistical methods used to describe the Helimak plasma. Chapter 3 explains the above–mentioned instabilities in more detail and discusses methods of differentiating between them. Chapter 4 provides profiles and discussion of basic plasma parameters, such as ion density, electron temperature, and floating potential. It includes a discussion of the effects of magnetic field pitch angle and applied bias voltage. It finished with descriptions of the typical turbulent amplitudes in the machine. Chapter 5 discusses certain experimental concerns in the taking of this data. Chapter 6 analyzes and comments on the results of the experiments with grounded bias plates. Chapter 7 follows naturally from its preceding chapter with a discussion of the effects of bias, both positive and negative, on the Helimak plasma. Finally, a summary and conclusion are given in Chapter 8.

Chapter 2

Experimental Background

This chapter outlines the experimental basis for the work presented in this dissertation by describing various aspects of Helimak operation, data–taking, and data analysis. Section 2.1 discusses the Helimak device and parameters, Section 2.2 discusses the theory and use of Langmuir probes, and Section 2.3 discusses the statistics used to analyze Helimak data.

2.1 The Texas Helimak

The Texas Helimak was used for all of the data taken in this dissertation. Hence, some background on its design and operation is useful in understanding the experiments which follow. This section begins with a detailed description of the device itself in Section 2.1.1. This is followed by an outline of the device's parameters in Section 2.1.2. Finally, a short comparison of the Helimak to the tokamak scrape–off layer, to which it is frequently compared, comprises Section 2.1.3.

2.1.1 The Helimak Device

The Texas Helimak is a large, toroidal plasma device located on the campus of the University of Texas at Austin. It functions as an experimental realization of the theoretical one–dimensional, sheared, cylindrical slab [2][3]. Its design was originally discussed in detail in a technical note from the University of California, San Diego [4]. This simple geometry affords simplified scenarios in which to study the behavior of plasmas with cylindrical curvature in an open magnetic field line configuration. Its straightforward correspondence with a well–known theoretical construction allows for comparison between experimental data and computational results. Indeed, several computational studies of Helimak plasmas have been published. See, for example, [5],[6],[7], and [3]. The Helimak, like other similar devices, is often referred to in the literature as a simple magnetic torus, or SMT.

The vessel is made of stainless steel and measures two meters tall with an inner radius of 0.6 m and an outer radius of 1.6 m, as shown in Figure 2.1. The three axes

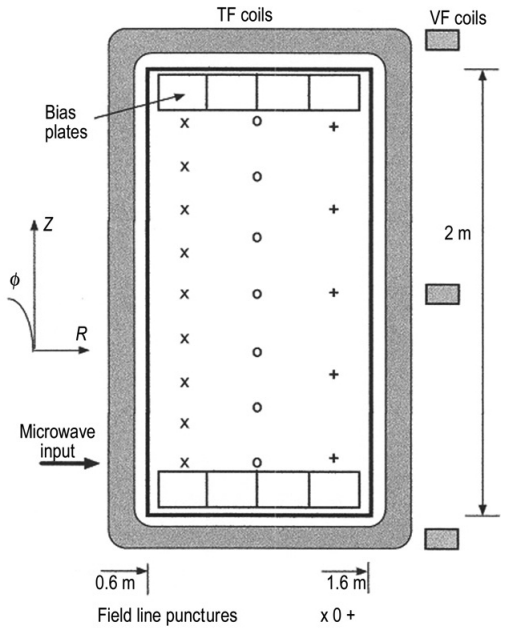

Figure 2.1: Cross Section of the Helimak showing dimensions, endplates, and magnetic field punctures

of the device are usually denoted r, z, and ϕ. The dominant magnetic field is in the ϕ direction, B_ϕ, with a much smaller vertical component, B_z. The finite B_z allows for a small plasma current to flow back through the walls of the vessel, creating a closed current loop that offsets the natural polarization drift's tendency to send the plasma electrons and ions in opposite vertical directions. This vessel current, therefore, stops the build–up of charge separation and allows for a stable MHD equilibrium. Indeed, as given in [4], the Grad-Shafranov equation has an analytical solution for this geometry, given by:

$$r^2 = -\frac{\mu_0^2}{4\pi^2}\frac{I_z I_z'}{\mu_0 p' + B_z}, \tag{2.1.1}$$

where p and I_z are the pressure and vertical current. In the derivation both have been rewritten as functions of B_z and primes represent differentiation with respect to B_z as well.

The magnetic field is produced by sixteen toroidal field coils and three vertical field coils, as shown in Figure 2.1. Current is supplied by an SCR power supply which can supply a constant current from 750 to 1200 A for more than 30 s. Functionally, changing the total current through the coils changes only the radial placement of the

density maximum without strongly affecting any other plasma quantities. Hence, the magnetic coil current is not typically explored as a parameter in Helimak experiments.

The power supply allows for a very fast repetition rate, limited only by the heating of the coils. At a typical current of 800 A the machine can be run three times in two minutes for several hours before the coils need to cool. More typical for turbulence work, the repetition rate is governed by the rate at which the computer can retrieve the data from the fast digitizers (see below), which tends towards 2.5 or 3 minutes per shot. At these speeds the coil temperature reaches equilibrium and the Helimak can be run continuously without overheating.

A variable resistor allows the ratio of B_z to B_ϕ to be varied, which in turn changes the pitch of the field lines. The pitch can be varied over a wide range of values, producing magnetic connection lengths from 10 m to several kilometers. The changing of a resistor to change the pitch of the field lines leads to an odd Helimak convention. While the peak toroidal magnetic field decreases, as expected, at large r, the vertical magnetic field remains approximately constant. Hence, the pitch of the field lines increases at larger radius. This gives rise to magnetic shear, calculated as [4]:

$$s(r) = r\frac{d}{dr}\ln q = r\frac{d}{dr}\ln\left(\frac{hR_0B_{\phi 0}}{2\pi r^2 B_{z0}}\right) \tag{2.1.2}$$

$$s(r) = -2 \tag{2.1.3}$$

Given this magnetic shear caused by the pitch gradient, the radially constant quantity associated with the pitch of each experiment is the value of the resistance. Hence, when the parameters of a data–taking run are recorded for Helimak data the pitch is written in ohms (Ω). This convention will be used throughout this work. For reference, a table of pitches at various radii, in terms of magnetic connection length and pitch angle, is found in Appendix A.

For most pitches, the field lines begin and end on sets of stainless steel endplates mounted vertically inside the vessel. Each of the sixteen plates measures 8 in (20.32 cm) on each side. The plates are arranged inside the machine as indicated in Figure 2.1, in four sets of four, two sets on the top and two on the bottom of the vessel, separated toroidally by 180°. The four plates in each set are arranged radially and are numbered one through four, starting with the inboard plate. The

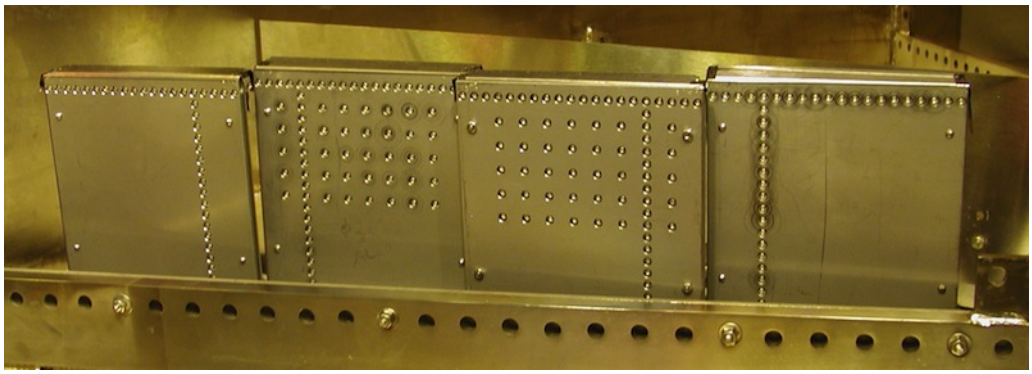

Figure 2.2: Photograph of the L plates. L1, the innermost plate, is on the right and the radius increases to the left of the photograph. The probes are visible as the small whitish circles

two sets of plates on the top are denoted "Top" (shortened to "T") and "Upper" ("U"), while those on the bottom are denoted "Bottom" ("B") and "Lower" ("L"). The top and upper plates are located vertically opposite the bottom and lower plates respectively. The plates will be referred to in this work by their letter designation and number. For example, the third plate from the inner wall on the bottom will be written "B3".

The endplates are grounded for normal operation. However, an interesting class of experiments has been conducted in which some of the plates are instead biased as first reported in [2]. For these experiments the four number two plates are biased across a range of values from $-50\,\mathrm{V}$ to $20\,\mathrm{V}$. However, for the experiments in this work the plate bias has been moved to plate 3 in each set for increased proximity to the movable probe drive, which is discussed below. For more information on the effects that this biasing has on the plasma profiles please see Section 4.1.

These plates also function as shielding for another set of plates onto which the Helimak's collection of Langmuir probes is mounted, as shown in Figure 2.2. The Helimak contains over 700 surface-mounted probes with circular geometry and a physical area of $1.6 \times 10^{-5}\,\mathrm{m}^2$. The probes all face in the $\pm\hat{\phi}$ direction and are predominantly arranged in a radial line with a separation of $1.0\,\mathrm{cm}$ between probes on the same plate and $1.5\,\mathrm{cm}$ spacing across the plate boundary. The total radial range covered by the probes runs from $R = 0.67\,\mathrm{m}$ to $R = 1.475\,\mathrm{m}$, for a total of $0.805\,\mathrm{m}$ of coverage across the $1.0\,\mathrm{m}$ width of the vacuum vessel. The main radial line of probes is located $20\,\mathrm{cm}$ vertically in from the top and bottom of the machine. This gives the Helimak an effective plasma height of $1.6\,\mathrm{m}$.

Additionally, each plate contains a vertical column of ten probes, with spacing of 1 cm, extending from the main radial line away from the midplane of the machine. Half of the plates also have grids in r and z with spacings of 2 cm, shown in Figure 2.2 on plates 2 and 3. Due to the toroidal symmetry and nature of the magnetic field it is usually assumed that r is the most experimentally relevant direction, at least to first order. Some work is also done on quantities that vary in z. Few, if any, differences in plasma quantities are typically detected in ϕ. It is for these reasons that the probes are arranged as they are. These probes are labeled beginning at the inner edge of the plate. The main radial line of probes on each plate is numbered 1 through 20. The vertical columns and grids, where present, are labeled with the number of the corresponding radial-line probe with an added letter, beginning with "A" and continuing (skipping "I") as the probes move away from the midplane of the machine. For a discussion of Langmuir probe theory see section 2.2.

Another set of Langmuir probes which will be important in this work is a set of four probes, or which three are currently functional, attached to a movable probe drive (MPD) that is mounted on the top of the machine. This probe drive moves in the vertical direction and can insert the probes on its tip up to 54.3 cm into the plasma, or just over one-fourth of the height of the machine. Toroidally, the MPD is separated by 112.5° from the probes on the upper plates. Radially, it is located at 1.293 m from the major axis, which puts it between probes U4-01 and U4-02, though two of the individual probes vary by about 1 cm from the radial position of the MPD.

Helimak discharges are run in a variety of gases. Argon and helium are the most common; of these two, argon is preferred because of its ease of use. Only a few warm–up shots are required before data can be taken for the day. Once equilibrated the argon pressure will remain constant throughout the course of the day. Before running in helium, on the other hand, several hours worth of conditioning shots must be taken to load the walls and produce a stable plasma for data taking. For this same reason, hydrogen is not typically used. No amount of conditioning has been experimentally shown to load the walls sufficiently to allow for a stable hydrogen plasma. However, other heavy noble gases have been used, including neon and xenon. This work will focus on data taken in argon. The gas is fed into the vessel via a set of capillary tubes and a needle valve. This allows for the feed pressure to be varied across experiments. It has been observed in the past that the feed pressure has no

visible effect on the plasma density but that increased feed pressure does increase the collisionality inside the device.

The plasma is created via RF heating of the neutral gas which makes use of a standard 2.45 GHz microwave source. While the power delivered is typically 6 kW, it can be varied over a small range. However, this parameter change is not very interesting in terms of plasma effects so it will not be explored here. The microwaves are deposited in the vessel by a simple open waveguide that opens at the inner radius of the vessel, localized in ϕ and z. The plasma discharge forms at the location of the ECH which is radially localized due to the $1/r$ dependence of the toroidal magnetic field. Most of the power is absorbed at the upper hybrid resonance. However, it has also been shown that single pass absorption of the microwaves is low. The Helimak vessel then acts as an over–moded chamber and the microwaves are absorbed after multiple passes. At present, the reasons for this are not fully known.

2.1.2 Helimak Parameters

The Helimak has an array of variables that can be directly controlled by the operator. These are shown in Table 2.1 along with the variable range and typical values used in this work. The effect on the plasma of each of these variables is described above, in Section 2.1.1.

Variable	Range	Typical Values
Gas feed pressure (μT)	$10 - 40$	10, 20, 30, 40
Magnetic field line pitch (Ω)	$0.0 - 50$	2.7, 3.3, 3.6, 5.0, 10, 15, 20, 25
Total magnetic coil current (A)	$750 - 1200$	800
Microwave power (kW)	$2.0 - 6.0$	6.0
Applied plate bias (V)	$-50 - 20$	$-40, -20, -10, -5, +10, +20$

Table 2.1: Controllable Helimak variables with typical values

In addition to the control variables, past studies on the Helimak have produced a set of reliable measurements of the device's basic plasma parameters [2][3]. Several of those considered most relevant are given in Table 2.2.

Parameter	Value	Parameter	Value
T_e (eV)	10	ν_{ee} (s^{-1})	1.31×10^5
T_i (eV)	0.1	ω_{ce} (s^{-1})	1.76×10^{10}
n (m^{-3})	$\leq 10^{17}$	ω_{ci} (s^{-1})	2.39×10^5
B_ϕ (T)	$0.05 - 0.13$	ω_{pe} (s^{-1})	1.78×10^{10}
$L_n = n/(dn/dr)$ (m)	0.2	ω_{pi} (s^{-1})	6.60×10^7
c_s (m/s)	4.9×10^5	v_{T_e} (m/s)	1.32×10^6
ρ_s (cm)	2.05	v_{T_i} (m/s)	268
β	4×10^{-5}	λ_D (m)	7.43×10^{-5}

Table 2.2: Measured Helimak plasma parameters

2.1.3 The Helimak and the Tokamak Scrape–off Layer

The Helimak and other SMTs are often referred to as testbeds for the tokamak scrape–off layer (see, for instance, [2], [7], [8]). Briefly, the scrape–off layer (SOL) is the region in a tokamak outside of the magnetic separatrix. Inside of the separatrix is the core, defined by closed magnetic field lines, high densities, and high temperatures. The SOL, on the other hand, is characterized by open magnetic field lines, lower temperatures, and lower densities. While the open magnetic field lines are akin to those of the Helimak, the SOL ion density in DIII–D, a large tokamak at General Atomics in San Diego, is approximately 10^{18} while the electron and ion temperatures can be up to 200 eV and 100 eV respectively and a magnetic field of up to 2 T can be used [9].

Comparison of these values with those in Table 2.2 shows that the Helimak is not a SOL surrogate in the typical sense. The relationship between the Helimak and SOL become clear when examining the unitless parameters of both devices, as given in Table 2.3.

	Helimak	DIII–D SOL
Transverse size (ρ_s/L_n)	0.2	0.05
Parallel size L_c (m)	50	40
β	4×10^{-5}	3×10^{-4}
Drift drive (v_D/c_s)	0.2	0.06
Collisionality (L_c/λ_{ee})	0.1	0.02
Turbulence Level ($\Delta n/n$)	0.4	0.3

Table 2.3: Comparison of Helimak and DIII–D SOL parameters

While also similar in physical size, the Helimak shares several desirable parameters with the DIII–D SOL. Many of the parameters in the table vary by a factor of only four or five. Hence, while much lower in temperature and density, the Helimak shares enough similarities with the SOL that it can be considered a useful testing ground for SOL concepts.

2.2 Langmuir Probes

Without question, Langmuir probes are among the most practical and most widely–used instruments for obtaining plasma data. Their simplicity of design, ease of use, and straightforward ability to yield important plasma quantities make them invaluable in plasma physics research. The Helimak makes great use of Langmuir probes, as previously mentioned, with over 700 such probes in the device. This section describes the basics of their theory, in Sections 2.2.1 through 2.2.3 and use, in Section 2.2.4.

2.2.1 Plasma Sheath

Langmuir probe theory is based on the physics of plasma sheaths [10][11]. A sheath develops at the surface of any material placed into a plasma, though in this case the primary concern is a conducting material placed in the plasma. The physical size of this sheath will be on the order of a Debye length, λ_D. The conducting surface will tend to "float" at a voltage which will draw zero current from the surrounding plasma. This "floating potential" is typically denoted ϕ_f or V_f. This potential will nearly always be different, and in the case of the Helimak, is always different from the potential of the bulk plasma, or "plasma potential," typically denoted ϕ_p or V_p. This difference is primarily due to the fact that, due to their lower mass, electrons will typically have much higher thermal speeds than their ion counterparts. This means that when a conductor is placed in the plasma it will initially acquire a negative charge. This will create a negative electric field which acts both to repel further electrons and to pull ions into the vicinity. Though the ions will eventually reach the conductor to balance out the electrons, the floating potential will remain lower than the plasma potential. The plasma potential is nearly always positive for a very similar reason. Namely, the more mobile electrons are more likely to escape

the plasma altogether, leaving the plasma slightly positive. As the electron thermal energy increases and more electrons escape, the plasma potential increases as well.

2.2.2 Sheath Densities

For Langmuir probes, on the other hand, a metallic probe, biased compared to ground, is inserted into the plasma instead of a floating conductor. For ion saturation data the probe is biased negatively enough so as to discourage electrons from reaching the probe, whereas for equilibrium characteristic data the probe bias is swept from positive to negative. This allows both the ion saturation region and the curve of the transition region from ion to electron saturation to be sampled. In practice, the amplifiers saturate long before reaching electron saturation.

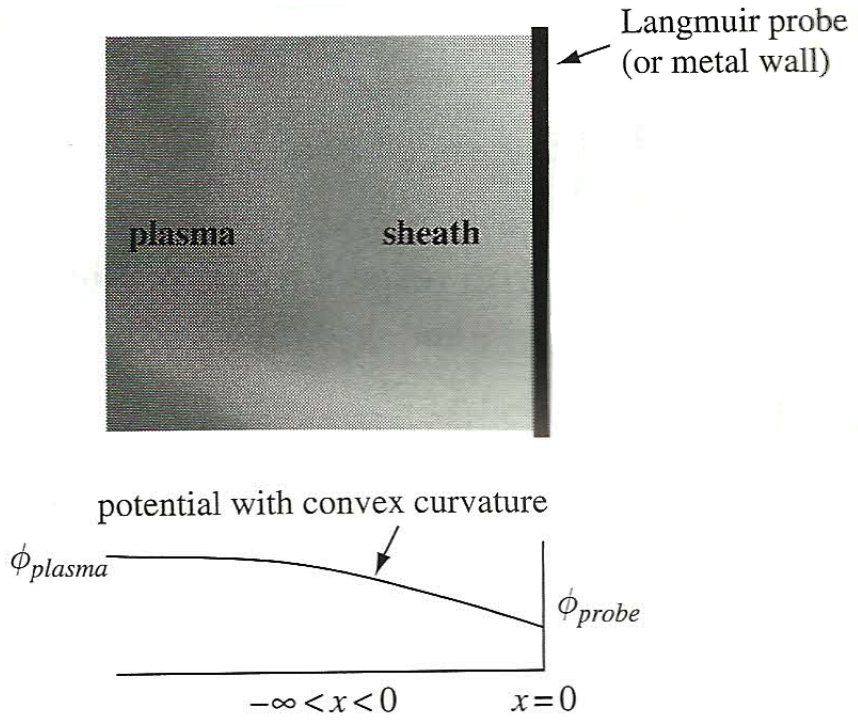

Figure 2.3: Theoretical semi-infinite plasma set-up for derivation of Langmuir probe characteristics

To analyze the behavior of Langmuir probes it is first useful to imagine a simplified scenario in which there exists a one–dimensional plasma with a conducting wall as depicted in Figure 2.3 (image from [10]). For simplicity sake, one assumes

that the probe is located at $x = 0$ and that the plasma is semi–infinite, i.e. it fills all of space from $-\infty < x < 0$. In reality, this is a reasonable first approximation for a large, magnetized plasma such as that found in the Helimak. In such a case the primary motion of the plasma will be along the field lines, justifying the one-dimensional assumption. Likewise, the large size means that the plasma edge is many Debye lengths away from the probes, allowing end effects to be ignored and thus justifying the semi–infinite assumption. It is further assumed that the electron distribution function is Maxwellian. This assumption is less agreeable in the Helimak where high–energy electrons form a significant tail to the distribution.

The analysis begins by biasing the probe negative with respect to the plasma. With the above assumptions, the electron density in the neighborhood of the probe can be described. If over the range of all negative x values, the difference of the measured potential from the plasmas potential is defined by $\Delta\phi(x) = \phi(x) - \phi_p$ then this density can be calculated by [10]:

$$n_e(x) = \int_{-\infty}^{\infty} \mathrm{d}v f_{e,Maxwellian}(v, 0) = n_0 \exp\left(e\Delta\phi(x)/kT_e\right). \tag{2.2.1}$$

It is possible to simply Eq. (2.2.1) by looking closely at the character of $\Delta\phi(x)$ in several limits. Far from the probe, by definition, $\phi(x) = \phi_p$. Hence, in that region $\Delta\phi(x) = 0$. At the probe, on the other hand, $\phi(x) = \phi_B$, where ϕ_B is the biased potential of the probe. In this region, $\Delta\phi(x) = \phi_B - \phi_p$. Plugging this into equation (2.2.1) for regions near the probe yields:

$$n_e = n_0 \exp\left(e(\phi_B - \phi_p)/kT_e\right). \tag{2.2.2}$$

This returns the intuitive result that if the probe is biased below the plasma potential only a small portion of the electrons, namely, those with enough thermal energy to overcome the potential barrier, will reach the probe. Given that, for this derivation, the probe is biased to a negative voltage it follows that $\phi_b < \phi_p$. Hence, $\Delta\phi < 0$ and in the neighborhood of the probe there is a diminished electron density compared to that of the bulk plasma.

The ions behave much differently than the electrons. Once the initial negative sheath is in place all of the ions will be attracted to it; there is no potential barrier that must be overcome. As they approach the potential well surrounding the probe

they will accelerate. Under the assumption that the total flux must be conserved then:

$$n_0 u_0 = n_i(x) u_i(x) \tag{2.2.3}$$

Where subscript naught indicates the bulk plasma and subscript i indicates the sheath. Since the ions will accelerate as they encounter the potential drop of the sheath it is necessary that $u_i > u_0$ and hence $n_i < n_0$. Thus, the ion density also decreases in the sheath, though for a much different reason than the electron density.

2.2.3 Sheath Currents

With the densities in hand one can now produce expressions for the currents that will be collected at the probe, given by the usual expressions: $I = JA = nquA$, where J is the current density, A is the area of the probe, q is the charge of the species, and u is the velocity at which the plasma particles hit the probe. It should be noted that there are various theories involving different shapes of Langmuir probes. Inside of the Helimak each probe is essentially a circular piece of a plane. Hence, the simple planar probe theory serves quite well. It should be noted that A is an effective collection area. Given that the pitch of the Helimak magnetic field lines is never too great it can safely be assumed that the field lines are normal to the surface of the probes. Hence, the effective area is equal to the physical area.

Since flux conservation has been invoked for the ions, $n_i u_i$, or the flux of ions hitting the probe, can be replaced with $n_0 u_0$, or the flux before hitting the sheath. Conservation of energy is now invoked in order to find an expression for u_0:

$$\frac{1}{2} m_i u_0^2 = \frac{1}{2} m_i u_i^2(x) + e\Delta\phi(x), \tag{2.2.4}$$

which is easily solved to produce

$$u(x) = \sqrt{u_0^2 - 2e\Delta\phi(x)/m_i}. \tag{2.2.5}$$

Upon plugging into Eq. (2.2.3) it is immediately seen that

$$n_i(x) = \frac{n_0}{\sqrt{1 - 2e\Delta\phi(x)/m u_0^2}}. \tag{2.2.6}$$

It is now desirable to relate this expression to the electron density in the region, given by Eq. (2.2.1). Quasi-neutrality demands that $n_i \approx n_e$. In this case, more clarity is found by noting that $\Delta\phi(x)$ is a decreasing function. In addition to the explanation given above about the relative magnitudes of $\phi(x)$ and ϕ_p, it is also reliably observed experimentally that the slope of $\Delta\phi(x)$ is decreasing. Hence, the second derivative of $\Delta\phi(x)$ is concave down and negative as well [12]. By application to Poisson's equation:

$$\frac{\mathrm{d}^2\Delta\phi}{\mathrm{d}x^2} = -\frac{e}{\epsilon_0}\left(n_i(x) - n_e(x)\right) \tag{2.2.7}$$

it can be seen that the only possible way for the second derivative to be negative is if $n_i(x) > n_e(x)$.

To simply Eq. (2.2.5), Eqs. (2.2.6) and (2.2.2) are now plugged into the negativity condition derived from Eq. (2.2.7):

$$\left(1 - \frac{2e\Delta\phi(x)}{m_i u_0^2}\right)^{-\frac{1}{2}} > \exp\left(\frac{e\Delta\phi(x)}{kT_e}\right). \tag{2.2.8}$$

Inverting and squaring both sides and remembering that $\Delta\phi(x)$ is negative yields

$$1 + \frac{2e|\Delta\phi(x)|}{m_i u_0^2} < \exp\left(\frac{2e|\Delta\phi(x)|}{kT_e}\right). \tag{2.2.9}$$

Expansion of the exponential in a Taylor series shows:

$$\frac{2e|\Delta\phi(x)|}{m_i u_0^2} < \frac{2e|\Delta\phi(x)|}{kT_e} + \frac{1}{2}\left(\frac{2e|\Delta\phi(x)|}{kT_e}\right)^2 + \cdots . \tag{2.2.10}$$

The only way that this can be satisfied for all $|\Delta\phi(x)|$ is if

$$u_0^2 > \frac{kT_e}{m_i}. \tag{2.2.11}$$

Hence, the ions enter the probe region with a velocity larger than the ion acoustic velocity, usually denoted c_s, and also known as the Bohm speed. Their velocity will only be slightly larger, however, due to the constraint of quasi–neutrality which, though it may not hold completely in this case, still holds the electron and ion densities close, though not equal.

The total expression for the ion current striking the probe is now given by:

$$I_i = n_0 u_0 eA = n_0 c_s eA = n_0 \sqrt{\frac{kT_e}{m_i}} eA. \tag{2.2.12}$$

The usual expression given is known as the the Bohm ion current and differs from the derived expression by a factor of 0.6. This difference arises due to the reduction of ion density in the presheath, a region not considered here in which the ions are accelerated to the ion acoustic velocity [11]. Bohm argued that the presheath leads to a potential drop of $0.5T_e$ over a long distance inside the plasma. This gives the ions a velocity at the sheath edge, even when the bulk $T_i = 0$ [12]. Putting this together yields the final expression for I_i:

$$I_i = I_{Bohm} = 0.6 n_0 c_s eA. \tag{2.2.13}$$

The electron current impinging on the probe is given similarly, using the electron thermal velocity for u_e:

$$I_e = n_e q u_e A \tag{2.2.14}$$

$$= -n_0 eA \sqrt{\frac{kT_e}{2\pi m_e}} \exp\left(-\frac{e(\phi_p - \phi_b)}{kT_e}\right) \tag{2.2.15}$$

The total current to the probe is then given by the combination of these two currents:

$$I = 0.6 n_0 c_s eA - n_0 eA \sqrt{\frac{kT_e}{2\pi m_e}} \exp\left(-\frac{e(\phi_p - \phi_b)}{kT_e}\right) \tag{2.2.16}$$

2.2.4 Probe Use

Based on the results of the previous section, a real set of Langmuir probe data can be used to calculate the ion density (n_0), electron temperature (T_e), and floating potential (V_f) of the plasma. This is accomplished by sweeping ϕ_b across a wide range of values. Figure 2.4 gives a sample of the probe curve that results. At large negative values the ion saturation current is nearly constant. As ϕ_b increases the total current passes through zero at the floating potential, then increases exponentially towards the unreached electron saturation region.

The plasma characteristics are deduced from such a plot by working backward

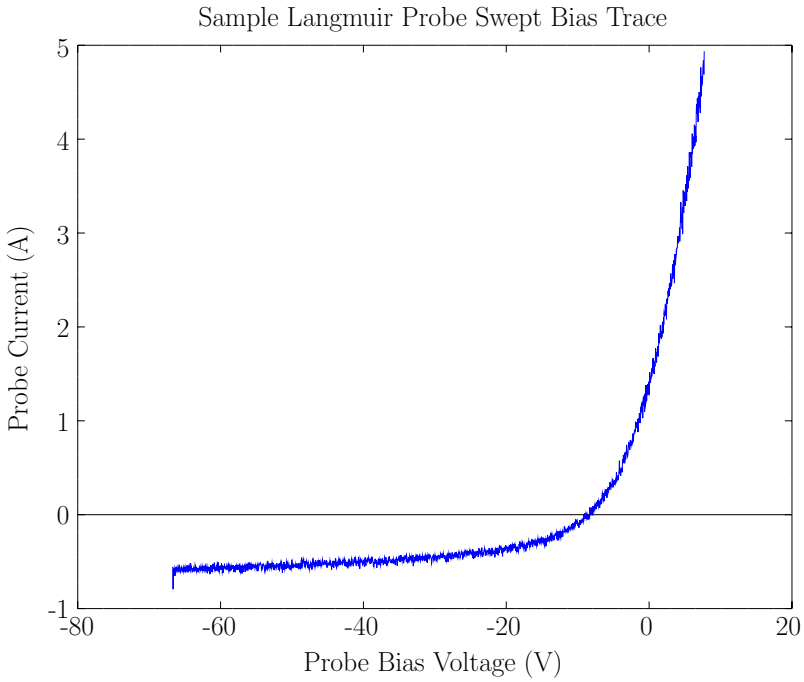

Figure 2.4: Sample Langmuir Probe Trace when Swept Voltage is Applied

from Eq. (2.2.16). The constant I_i is first subtracted from all of the data, leaving I_e. A plot of $\ln(I_e)$ versus ϕ_b is then produced. The slope of the resulting fit line gives $1/kT_e$. Once T_e is known c_s can be calculated. With this value in hand, n_0 is calculated by simple division from the value of the ion saturation current, given by Eq. (2.2.13), with knowledge of the probe area. The floating potential is found by observing at what voltage the current crosses zero. This is the point at which zero current flows to the probe, which is the definition of the floating potential.

A theoretical examination of the floating potential yields a relationship between ϕ_p and ϕ_f, where ϕ_f is used to denote the floating potential, $\phi_b|_{I=0}$. When $I = 0$ it is seen that

$$I_i = -I_e \tag{2.2.17}$$

$$0.6\sqrt{\frac{kT_e}{m_i}} = \sqrt{\frac{kT_e}{2\pi m_e}} \exp\left(-\frac{e(\phi_p - \phi_f)}{kT_e}\right) \tag{2.2.18}$$

$$\ln\left(0.6\sqrt{\frac{2\pi m_e}{m_i}}\right) = -\frac{e(\phi_p - \phi_f)}{kT_e} \tag{2.2.19}$$

$$\phi_p - \phi_f = -\frac{kT_e}{e} \ln\left(0.6\sqrt{\frac{2\pi m_e}{m_i}}\right). \tag{2.2.20}$$

Some rearranging yields

$$\phi_f = \phi_p - \frac{kT_e}{e} \ln\left(\frac{5}{3}\sqrt{\frac{m_i}{2\pi m_e}}\right). \tag{2.2.21}$$

Hence, ϕ_f will be less than ϕ_p by a numerical factor that depends both on T_e and on the ion–electron mass ratio. For argon, the mass ratio piece comes out to be approximately 4.7. With warm electrons with $kT_e/e \approx 10\,\text{eV}$, it is expected that the floating potential in a Helimak argon plasma is approximately 47 eV lower than the plasma potential. While this equation is commonly used to obtain ϕ_p it is extremely inaccurate when used to determine fluctuating quantities, such as $\tilde{\phi}_p$. Hence, it cannot be used on the Helimak to accurately find the fluctuating quantities needed to calculate the transport coefficients.

2.3 Statistical and Computational Methods

Data taken by the Helimak's suite of Langmuir probes (see Section 2.1.1) passes from the machine to a large patch panel. The number of probes far outnumbers the number of available digitizers. Hence, only selected channels can be processed for each shot. Those selected channels are sent through a set of unity–gain amplifiers and digitized. For ion saturation data these amplifiers are biased to ion saturation, typically around $-70\,\text{V}$, but for potential measurements they are allowed to float. The amplifiers can also be swept in order to take equilibrium plasma profiles (see Chapter 4.1 for a discussion of the equilibrium plasma). For turbulence data a 96–channel digitizer that collects ten seconds of data at 500 kHz is used. For equilibrium data there is a set of 64 slower digitizers that collect 20 seconds of data at 7 kHz.

All data taken on the Helimak is digitized and stored locally using MDSplus. Once there, the time traces can be viewed on the DWScope program and visually inspected for errors in the shot. Samples of the traces are shown in Figure 2.5. The top figure shows a subsample of the complete set of data at the normal zoom level (i.e. the data as it appears on the scope) while the bottom trace is zoomed in to show what the data looks like on a shorter time scale.

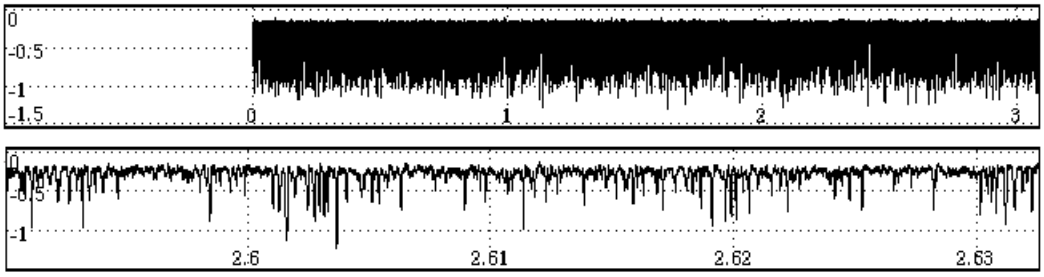

Figure 2.5: Sample MDSplus traces as shown by DWScope

However, little quantitative data can be deduced from the traces themselves. In order to obtain useful results from the data taken a statistical analysis program is used. This program, called StatAnalX, written by Professor Kenneth Gentle in C++, calculates various statistics for the data. It calculates both one and two channel statistics. Following a brief discussion of sampling (Section 2.3.1), this section gives an overview of the various statistical methods that are used in this work, including fast Fourier transform (FFT), auto– and cross–correlation, power spectra, cross–spectra, and bicoherence.

2.3.1 Sampling

Helimak data can be considered stochastic data. The long time series are subject to statistical analysis but individual points cannot be predicted with any accuracy. Indeed, while the statistical values are repeatable between shots, the traces themselves are vastly different. However, the data can also be considered stationary in the sense that the average plasma quantities, once the microwave power and magnetic coils are up to full power, do not change over the course of the shot. The data taken can then be considered as a discrete set of random variables which must be considered in terms of their probability distribution function, averages, and frequency spectra.

As mentioned in the above introduction to the section, for turbulence data the plasma is sampled at 500 kHz by the fast digitizer. Based on the Nyquist–Shannon sampling theorem, the highest frequency in the plasma that can theoretically be completely resolved is half of the sampling frequency, or 250 kHz. Other considerations, such as the amplifiers in use, may decrease this bound even further [13]. Practically speaking, for the data taken in this work there are rarely any interesting plasma fea-

tures above approximately 10 kHz, meaning that all of the data falls safely within the limit.

2.3.2 Fast Fourier Transform

The fast Fourier transform (FFT) is a one–channel statistic that is both the most basic and one of the most powerful statistical tools available. Its simplicity lies in the straightforward way in which it may be derived from the continuous Fourier transform. Its power lies in combining it with other statistical measures. Indeed, it forms the backbone of almost every other statistical method that will be presented in this section.

Functionally, the FFT allows for the conversion our digitized time–domain signals to traces in the frequency domain. This allows for the determination of which frequencies of oscillating signals are present in the data, as well as for comparisons of their relative strength in the signal. This is clearly useful in turbulence and instability data as it provides a possible correlation with theoretical predictions of turbulent frequencies. A determination can be made of which frequencies are the strongest and, combined with other statistics, it can be seen how that changes over the chosen parameter space.

Mathematically, the FFT is the discrete version of the continuous, or analog, Fourier transform well–known to undergraduate students. The "fast" part of its name refers simply to the optimization of the algorithm for computational speed and efficiency. The continuous Fourier transform is given in many texts and, for a time series $f(t)$, may be written:

$$F(\omega) = \frac{1}{\sqrt{2\pi}} \int_{-\infty}^{\infty} f(t) e^{-i\omega t} dt. \tag{2.3.1}$$

Here, through an integral over all time the frequency spectrum of the data is obtained. The reverse operation can also be performed to reproduce the time series from the Fourier transform:

$$f(t) = \frac{1}{\sqrt{2\pi}} \int_{-\infty}^{\infty} F(\omega) e^{i\omega t} d\omega. \tag{2.3.2}$$

The discrete Fourier transform follows directly from the above, making minor adjustments for the nature of the data. Most notably, The integral over time is replaced with a summation, a more natural operation for digitized data. Since, in

practice, there are no infinite time windows in which to work, the time scale is also adjusted to fit the number of data points in the sample or its subsample, given by N. Also, traditionally, n is used in place of t and k is used in place of ω to indicate the frequency variable. This should not, however, be confused with the use of k as a wavenumber, which will be discussed in Chapter 3. Making these adjustments yields [13]:

$$F[k] = \frac{1}{N} \sum_{n=0}^{N-1} x[n] e^{-i2\pi kn/N}. \tag{2.3.3}$$

The application of this equation to a time series of Helimak data essentially produces a histogram of frequencies, or a frequency spectrum, showing which frequency components appear most commonly in the data. Those with a strongly presence will have a correspondingly higher amplitude. As a note, while in this work spectra of this sort will be presented as solid curves for ease of readability, it is useful to remember that they actually represent discretized functions.

It should also be noted that the FFT is only computationally fast for 2^N samples. In general, N should be chosen to be no larger than necessary in order to resolve the lowest frequencies. For large data sets, such as those from the Helimak, the FFTs reported are the average over many smaller intervals.

2.3.3 Power Spectrum

The power spectrum is closely related to the Fourier transform. While the Fourier spectrum is inherently complex, the power spectrum represents the real part, obtained by:

$$P_{xx}(k) = |F[k]|^2 \tag{2.3.4}$$

This represents the "power" that each of the Fourier components adds to the total fluctuation power and can be used to determine the relative strengths of the frequencies present. The power spectrum will be used extensively in this work as a means of examining the relative amplitudes of fluctuations in the plasma to determine which frequencies dominate in particular regimes.

2.3.4 Autocorrelation

The autocorrelation function is a one–channel statistic that is useful for looking for recurring patterns in a time series of data. It is defined by:

$$R_{xx}(\tau) \equiv \int_{-\infty}^{\infty} x(t)x^*(t-\tau)dt. \tag{2.3.5}$$

where $x(t)$ is a continuous random variable.

Qualitatively, the operation involves a sliding comparison of a signal against itself. For each instance a time delay, τ, is introduced and the integral of Eq. (2.3.5) taken. Once completed for all desired time delays the resulting function gives an indication of the original signal's relationship to itself at different times. At $\tau = 0$ the signals are matched up and equal, yielding a maximum value of $R_{xx}(0) = 1$ for the autocorrelation. At other times, the signals will drop towards zero with a time to drop to $1/e$ known as the decorrelation time. The autocorrelation of nonperiodic signals will drop steeply to zero and stay nearby, while that of periodic signals may drop less steeply and may show a pseudo–sinusoidal quality indicative that the signal may be approximately self–similar at multiple time-s. This is a good indication that the signal displays some form of oscillatory behavior.

2.3.5 Cross–Correlation

The cross–correlation function is closely related to the autocorrelation function. This time, however, two separate signals from two separate Langmuir probes are taken and the same sliding comparison performed as before. This gives a general idea of the strength of the relationship between two separate probe signals. The cross-correlation is defined by:

$$R_{xy}(\tau) \equiv \int_{-\infty}^{\infty} x(t)y^*(t-\tau)dt. \tag{2.3.6}$$

where $x(t)$ and $y(t)$ are again continuous random variables.

As with the autocorrelation, the cross–correlation of most probe signals will drop quickly to zero. Unlike the autocorrelation, however, the cross–correlation does not necessarily have a maximum of one at $\tau = 0$, rather its maximum value will be

between zero and one and may occur for a value of $\tau \neq 0$. The greater the value, the higher the correlation between the two signals, while a time lag indicates the time that it takes for the signal to travel between the two probes. Generally, only this maximum value is used for comparing signals in this work because, regardless of the time at which it occurs, it represents the best case relationship.

This statistic is extremely helpful and great use of it was made in aligning the probes correctly. For more information, see Section 5.2.

2.3.6 Cross–Spectrum and Significant Cross–Phase

Just as the cross–correlation can be computed to show the strength of the relationship between time signals from different probes, the cross–spectrum can be computed in order to see how their frequency spectra compare. The cross–spectrum can be defined either as the Fourier transform of the cross–covariance (a sort of unnormalized cross–correlation) or as the product of their Fourier spectra. For two signals, $x(t)$ and $y(t)$ with Fourier transforms $X(\omega)$ and $Y(\omega)$ the cross–spectrum can be computed as:

$$P_{xy}(\omega) \equiv X^*(\omega)Y(\omega). \tag{2.3.7}$$

This quantity is inherently complex and can be decomposed into real and imaginary parts [13]:

$$P_{xy}(\omega) = C_{xy}(\omega) + iQ_{xy}(\omega). \tag{2.3.8}$$

Here, C_{xy} is called the co–spectrum and Q_{xy} the quadrature spectrum. The co–spectrum represents the covariance between the in–phase components and the quadrature spectrum the covariance between the out–of–phase components. Like all complex quantities the cross–spectrum can be written in polar form [13]:

$$P_{xy}(\omega) = |P_{xy}(\omega)|\, e^{i\alpha_{xy}(\omega)}, \tag{2.3.9}$$

where $|P_{xy}(\omega)|$ is the amplitude and $\alpha_{xy}(\omega)$ is the cross–phase. These are given by:

$$|P_{xy}(\omega)| = \sqrt{C_{xy}^2(\omega) + Q_{xy}^2(\omega)}, \tag{2.3.10}$$

$$\alpha_{xy}(\omega) = \arctan\left(\frac{Q_{xy}(\omega)}{C_{xy}(\omega)}\right). \tag{2.3.11}$$

The amplitude can be normalized to give the coherency spectrum, a measure of the strength of the correlation between frequency peaks across the two channels [13]:

$$\gamma_{xy}(\omega) = \frac{|P_{xy}(\omega)|}{\sqrt{|P_{xx}(\omega)|\,|P_{yy}(\omega)|}}, \tag{2.3.12}$$

where P_{xx} and P_{yy} are the respective power spectra of each signal.

The cross–phase, $\alpha_{xy}(\omega)$, represents the phase difference, or the lead or lag, between the frequency components of each signal. Importantly for this work, the cross–phase can be used to calculate the components of the wavevector, $\mathbf{k}$:

$$k_n(\omega) = \frac{\alpha_{xy}(\omega)}{\Delta n}, \tag{2.3.13}$$

where n is the desired component (r, z, or ϕ in the Helimak) and Δn is the distance in the direction of n between the two probes used to make the measurement. Hence, the cross–spectrum function can be used to produce effective dispersion relations for pairs of probes. The StatAnalX program actually produces statistics in terms of f, not ω, so it produces dispersion relations between α_{xy} and f which can easily be converted into relations between k and ω. Several examples of these dispersion relations are presented in Figures 6.6 and 6.7.

However, some frequency components carry more power than others and occasionally the cross–spectrum will produce large values of the coherency spectrum for components with little importance. To protect against this, the StatAnalX program also produces a statistic called the *significant cross–phase*. This statistic performs checks of the FFT magnitude at each spectral component and only includes those components in the cross–phase that have an FFT magnitude greater than a preset cutoff value, thus producing a cross–phase composed only of terms that "matter" to the power spectrum. Taking into account that not all spectral components are equally weighted allows for the computation of an accurate average of Eq. (2.3.13) (this equation has been left in terms of f to reflect the actual calculations used):

$$\langle k_n \rangle = \frac{1}{\Delta n} \frac{\sum_f \gamma_{xy}(f)\alpha_{xy}(f)}{\sum_f \gamma_{xy}(f)}. \tag{2.3.14}$$

All of the wavenumbers presented in this work were calculated using Eq. (2.3.14).

In accordance with the interpretation of the cross–phase as the dispersion

relation, the average phase velocity can be calculated from the slope of its best–fit line:

$$v_\phi = \frac{\omega}{k} = \frac{2\pi f}{\alpha_{xy}/\Delta n} = \frac{2\pi \Delta n f}{\alpha_{xy}} = \frac{2\pi \Delta n}{s}, \tag{2.3.15}$$

where s is the slope.

2.3.7 Bispectrum and Bicoherence

The bispectrum and closely related bicoherence are higher–order statistical functions that enable the identification of nonlinear interactions between frequency components [14]. These statistics are not based on the *moments* of the distributions but rather on their *cumulants*, which are defined by $K(t) = \log M(t)$, where $M(t)$ is the given moment for which the cumulant is desired. As explained by Kim and Powers in [14], cumulants of greater than or equal to third order must equal zero. Furthermore, all cumulants go to zero when the random variables that constitute them are statistically independent from each other. By extending to spectra, they showed that a given cumulant spectrum will be zero unless there are statistically related waves present whose frequencies add to zero ($\omega_1 + \omega_2 + \cdots + \omega_n = 0$). Hence, cumulants can be used to identify whether given frequencies are statistically related to one another or, in other words, whether there is joint dependence between waves of different frequencies.

From the previous discussion, the bispectrum may be defined as the third–order cumulant spectrum. It is given by [14]:

$$B(k,l) = E[X_k X_l X^*_{k+l}], \tag{2.3.16}$$

Where the X's represent Fourier transformed data and $E[\cdots]$ indicates the expected value. From this definition it is clear that the bispectrum shows a relationship between the three waves with frequencies k, l, and $k+l$. In the usual interpretation it is used to deduce three–wave coupling from a quadratic nonlinearity.

The bicoherence, usually written $b(k,l)$, is a normalized version of the bispectrum which affords a simple explanation of three–wave interactions. As a normalized quantity it runs from 0 to 1. A bicoherence value of 0 indicates no dependence between the waves while a value of 1 indicates a complete interaction. Intermediate

values represent intermediate degrees of coupling between the waves. This technique was used in this work to explore potential relationships between spectral components and is utilized in Chapters 6 and 7.

As a statistical tool, the bispectrum calculation has its roots in simple non-linear oscillators with well–defined frequency peaks. In a turbulent system, such as the Helimak, the bispectrum will be noisy. In order to clean up the data the analysis program averages over multiples iterations of the FFT interval, just as for the FFT calculation itself.

Chapter 3

Helimak Instabilities

This chapter defines and briefly outlines the major instabilities believed to dominate in the Helimak plasma. As this is an experimental dissertation there are no detailed derivations of the instabilities, but rather a presentation of the major results. Citations are given so that the full derivations may be found in the literature. Section 3.1 discusses the interchange instability, Section 3.2 discusses drift waves, and Section 3.3 outlines several methods found in the literature for differentiating between the two. Finally, Section 3.4 briefly explains why other modes are not considered.

3.1 Ideal Interchange Instability

The interchange instability is a nearly universal plasma instability that requires only a density gradient and force to form and destabilize. It is sometimes referred to as the flute instability due to its fluted column–like appearance in a cylindrical plasma, as depicted in Figure 3.1 (figure from [15]).

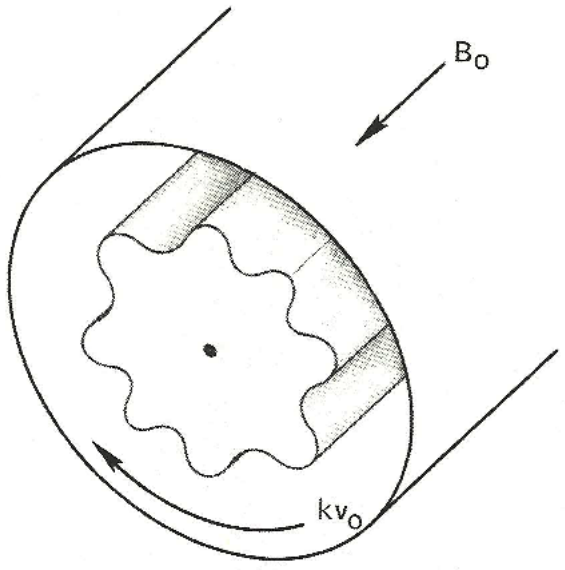

Figure 3.1: Illustration of the interchange, or flute, instability in a cylindrical plasma

Mathematically, the interchange mode is similar to the Rayleigh–Taylor instability of fluid mechanics. This instability arises when a heavy fluid is supported by a light fluid against the force of gravity. In the simplest case, the fluids meet at a plane, as depicted on the left side of Figure 3.2. In the absence of any triggers this situation sits on an unstable equilibrium, like a ball perched on top of a hill. At the slightest perturbation a transverse wave will develop along the boundary layer. This wave will propagate along the boundary, perpendicular to the direction of the density gradient. Energetically, it is favorable for the positions of the fluids to change places so they will do so, taking advantage of the potential energy available due to gravity. Eventually, the two fluids will have completely changed positions and settled into a minimum energy state, as shown in the far right of Figure 3.2.

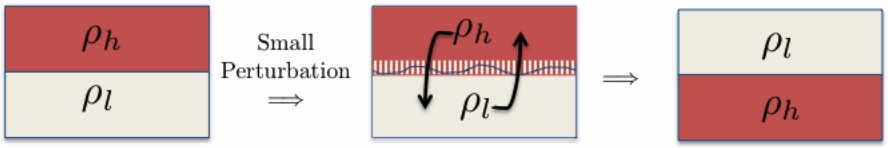

Figure 3.2: Simplified illustration of the Rayleigh–Taylor Instability

In a plasma, where the effects of gravity are minimal, the magnetic curvature takes the place of gravity and provides the force. The higher density regions of the plasma take the place of the heavy fluid while the lower density regions take the place of the light fluid. In order to be driven unstable the density gradient and radius of magnetic curvature must point in the same direction. On the high–field side of the device, the region of "good" curvature, the density gradient points radially outward, opposite of the radius of curvature. Hence, on this side of the density maximum the interchange instability is stable. On the low–field side, in the region of "bad" curvature, the collinearity of the pressure gradient and the magnetic field drives the mode unstable.

An expression for the growth rate of the interchange instability itself is derived from the ideal MHD equations, which includes the Maxwell equations together with

the force–balance equation and continuity equation:

$$\rho\left[\frac{\partial \mathbf{U}}{\partial t} + \mathbf{U}\cdot\nabla\mathbf{U}\right] = \mathbf{J}\times\mathbf{B} - \nabla P, \tag{3.1.1}$$

$$\frac{\partial \rho}{\partial t} = -\nabla\cdot(\rho\mathbf{U})\,. \tag{3.1.2}$$

While the derivation will not be provided here, the interested reader is encouraged to consult reference [6]. The result of the derivation is the following dispersion relation:

$$-\bar{\omega}^2 = \frac{2c_s^2}{RL_p}\left(1 - \frac{10}{3}\frac{L_p}{R}\right) \tag{3.1.3}$$

where c_s is the sound speed, R is the radius of magnetic curvature, and L_p is the pressure gradient scale length, given by $L_p \equiv {}^{-p_0}\!/_{p_0'} = {}^{L_n}\!/_{(1+\eta)}$. For sufficiently steep gradients this expression reduces to the commonly–seen interchange growth rate:

$$\gamma_I = c_s\sqrt{\frac{2}{RL_p} - \frac{20}{3R^2}}, \tag{3.1.4}$$

$$\gamma_I \approx \frac{\sqrt{2}c_s}{\sqrt{RL_p}} \approx \frac{c_s}{\sqrt{RL_p}}. \tag{3.1.5}$$

It is immediately apparent that the growth rate increases with c_s, which in turn increases with T_e. It also increases with increasing pressure gradient and decreases at large radius of magnetic curvature.

Perhaps the most striking characteristic of the interchange instability is its global character. The ideal interchange mode, ideal in the sense that the plasma has zero resistivity, has a wavevector exactly perpendicular to the magnetic field, $\mathbf{k}\cdot\mathbf{B}_0 = 0$. It thus has a wavenumber parallel to the magnetic field identically equal to zero, $k_\parallel = 0$. This implies an infinite wavelength in that direction and zero frequency. It must be noted that the zero frequency only applies to the plasma frame of reference which, when bulk plasma flows are present, is different from the laboratory reference frame. Hence, in the literature the interchange mode is typically identified with some nonzero frequency in the laboratory frame. Additionally, the mode is predicted to have moderately long vertical wavelengths [5].

3.2 Drift Waves

Drift waves were originally discovered in the 1960's and their properties were extensively studied in Q–machine plasmas [3]. They are sometimes referred to in the literature, especially in TORPEX papers, as the "drift–interchange" instability, reflecting their close relationship with the ideal interchange instability (see, for example [16]).

While drift waves require a plasma density gradient to form, they are not driven unstable by the gradient itself but require another influence, such as resistivity, magnetic curvature, finite electron mass, or Landau damping to become unstable [16]. Most of the work in the Helimak has focused on instabilities caused by the finite resistivity of the plasma. While not necessarily considered a resistive device, plasma resistivity is inversely proportional to $T_e^{\frac{3}{2}}$ and, given the much lower temperatures in the Helimak as compared to a tokamak, there is a correspondigly greater resistivity than in higher temperature devices.

Qualitatively, drift waves in a cylindrical plasma closely resemble the flute instability shown in Figure 3.1. However, the major difference is an important one that will be critical to measurements made and conclusions drawn in this work. Unlike the interchange instability in which all motion is perpendicular to the magnetic field, leading to $k_\parallel = 0$, drift waves have a parallel component that produces an often small $k_\parallel \neq 0$. This can be clearly seen in Figure 3.3 (figure from [15]).

Drift waves arise from a fluid description of a plasma. In their 2006 paper, Perez and Horton derive an expression for the drift wave growth rate in a Helimak plasma starting with a Braginskii two–fluid model that describes each species of the plasma separately:

$$m_s n_s \frac{d}{dt}\mathbf{v}_s = -\nabla p_s + e_s n_s \left(\mathbf{E} + \mathbf{v}_s \times \mathbf{B}\right) + \mathbf{R}_s, \tag{3.2.1}$$

where s may be either e or i [3]. The analysis continues in the usual way by assuming that all fluctuating quantities can be described as the sum of a stationary and a fluctuating quantity. The fluctuating quantity is then represented as a complex exponential whose derivatives are easily taken. Finally, the following dispersion relation

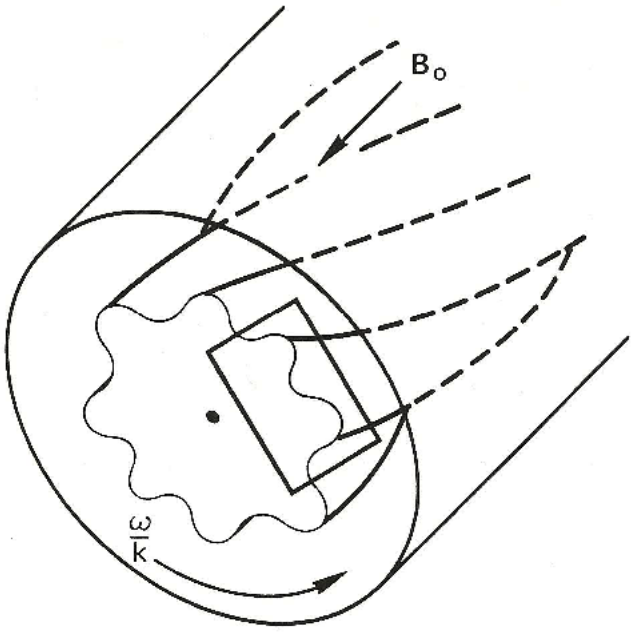

Figure 3.3: Illustration of a drift wave propagating in a cylindrical plasma

is produced:

$$\left(1 + k_\perp^2 \rho_s^2\right) \tilde{\omega} = \omega_* - \omega_D + i \frac{\tilde{\omega}\left(\omega_* - \tilde{\omega}\right)}{\nu_\parallel}. \tag{3.2.2}$$

In the above expression, the frequency is given as $\tilde{\omega}$, the Doppler–shifted frequency in the plasma frame: $\tilde{\omega} = \omega - \mathbf{k}_\perp \cdot \mathbf{v}_E$. Also, ω_* is the diamagnetic drift frequency and ω_D is the grad–B/curvature drift. These are defined by:

$$\omega_* = k_\perp v_d = \frac{k_\perp T_e}{eBL_n}, \tag{3.2.3}$$

$$\omega_D = \frac{2k_\perp T_e}{eBR_c}. \tag{3.2.4}$$

Simplifying and rearranging Eq. (3.2.2) for large $\nu_\parallel$ leads to the expression for the drift wave growth rate given by Perez and Horton [3]:

$$\gamma_k \approx \frac{\omega_*\left(\omega_* k_\perp^2 \rho_s^2 + \omega_D\right)}{\nu_\parallel \left(1 + k_\perp^2 \rho_s^2\right)^3}. \tag{3.2.5}$$

In the analysis chapters of this dissertation (Chapters 6 and 7) it will be useful to know how γ_k depends explicitly on $k_\perp$. While the exact values will not be necessary, the general shape of the curve will be of interest. Substituting the expressions given above for ω_* and ω_D in order to show their $k_\perp$ dependence explicitly and then dropping all constant multiplicative terms yields an expression which can be plotted to show the general shape of the γ_k curve:

$$\gamma_k \propto \frac{R_c k_\perp^4 \rho_s^2 + 2 L_n k_\perp^2}{\left(1 + k_\perp^2 \rho_s^2\right)^3} \tag{3.2.6}$$

Plugging in for the known values, $R_c \approx 1.1\,\mathrm{m}$, $L_n \approx 0.2\,\mathrm{m}$, $\rho_s \approx 0.0205\,\mathrm{m}$, and plotting for a range of $k_\perp$ values gives the result seen in Figure 3.4. The maximum occurs near $k_\perp \approx 61\,\mathrm{m}^{-1}$, or near $k_\perp \rho_s \approx 1.26$.

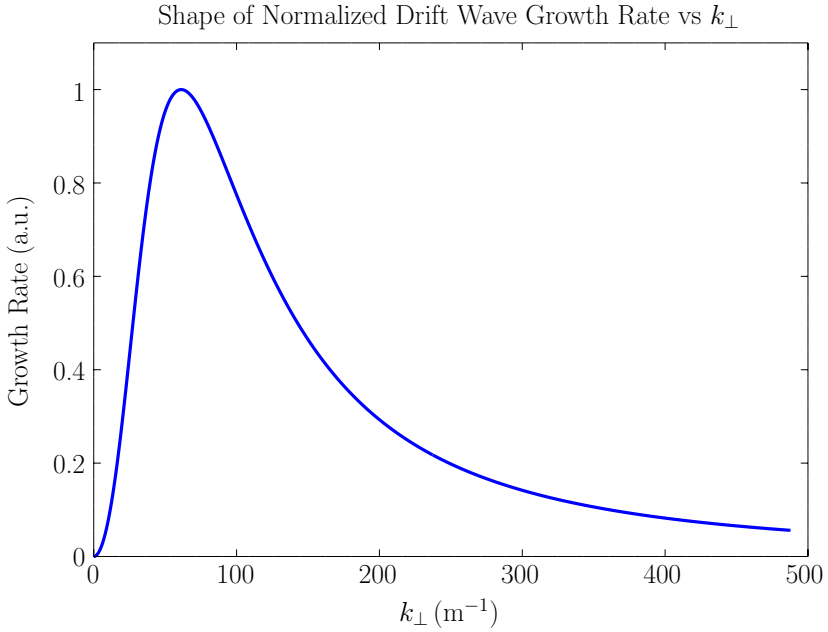

Figure 3.4: Shape of drift wave dispersion relation with Helimak parameters

3.3 Methods of Differentiation Between Drift Waves and Interchange Instabilities

While the theoretical differences between drift waves and the interchange instability are simple enough, in experimental work the distinction is rarely so trivial. This section reviews some of the literature on the distinction between different instabilities. The techniques discussed here are those that are either used later in this dissertation or those which have been proposed but which could not be implemented correctly due to the nature of the Helimak plasma and its instrumentation.

Theoretically, the only measurement that needs to be made is that of $k_\parallel$. A value of $k_\parallel$ equal to zero would determine that the ideal interchange instability dominates while a nonzero value would indicate the presence of drift waves. However, in practice this measurement is tricky (see Section 5.2). Compounding the difficulty is the fact that experimental data are always noisy. Hence, a look at some of the other proposed differentiation methods is instructive.

In a 2010 PRL paper, Ricci and Rogers discussed the transition from the interchange instability to drift waves in a SMT [5]. Based on global three dimensional simulations and comparisons with experimental results from the TORPEX device [16] they conclude that such a magnetic field geometry has three regimes dominated by distinct plasma instabilities. These are the ideal interchange regime, the resistive interchange regime, and the drift wave regime. They concluded that the interchange mode should dominate the plasma at high pitch and posited that the newly–recognized resistive interchange mode should dominate at low pitch. They found that drift waves would dominate only at lower collisionality than typically seen in TORPEX plasma.

In order to differentiate the various regimes, Ricci and Rogers define two unitless parameters called $\alpha_\perp$ and $\alpha_\parallel$ as:

$$\alpha_\perp = \frac{2\pi N \rho_s c_s}{0.3 L_v R \gamma_I}, \tag{3.3.1}$$

$$\alpha_\parallel = \frac{1}{2\gamma_I \hat{\nu}} \left(\frac{L_v c_s}{2\pi N R \rho_s} \right)^2, \tag{3.3.2}$$

where γ_I is given by Eq. (3.1.4), ρ_s is the Larmor radius at the sound speed, c_s, N is the number of field line turns contained in the vertical vessel height, L_v, R

is the radius of curvature of the magnetic field, and $\hat{\nu}$ is an adjusted collisionality. They determined that for $\alpha_\perp \lesssim 1$ the ideal interchange mode would be favored as an instability and that for $\alpha_\parallel \lesssim 1$ the resistive interchange mode would be favored.

When applied to the Helimak, however, the results are slightly different than those in TORPEX. For the relevant pitches used in the Helimak the calculated values of these two parameters are shown in Table 3.1.

R (Ω)	$\alpha_\perp$	$\alpha_\parallel$
2.7	0.207	9680
3.3	0.246	6830
3.6	0.262	6010
5	0.342	3540
10	0.695	856
15	1.20	288
20	1.68	146
25	2.94	47.9

Table 3.1: Theoretical $\alpha_\perp$ and $\alpha_\parallel$ values for Helimak plasma

Based on the these values it is clear that $\alpha_\perp$ is a potentially interesting parameter in the Helimak while $\alpha_\parallel$ is not. The values for $\alpha_\perp$ vary across the proposed cutoff point of $\alpha \approx 1$ with the highest five Helimak pitches, 2.7, 3.3, 3.6, 5, and 10 Ω falling below and the three highest pitches, 15, 20, and 25 Ω residing above. Hence, this theory predicts that at the higher Helimak pitches the ideal interchange mode will dominate. Meanwhile, the values of $\alpha_\parallel$ for the Helimak pitches used are always much larger than 1, implying that the resistive interchange mode does not play a role in the plasma dynamics. To fill in the gap, Ricci and Rogers expect drift waves to dominate at these pitches.

For the present work, their methods of distinguishing between the various modes are also particularly interesting. To experimentally determine the regimes in which the various modes dominated, Ricci and Rogers calculated the mode numbers of the plasma fluctuations in the vertical and toroidal directions. They then related these mode numbers to $k_\parallel$ and k_z and drew conclusions about the dominate modes. An attempt to apply these methods was completed as part of the present work. However, it was found that in the Helimak no clearly defined mode numbers exist. This is due to the fact that the physical distances in the Helimak are much greater than those in

TORPEX. High values of cross–correlations do not persist over the length of an entire magnetic field line, yielding any mode numbers thus measured suspicious. In other words, while it certainly appears that large–scale structures exist in the machine, the stochastic vagaries of plasma motion make it extremely difficult to measure these structures, and hence their mode numbers, over long distances. Unfortunately, the mode number approach utilized on TORPEX is not useful on the Helimak and its results will not be reported in this work.

Another method that has been used to distinguish interchange instabilities is the phase shift between $\tilde{n}$ and $\tilde{\phi}$ [17]. Phase shifts less than $\pi/4$ are associated with drift waves while phase shifts in the range of $\pi/4 - \pi/2$ are associated with interchange instabilities. However, previous experiments have shown that there is no consistent pattern in the phase shifts in Helimak data. Hence, this approach will not be used either. A similar lack of correlation occurs in TORPEX [16].

3.4 Other Modes Not Considered

In this dissertation, only interchange instabilities and drift waves are considered as candidate modes to explain the fluctuations present in the Helimak plasma. This section will briefly describe why other common plasma instabilities and waves were not considered. The uniting thread of this section is that many modes typical on other plasma devices do not theoretically arise from the Helimak geometry. One such example is the resistive interchange mode, which was originally considered a candidate instability until the theoretical comparisons done in Section 3.3 showed that it was not likely to contribute to the experimental behavior.

Another commonly mentioned instability, actually a general fluid instability rather than a plasma–specific mode, is the Kelvin–Helmholtz instability. This mode goes unstable for large enough velocity shear between two layers of fluid and is common in linear devices and Q–machines. In the case of the Helimak, there is velocity shear across the device in the radial direction [18]. For a neutral fluid, the cutoff for stability is given by:

$$\frac{N^2}{U_r^2} > \frac{1}{4}, \tag{3.4.1}$$

where N is the Brunt–Väisälä frequency, given by $N^2 = -g/L_n$ and U_r is the flow shear in the radial direction [19]. This shows that not shear alone, but a particular

balance of shear and scale length, is required for instability. Based on the typical Helimak values of $L_n = 0.2\,\mathrm{m}$ and $U_r \approx 5000\,\mathrm{s}^{-1}$, Eq. (3.4.1) gives $10^{-4} \not> 0.25$. Hence, while there is strong velocity shear in the Helimak, the scale lengths are not commensurate and the Kelvin–Helmholtz instability is expected to be stable.

Finally, there has been some discussion in the past about the role of Alfvén waves in the Helimak plasma. Alfvén waves are hydromagnetic ion waves that propagate parallel to $\mathbf{B}_0$ with a characteristic velocity known as the Alfvén velocity: $v_a \equiv B/\sqrt{\mu_0 \rho}$. While they are a wave, not an instability, they are theoretically an important consideration because they cause magnetic field fluctuations which could effect the results presented here, particularly those involving the alignment of the MPD (see Section 5.2). However, they are not believed to be important in the Helimak. Thus, this work will ignore them for three reasons:

1. Plasma β in the Helimak is small, $\approx 10^{-5}$. With small β, magnetic effects, such as field line bending caused by Alfvén waves, can be ignored. Only for β several orders of magnitude higher than in the Helimak are such effects important.

2. The Alfvén velocity calculated for a typical Helimak plasma is on the order of $10^6\,\mathrm{m/s}$. While this is on the order of the electron thermal velocity, it is much faster than the ion thermal velocity, which is on the order of 100. Since Alfvén waves are an ion mode this value is more important. At such a tremendous difference the slow ions would not feel the Alfvén velocity if it were present.

3. Experimentally, attempts have been made to measure magnetic fluctuations in the Helimak. No fluctuations have been reliably measured, confirming the above two points.

Chapter 4

Equilibrium and Turbulent Profiles

This chapter presents and discusses both the equilibrium and turbulent profiles of typical Helimak plasma under a variety of conditions. It begins, in Section 4.1 with equilibrium profiles of the ion density, electron temperature, and floating potential for both grounded and biased cases. Section 4.2 discusses the turbulent amplitudes in the device for similar cases.

4.1 Equilibrium Helimak Data

Using the techniques described in Section 2.2 the following equilibrium profiles for a typical Helimak plasma can be obtained. In the following section profiles for various pitches with will given for the density, electron temperature, and floating potential, for probes on both the top and the bottom of the machine. All of these profiles are from argon plasma. All were produced at 6 kW of microwave power and 800 A of total magnetic field current. It should be noted that the bias plate used for these equilibria is plate 3, not the typically used plate 2. The reasons for this are explained in Section 4.2.

4.1.1 Density

Figures 4.1 and 4.2 show the smoothed density profiles of a typical discharge with no applied plate bias. Figure 4.1 was taken using probes on the top of the machine while Figure 4.2 was taken using probes on the bottom. Several important characteristics are immediately discernible. The first is that, while the bottom profiles are nearly identical, the top profiles show more variation, especially at lower radii (on the high–field side, or HFS). At higher pitches the density peaks of the profiles are lower by about a factor of 1.5 and shifted inward by over 10 cm. At present we are unsure how to account for this change, though it may be worth noting that the microwave waveguide enters the machine near the bottom. Perhaps this gives the plasma on the bottom a better chance at first pass absorption and leads to more consistent densities.

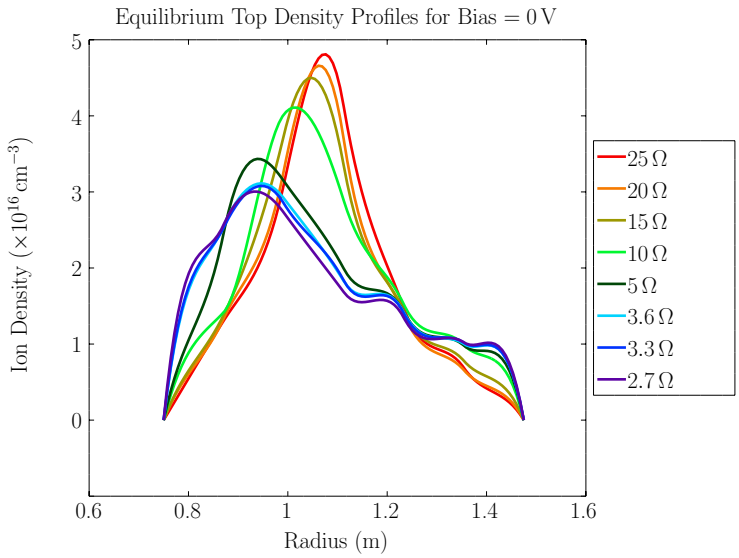

Figure 4.1: Density profile from the top of the machine using grounded plates

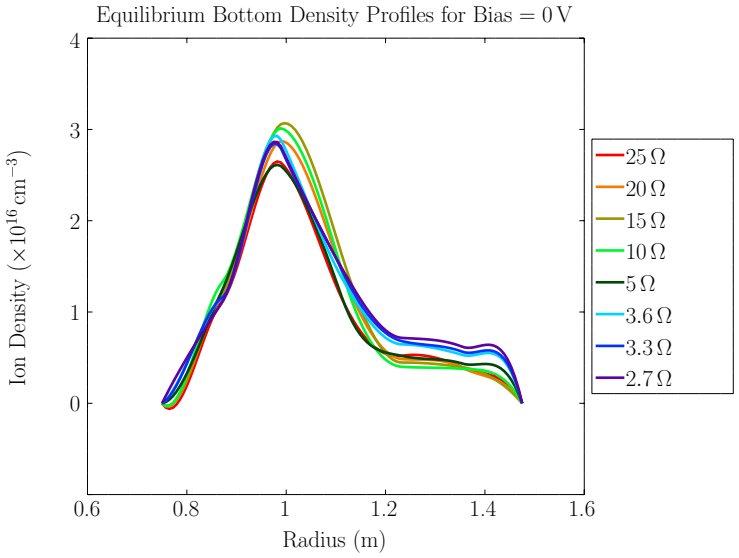

Figure 4.2: Density profile from the bottom of the machine using grounded plates

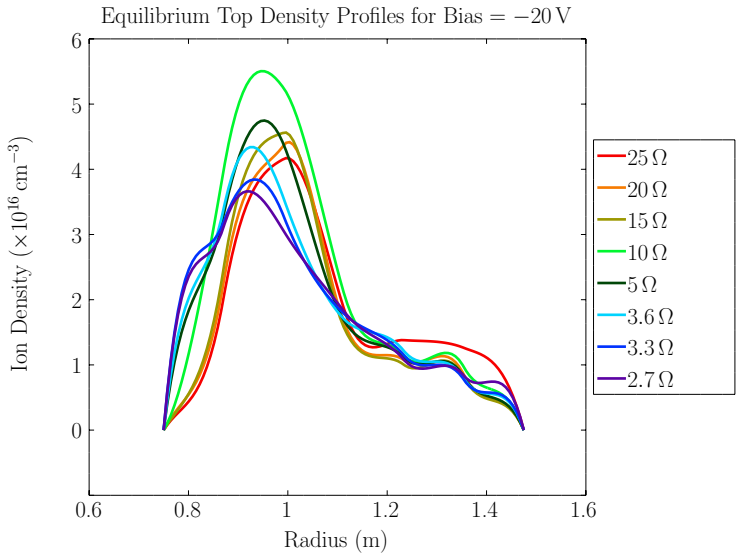

Figure 4.3: Density profile from the top of the machine using plates biased to −20 V

For the other, "normal," peaks, the density maximum is consistently located between $R = 1.0\,\mathrm{m}$ and $R = 1.1\,\mathrm{m}$ and does not vary much with pitch. This is consistent with the estimated radial position of the upper hybrid resonance. As noted in Section 2.1.1, it is believed that first pass absorption is quite low. Hence, it is unclear exactly why the density maximum should be so well correlated with the upper hybrid resonance location. Future work plans to investigate this more closely.

As illustrated in Figures 4.3 and 4.4, the application of 20 volts of negative bias changes the density profiles, though not by much. The top traces, Figure 4.3, at high pitch shift back outward slightly while those at low pitch shift inward to meet them, with all peaks in the neighborhood of $R = 1.0\,\mathrm{m}$. For the top probes the maximum density value remains fairly constant while for the bottom probes the maximum density increases at high pitches by about one–third. The most obvious change occurs out near the bias region, where the profiles for both top and bottom have flattened considerably. Figure 4.5 shows the average values of the slope of the profile for each resistance for both the top and bottom, with and without negative bias. Here, the average for each pitch is taken from $R = 1.2\,\mathrm{m}$ and out to look at the behavior in the obviously flattened region only. It is clear from the figure that the application of bias flattens the profile on the outer half of plate 3, the bias plate, and on plate 4, the plate used for most of the measurements in this work. The

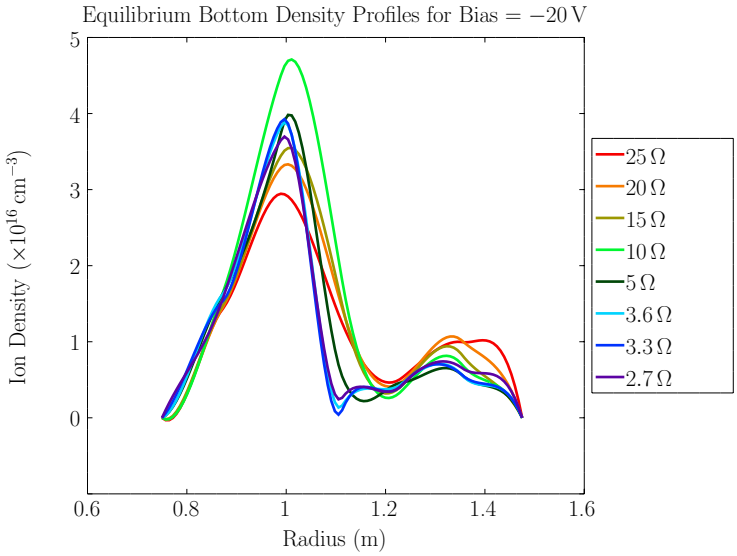

Figure 4.4: Density profile from the bottom of the machine using plates biased to $-20\,\mathrm{V}$

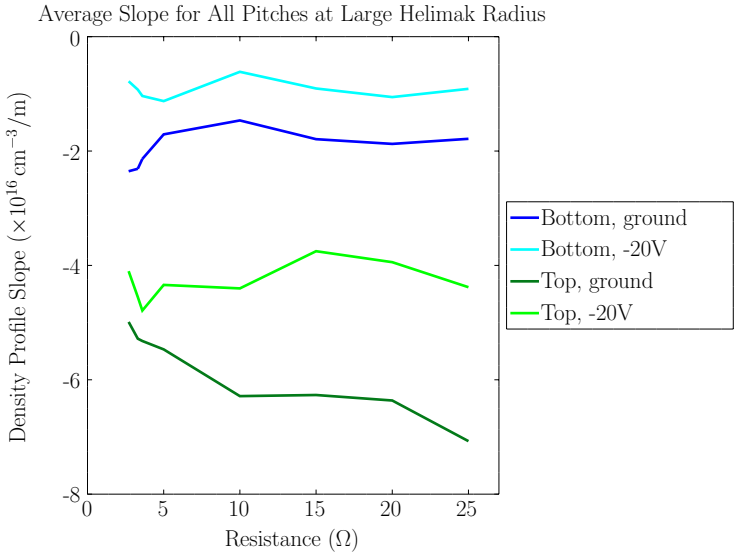

Figure 4.5: Average slope for each resistance at large radius, $R > 1.2\,\mathrm{m}$, with and without bias

interchange instability, discussed in Section 3.1, relies on the density gradient to be driven unstable. Hence, the flattening of this region is an important consideration in the turbulence reduction discussed in Section 4.2.

For the application of positive bias the density peaks shift again. For +10 V the results are shown in Figures 4.6 and 4.7. For the top profiles, Figure 4.6, two very different responses are seen. For the high pitches the density maximum remains fairly constant while the peak shifts inward by almost 10 cm. The lower density tail of the profile also drops off much more slowly and displays a secondary local maximum at the location of the bias plate (about $1.1 - 1.3$ cm). The lower pitches respond to the addition of positive bias by shifting in the opposite direction – outward – by about 10 cm, placing their respective maxima squarely in the center of the bias plate. This occurs while the maximum value of density remains constant.

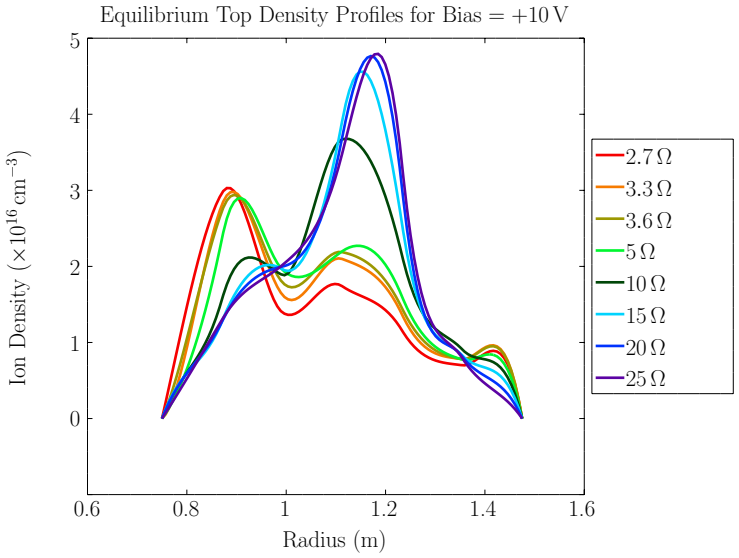

Figure 4.6: Density profile from the top of the machine using plates biased to +10 V

We note the strange opposite behavior of the low and high pitch profiles at positive and negative bias. At negative bias the peaks shifted towards each other compared to the grounded case with the high–pitched peak moving radially outward and the low–pitched peak moving inward. At positive bias the exact opposite occurred, resulting in a larger radial gap between the two sets of density maxima. This odd behavior will not be further explored in this work, though its significance may be worth exploring at a later time.

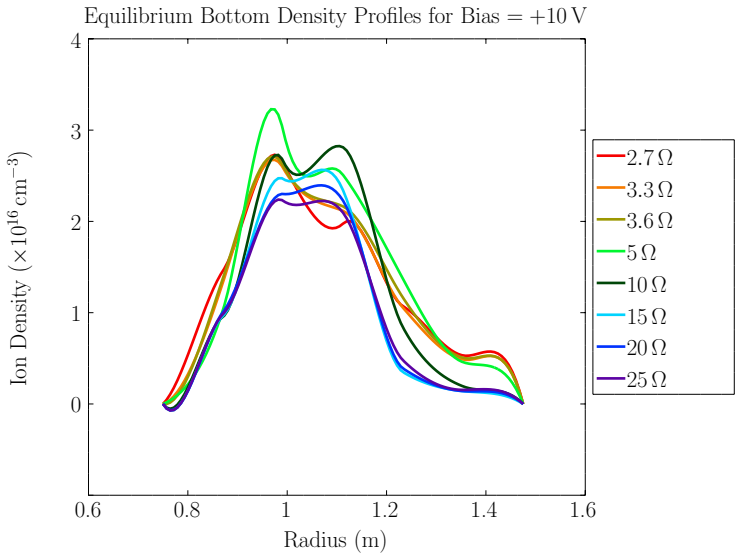

Figure 4.7: Density profile from the bottom of the machine using plates biased to +10 V

The bottom profiles react to the application of positive bias differently. The profiles in Figure 4.7 no longer have sharp, discernible maxima. Instead, the profiles are rounded on top and exhibit a comparatively flat density for approximately 20 cm. This flat spot is, however, aligned closely with the location of the previous maxima, indicating that the traces have not shifted radially. The maximum value itself has dropped off slightly from the grounded case. Additionally, the profiles are still rather consistent across all pitches.

As a final set of examples, consider Figures 4.8 and 4.9. Each figure shows the profile at a single pitch and demonstrates how the profiles at a fixed magnetic connection length vary with bias. For simplicity, only profiles from the bottom plates are shown.

These figures clearly show the shifts of peaks and maxima that occur at bias is changed at a given pitch. For the high–pitch case, Figure 4.8, the peak is raised and the tail flattened at negative bias and shifted peaks at positive bias. At a higher positive bias than that shown in Figure 4.6 the density peak again shifts outward. For the low–pitch case, Figure 4.9, it is seen how the effects of negative bias are mostly limited to a flattening of the tail while positive bias leads to a complete shift of the peak in the outward radial direction, towards the bias plate.

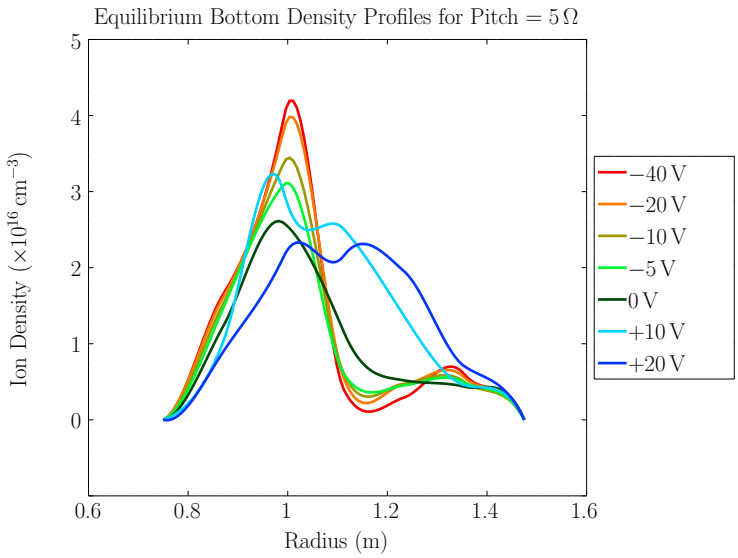

Figure 4.8: Density profile from the bottom of the machine showing all biases for pitch of 5 Ω

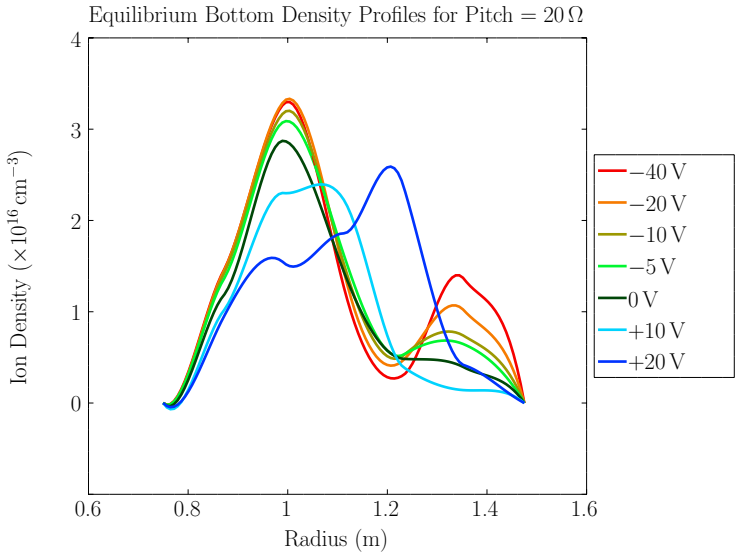

Figure 4.9: Density profile from the bottom of the machine showing all biases for pitch of 20 Ω

Of further interest is the general behavior near the bias plate. For the negatively–biased traces at all pitches a local density minimum occurs near $R = 1.2\,\mathrm{m}$ which corresponds to the center of the bias plate. While this local minimum is more noticeable for a pitch of $20\,\Omega$ it is also visible, though smaller, for pitch of $5\,\Omega$. This minimum at first seems counterintuitive, as it seems reasonable to expect a maximum ion density near the source of negative bias. This seeming anomaly is explained by noting that the Helimak electrons are always more mobile than the ions. Hence, with a negative applied bias the electrons vacate quickly and some of the ions follow in order to preserve quasi–neutrality. The opposite explanation holds for the positively–biased cases where we see that, for both high and low pitches, the density maximum is actually shifted toward the bias plate. In this case the electrons move quickly toward the higher electric field and are followed by an increase in ions, again preserving quasi–neutrality.

4.1.2 Electron Temperature

Sample profiles of the electron temperature in the Helimak with grounded plates are shown in Figures 4.10 and 4.11. Figure 4.10 was taken using probes on the top of the machine while Figure 4.11 was taken using probes on the bottom.

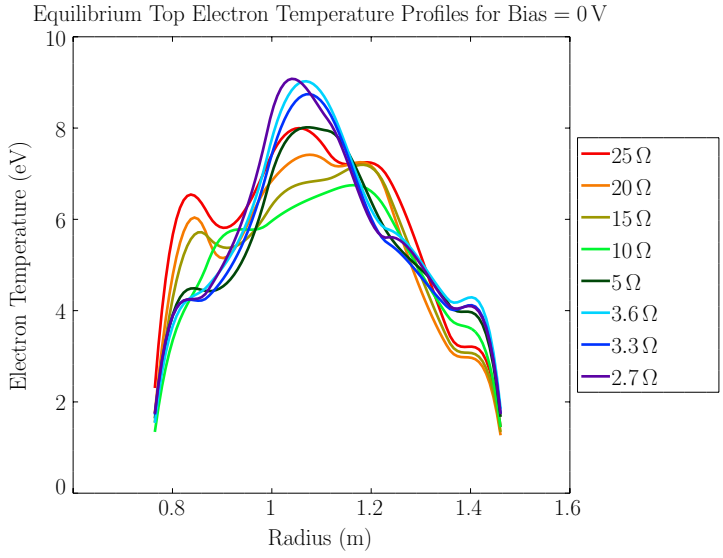

Figure 4.10: Electron temperature profile from the top of the machine using grounded plates

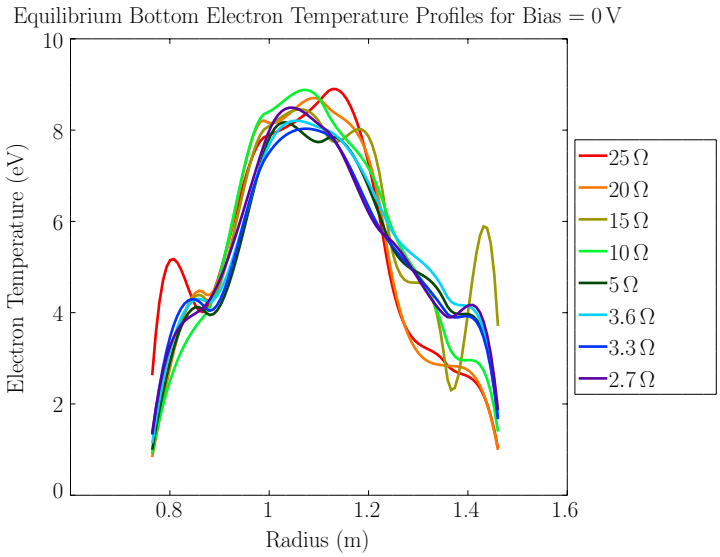

Figure 4.11: Electron temperature profile from the bottom of the machine using grounded plates

While not identical, these profiles show more qualitative similarity between the bottom and top of the machine than the density profiles. Both sets have peaks centered around $R = 1.1\,\mathrm{m}$ and maxima of approximately 8 eV. Again, however, the top profiles have some differences between high and low pitches, with the peaks at low pitch having lower temperature peaks that are also less distinct. However, the rest of the profiles are fairly symmetric about the maximum. The electron temperature profiles as measured by the bottom probes, Figure 4.11 display wider peaks than those on the top.

For the bias cases of electron temperature many of the differences are subtle and hard to differentiate based on plots of the profiles. Thus, the figures presented here are a composite of the actual profiles and the difference between the profile and the grounded case (either Figure 4.10 or 4.11), called the "Relative Electron Temperature." The relative figures were obtained by subtracting $T_{e,gnd}$ from the T_e profile of the applicable bias case. Values greater than zero indicate that the electron temperature increases when bias is applied, while values less than zero indicate a corresponding decrease.

When negative bias is applied the profiles change as shown in Figures 4.12 and 4.13. For the probes on top, Figure 4.12, the addition of bias has little effect

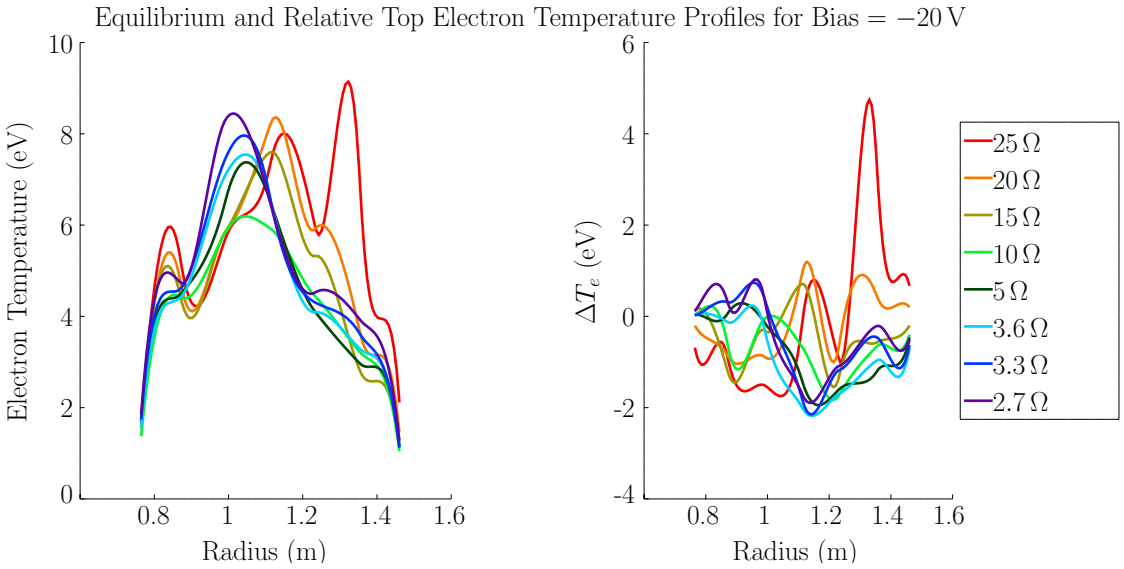

Figure 4.12: Equilibrium (left) and relative (right) electron temperature profiles from the top of the machine using plates biased to −20 V

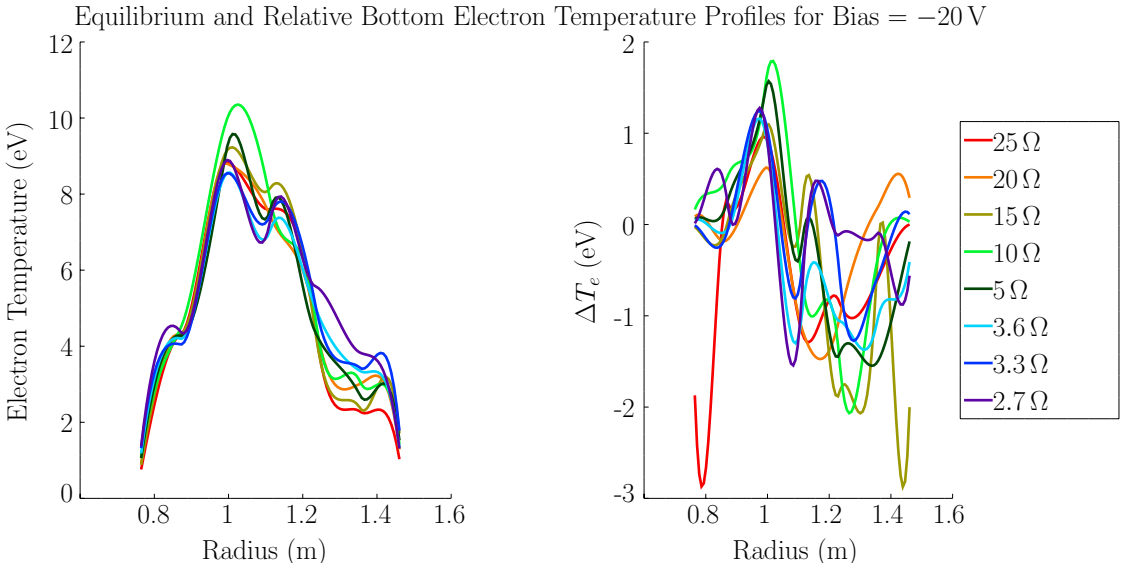

Figure 4.13: Equilibrium (left) and relative (right) electron temperature profiles from the bottom of the machine using plates biased to −20 V

on the high–pitch profiles on the HFS. The maxima drop by about 2 eV and shift slightly inward, away from the source of the bias. The electron temperature at the bias plate also drops by around 1 eV. Meanwhile, the lower pitches see a slight increase in electron temperature at and radially outward from the bias plate, with one large anomalous spike at 25 Ω. The bottom plates, Figure 4.13 see a strong decrease in the maximum value of T_e to go along with a smaller decrease just outside of the previous maximum and an increase to the inside. This creates a T_e profile with a double peak with an absolute maximum in the range of $9 - 10$ eV and a local maximum around 8 eV and radially outside. At the radius of the bias plate and outwards T_e is reduced for nearly all pitches, just as on the top plates. This is probably due to the fact that the high–energy electrons move away from the biased region most quickly.

The addition of positive bias yields the profiles shown in Figures 4.14 and 4.15.

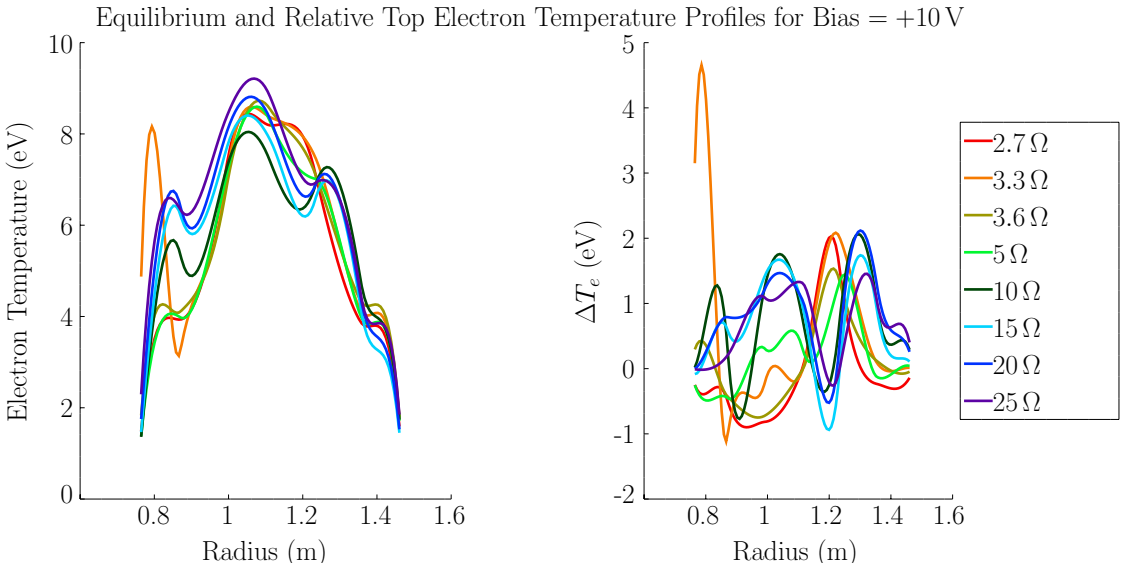

Figure 4.14: Equilibrium (left) and relative (right) electron temperature profiles from the top of the machine using plates biased to +10 V

For the probes on top of the machine, Figure 4.14 the profiles appear to have widened. The temperatures at low pitch have generally increased, except in the middle of the bias plate where they have decreased slightly. At high pitch, with the exception of the outlier at 3.3 Ω, the temperatures have generally decreased on the HFS, increased near the bias plate, and decreased slightly at larger radius. This

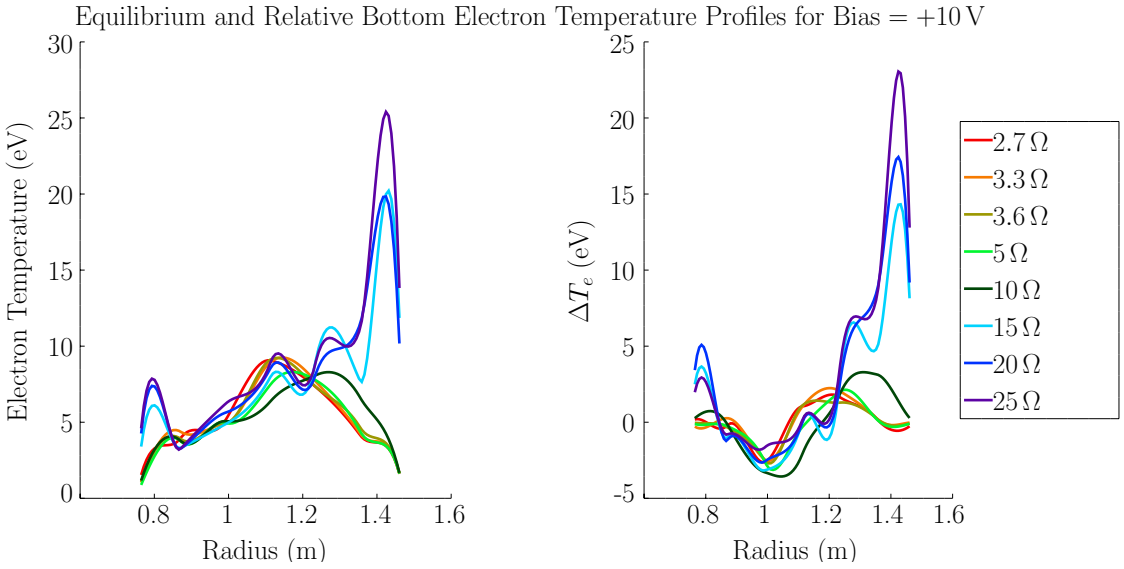

Figure 4.15: Equilibrium (left) and relative (right) electron temperature profiles from the bottom of the machine using plates biased to +10 V

behavior makes sense, as the positive bias will accelerate electrons into the region. The decrease at low pitch is harder to explain and may represent interference from some other effect. For the bottom probes, Figure 4.15 the addition of positive bias leads to several extreme outliers in temperature. While these extreme values are most likely nonsensical, it does appear from the general shape of the profile that T_e increases in this region for low pitch. There is a general increase in T_e at and outside of the bias plate for all pitches and a general decrease immediately to the inside of that plate. This leads to the profiles being skewed towards larger radius. This is a reasonable electron response to an additional positive electric field in the region.

4.1.3 Floating Potential

Figures 4.16 and 4.17 show representative floating potential profiles when the plates are grounded. As has generally been shown in this chapter thusfar, the profiles from the top and bottom of the machine do not agree. The top floating potential profile shows a contrast between high and low pitch. The profiles at high pitch show one major minimum, occurring near $R = 1.1$ m, near both the density maximum (see Figure 4.1) and the electron temperature maximum (see Figure 4.10). The profiles at low pitch, meanwhile, show two two major minima. The absolute minimum occurs

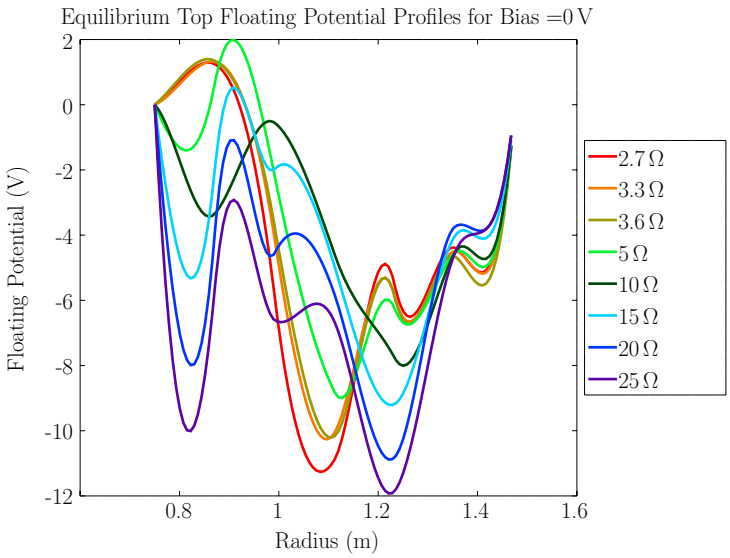

Figure 4.16: Floating potential profile from the top of the machine using grounded plates

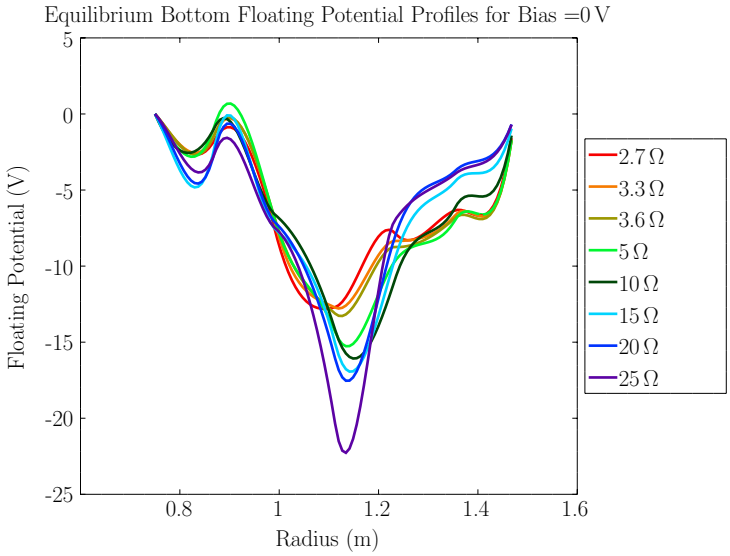

Figure 4.17: Floating potential profile from the bottom of the machine using grounded plates

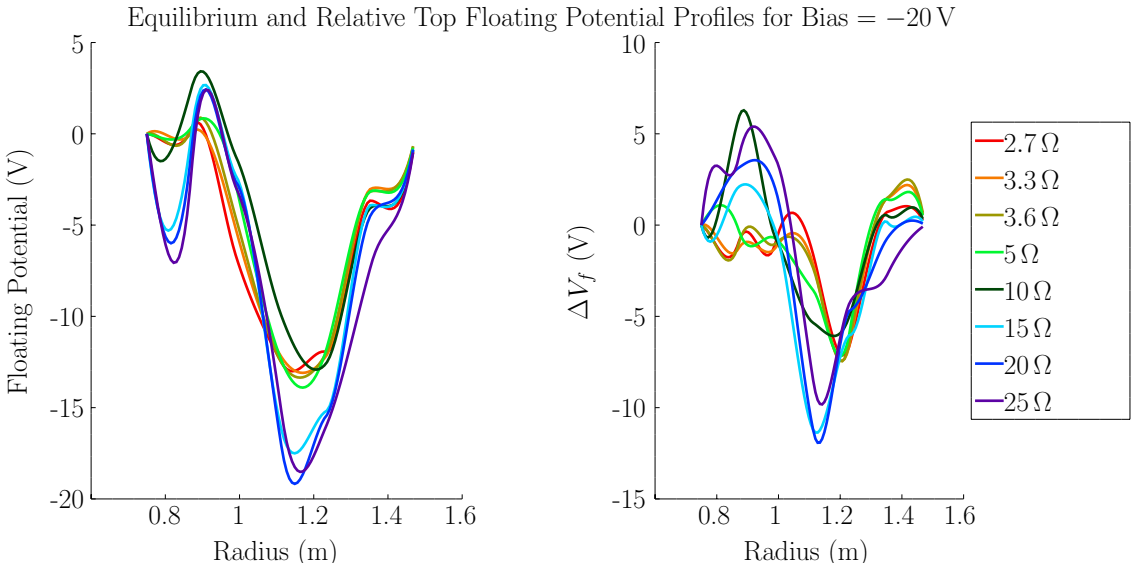

Figure 4.18: Equilibrium (left) and relative (right) floating potential profiles from the top of the machine using plates biased to −20 V

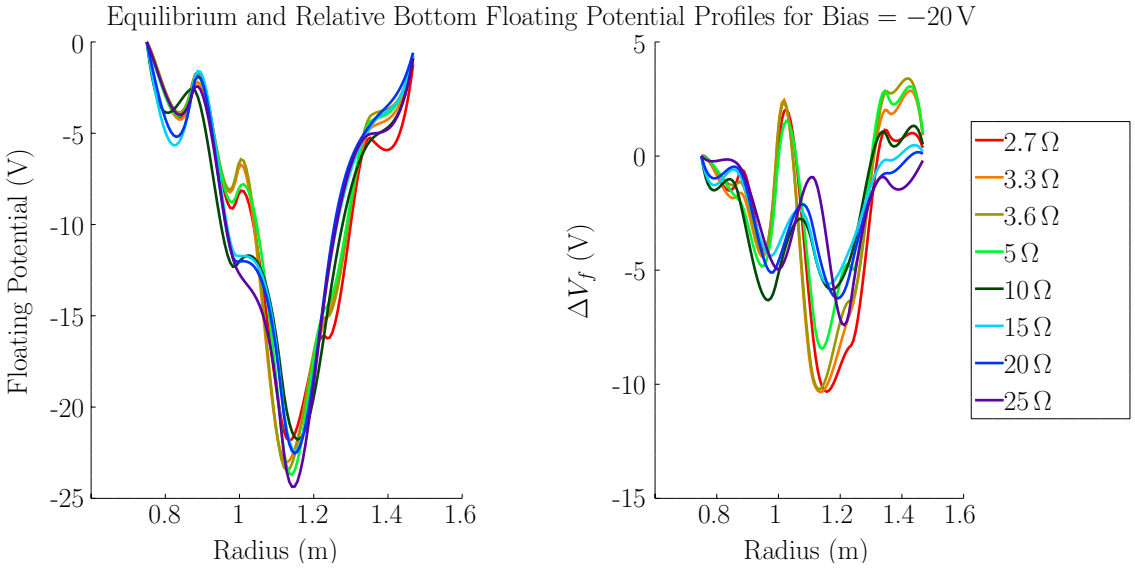

Figure 4.19: Equilibrium (left) and relative (right) floating potential profiles from the bottom of the machine using plates biased to −20 V

near $R = 1.2\,\mathrm{m}$, near the center of the bias plate. Another local minimum occurs near $R = 0.8\,\mathrm{m}$ on the HFS. It is unclear why a change in pitch would trigger the formation of another V_f minimum.

The bottom plates show a more consistent picture as far as shape is concerned. All pitches display one major minimum, all of which line up closely in R. The minimum at high pitch is slightly inside of that for low pitch, approximately aligned with its corresponding minimum on the top of the machine. The actual values of V_f are close for high pitch, falling in the range of -11 to $-13\,\mathrm{V}$. For low pitch V_f varies much more in the range -15 to $-20\,\mathrm{V}$, compared with -9 to $-12\,\mathrm{V}$ on the top plates.

As expected, the application of negative bias lowers the floating potential in the vicinity of the bias plate. On both the top, Figure 4.18, and bottom, Figure 4.19, the bias lowers the floating potential. Interestingly, the potential on the top is lowered by an extra $5\,\mathrm{V}$ for low pitches while the opposite holds true for the bottom plates, where the high pitches decrease in potential by an extra $5\,\mathrm{V}$. Other differences occur in the region away from the bias plate. For the top probes the potential remains nearly constant radially outward from the bias plate while the potential inside increases for low pitch. On the bottom, the potential mostly decreases for all radii inside of the bias plate while it increases at high pitch outside of the bias region. While the reason for these differences is not well understood, it is clear that the pitch plays an interesting role in the response of V_f to bias and that large asymmetries occur between the top and bottom of the vessel.

Again according to expectations, the application of positive bias tends to increase the floating potential under certain conditions. As seen in Figure 4.20, the probes on the top universally increase in floating potential at the location of the bias plate. Those at low pitch increase by about $10\,\mathrm{V}$, compared with $5\,\mathrm{V}$ for those at high pitch. This increase is associated with a decrease of about $5\,\mathrm{V}$ just inside of the bias plate at low pitch. For high pitch, on the other hand, the floating potential increase applies at all radii. The magnitude of the increases are approximately the same as the magnitudes of the decreases with the application of $-20\,\mathrm{V}$ of bias (see Figure 4.18). This is in agreement with the general Helimak observation that positive bias affects the plasma more strongly due to the lower inertia that the electrons have compared to the ions.

For the bottom, the effect of positive bias is stronger with increases of up to

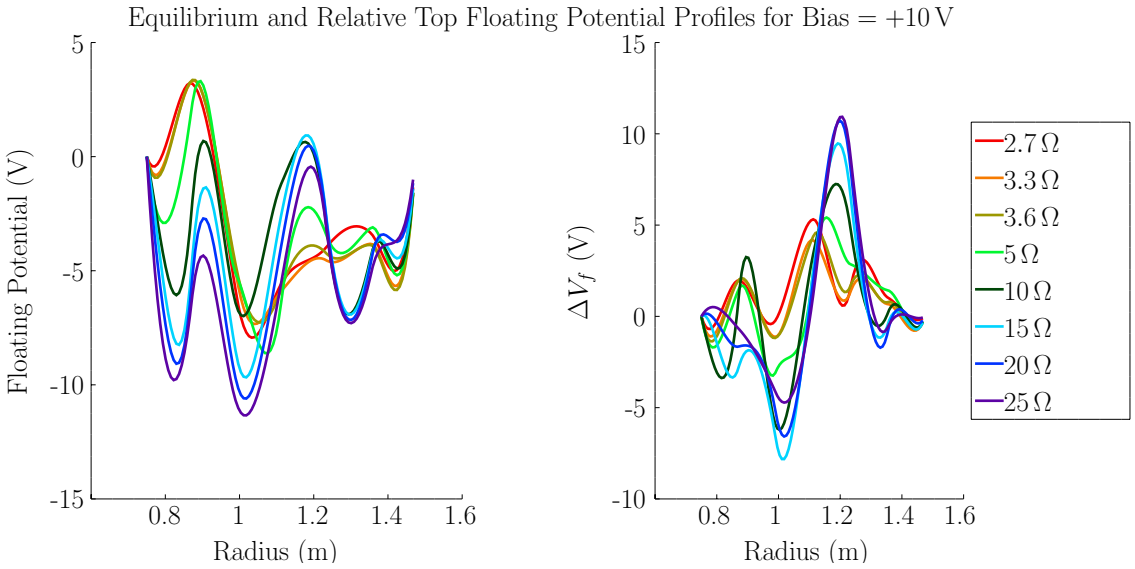

Figure 4.20: Equilibrium (left) and relative (right) floating potential profiles from the top of the machine using plates biased to +10 V

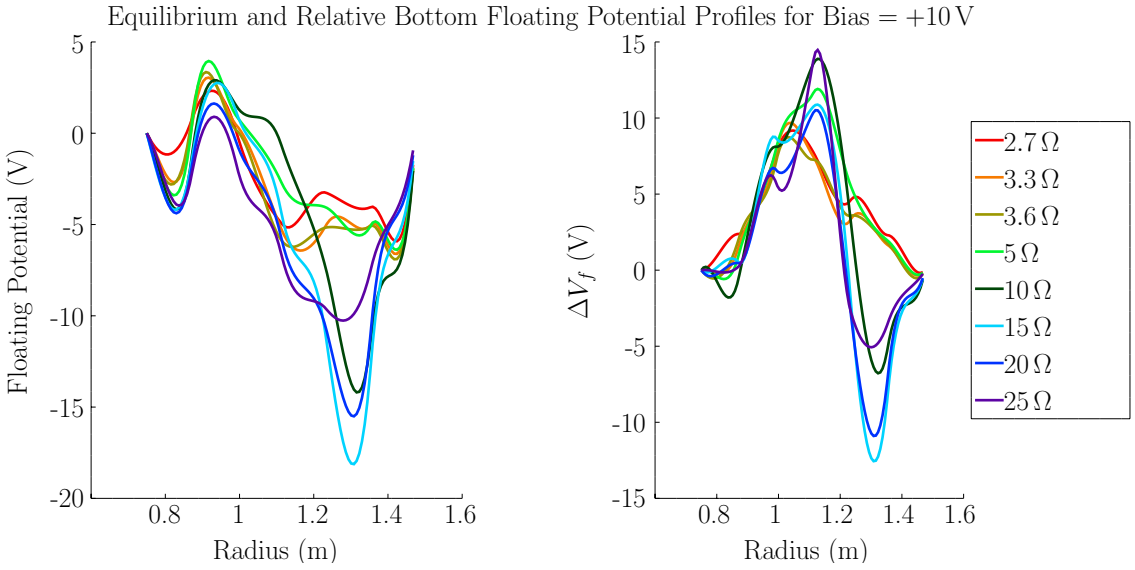

Figure 4.21: Equilibrium (left) and relative (right) floating potential profiles from the bottom of the machine using plates biased to +10 V

15 V at low pitch and 10 V at high pitch. While an increase in V_f occurs for high pitch at all radii, the low pitches experience a drop in V_f near the outer edge of the bias plate at about $R = 1.3$ m. This drop falls in the range of $5 - 10$ V and results in a deep well in the profile at that radius. While the magnitude of the change at high pitch, ≈ 10 V is about the same as that at the application of -20 V, the magnitude of the change at low pitch, ≈ 15 V, is significantly larger than the corresponding change at negative bias, 5 V.

4.2 Helimak Turbulent Amplitude Profiles

In this section the profiles of turbulent amplitude inside the Helimak are shown and compared against each other at various biases, radii, and pitches. This section paints a complete picture of how the bias amplitudes respond to various parameter changes. Grounded profiles are discussed in Section 4.2.1 and biased profiles are discussed in Section 4.2.2.

The bias amplitudes in the Helimak are historically calculated as $\frac{\Delta n}{n}$ where n is the average value of the density over the time period during which the F–96 takes data and Δn is the variance of the density signal. The average, n, is always negative so the absolute value is taken.

4.2.1 Grounded Turbulence Profiles

Figure 4.22 shows the standard case of Helimak turbulent amplitudes with no bias. The first important characteristic of this data is that it clearly shows that the turbulent amplitude increases as radius increases. The second is the generally high levels of turbulence at all radii for all pitches. The Helimak was designed, in part, to be a turbulent device so that the properties of turbulence could be studied. This is accomplished through the weak magnetic field, which does not contribute strongly to confinement, as well as the magnetic field geometry with its open magnetic field lines. Compared with far more modest tokamak values of turbulent amplitude it is obvious that the Helimak fulfills its purpose in this regard. The amplitudes of approximately 60% on parts of plates 3 and 4 are contrasted by more moderate, but still relatively high, values near $20 - 30\%$ close to the density maximum.

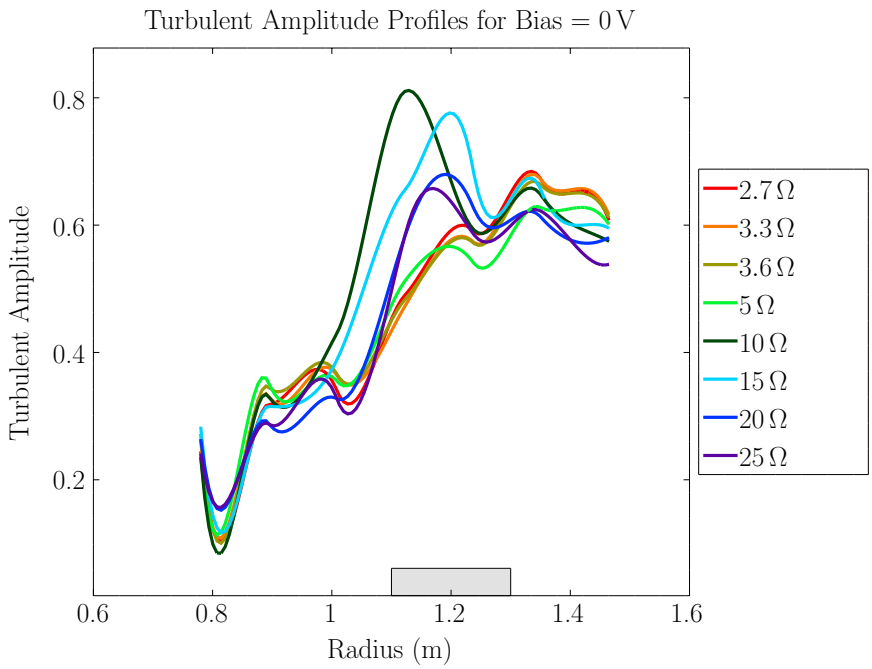

Figure 4.22: Turbulent amplitudes in the grounded case

4.2.2 Biased Turbulence Profiles

As has been reported extensively in previous works (see, for example [20]), Helimak plasma turbulent amplitudes respond strongly to an applied bias. For negative bias the amplitudes typically decrease, while for positive bias values they have been shown to increase at certain radii and decrease at others. In the plots that follow the relevant grounded case will be plotted along with the biased cases for reference where relevant.

In past Helimak work the bias was applied on plate 2. Previous results showed strong effects due to bias primarily on plates 2 and 3. For this work the bias was moved further out onto plate 3 so that its effects could be seen on plate 4 as well. This was desirable because the radial location of the MPD lines up with plate 4 and thus the effects of bias on $k_\parallel$, which requires the MPD in order to be measured, could be studied (for the results of this piece of the experiment, see Section 7.1). The bias plate, plate 3, is indicated for reference in all of the following plots as a small gray rectangle spanning the distance between $R = 1.1\,\mathrm{m}$ and $R = 1.3\,\mathrm{m}$.

For small magnitudes of negative bias Figure 4.23 shows the relative turbulent

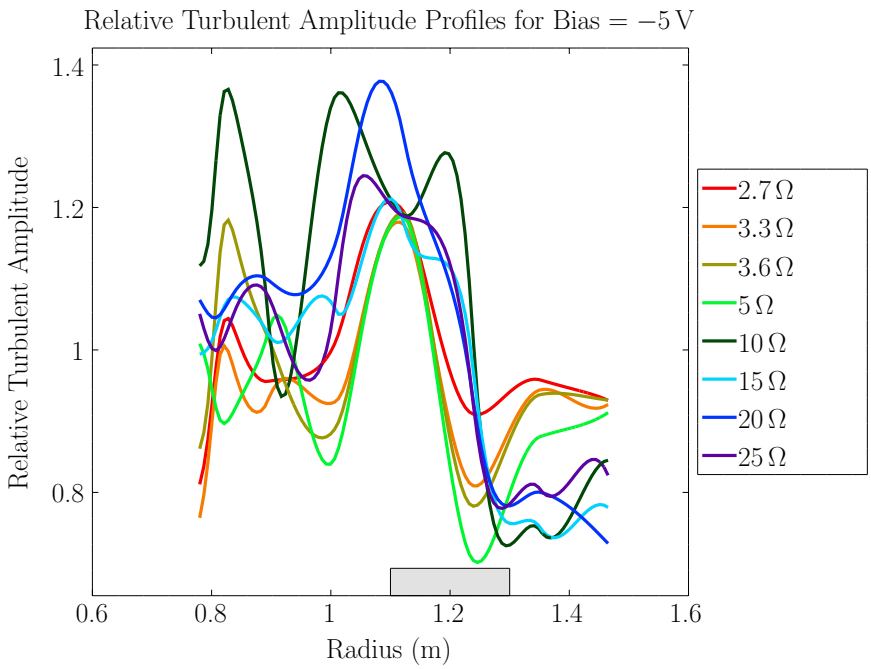

Figure 4.23: Turbulent amplitudes at a bias of $-5\,\mathrm{V}$

amplitude profiles for all pitches. This is a composite plot taken by dividing the turbulent amplitudes at $-5\,\mathrm{V}$ by the grounded amplitude values seen in Figure 4.22. Hence, values greater than one indicate an increase in turbulent amplitude with bias and values less than one represent a decrease in turbulent amplitude. Values near one represent little or no change, within experimental error.

Figure 4.23 shows the changes in turbulent amplitudes with these parameters. On the HFS of the machine the amplitudes are relatively constant, with one outlier at $10\,\Omega$. Based on past experiments these probes are too far from the bias application to feel strong effects. On the outer half of plate 2 and the inner half of plate 3 ($R \approx 1.0 - 1.2\,\mathrm{m}$) the turbulent amplitudes are increased by about 20%. It is only on the outer half of plate 3 and on plate 4 that the turbulent amplitudes are decreased. At high pitch there is only a decrease of a few percent while at low pitch the decrease can be well over 20%.

At stronger negative bias, as seen in Figure 4.24, the same general pattern holds, though with differing amounts of reduction or amplification. For the same region of amplification identified in Figure 4.23, $R \approx 1.0 - 1.2\,\mathrm{m}$, the amplification

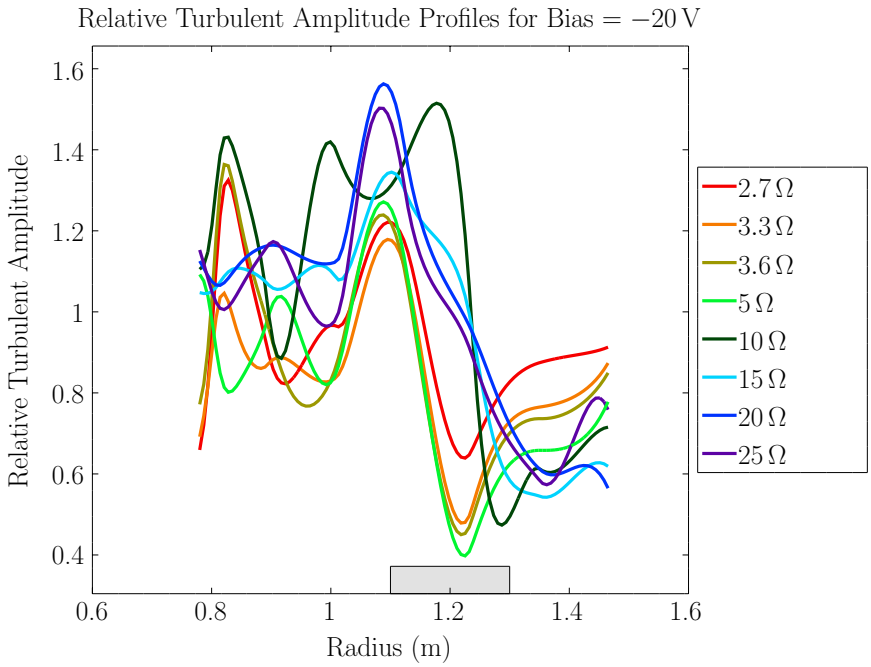

Figure 4.24: Turbulent amplitudes at a bias of −20 V

level can reach as high as 50% at the lowest pitches. For the higher pitches the amplification is only slightly increased above 20%. For the outer region of the plasma reduction again takes place. In this case, the high pitches undergo reduction of about 10–20% while the low pitches can have bias reduction of up to 40–50%.

While the identification of the instabilities will be delayed to Chapters 6 and 7, it is clear that, in the region of the MPD, the dominant instability at low pitch is more strongly affected by negative bias than that at high pitch. While the complete mechanism is unknown, the bias does more to disrupt the instabilities at low pitch.

Meanwhile, Figure 4.25 shows the relative turbulent amplitudes at positive bias. This figure shows decreased turbulent amplitudes at almost all radii. Near the center of the bias plate the bias reduction reaches levels as large as 80%. The reduction extends beyond the edge of plate 3 into the inner regions of plate 4 where the MPD is located. However, at large radii the turbulence is amplified for all pitches. The lowest pitches are the most strongly affected with up to 50% amplification. The high pitches have more moderate amplification values of 10–20%.

It is also instructive to exam turbulent amplitude profiles for each pitch plotted

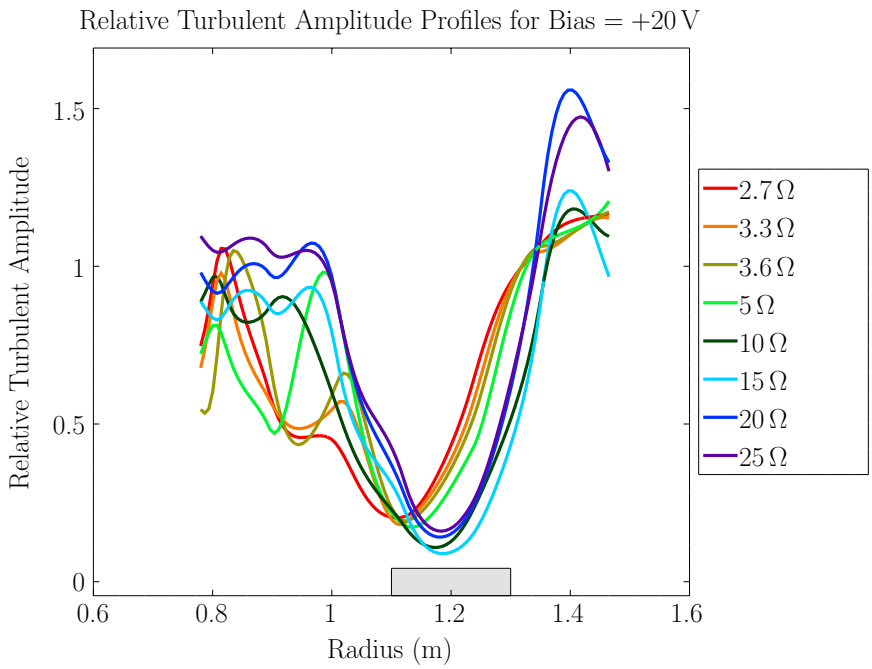

Figure 4.25: Turbulent amplitudes at a bias of +20 V

for all measured bias values. Figure 4.26 shows such a plot for a high pitch of 5 Ω. Here, the dark green line represents the grounded turbulent amplitude that serves as a standard of comparison. In the range $R \approx 1.0 - 1.2$ m the turbulence is amplified at negative bias and reduced for positive bias. At slightly larger radii there is reduction at all bias values. Further out, on plate 4, there is a nearly sequential response to the bias. For positive bias in parts of this region the bias is amplified for 10 V and more strongly amplified for 20 V. Likewise, the bias is suppressed somewhat at −5 V, more at −10 V, and saturates past −20 V with little change between −20 V and −40 V.

Figure 4.27 shows that a similar response occurs at low pitch (20 Ω). The bias is amplified in the region $R \approx 1.0 - 1.2$ m for negative bias and reduced for positive bias. Further out, a similar sequential relationship as seen in Figure 4.26 exists, though the transition is not so clean for positive bias as it was at high pitch. It is seen that 20 V lags somewhat behind 10 V

It should be noted that the sequential reduction in bias at radii just outside of the bias region is consistent with previously–obtained Helimak data, as discussed in [20].

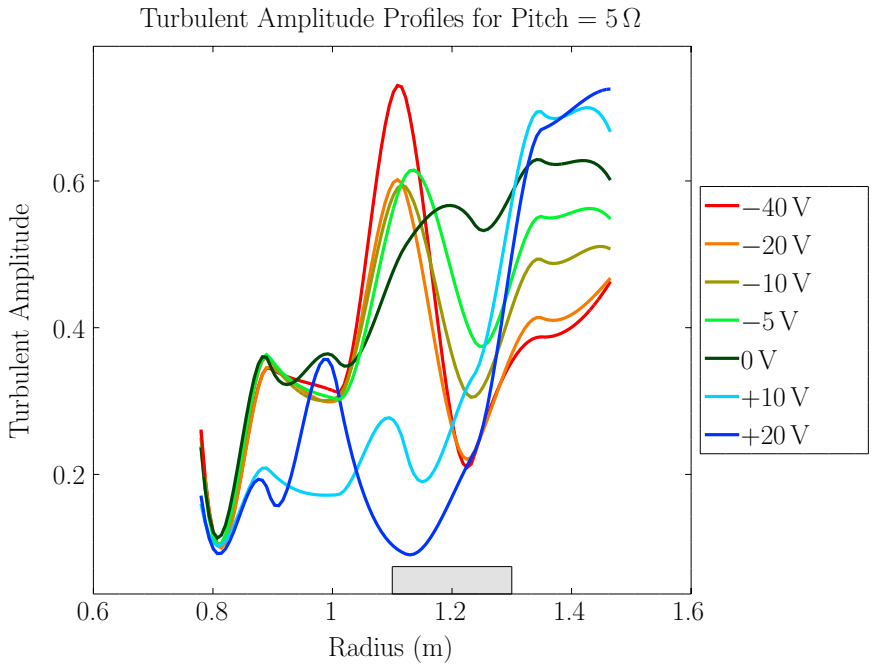

Figure 4.26: Turbulent amplitudes at a bias of 5 Ω

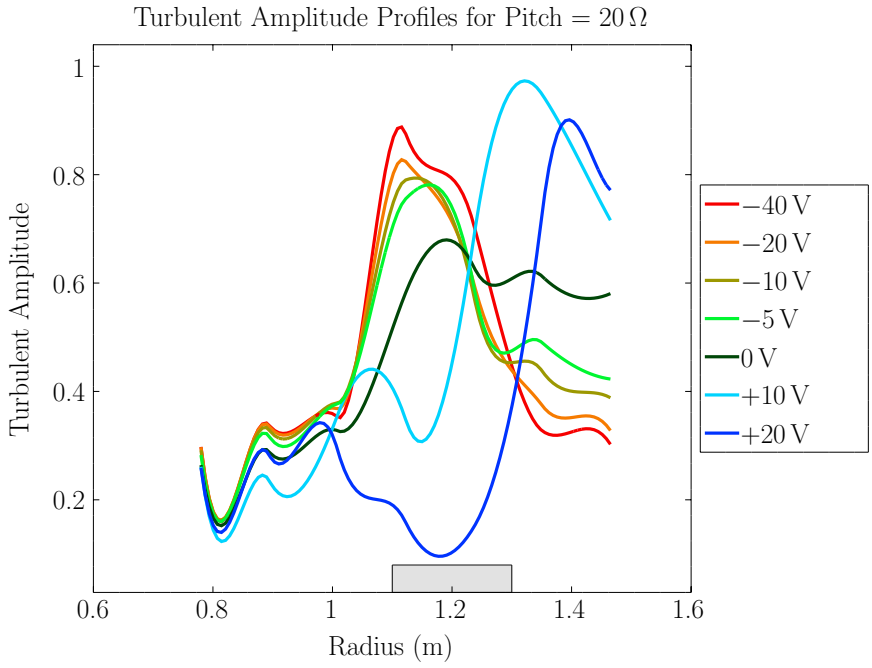

Figure 4.27: Turbulent amplitudes at a bias of 20 Ω

Chapter 5

Experimental Considerations

This chapter will describe certain experimental considerations not discussed elsewhere. Section 5.1 discusses the shielding effects that are possible at low pitch due to the vertical extend of the Langmuir probe plates. Section 5.2 discusses the method developed to ensure that the MPD and the plate probes were aligned along the same magnetic field line.

5.1 Shielding Effects

As previously noted in Section 2.1.1, the longer magnetic connection lengths in the Helimak necessarily have a much smaller pitch than the shorter ones. Hence, there has been a long–held notion that shielding is possible at the smallest pitches. Shielding can occur when the pitch is small enough that a magnetic field line striking one of the probes is blocked from the main plasma volume because it hits the back of a probe plate on its way around the machine. This is an important consideration when deciding the parameter space for Helimak experiments. While a decrease in pitch is usually associated with an increase in connection length, if shielding occurs for a certain resistance then at a certain cutoff pitch the connection length will be chopped to the distance of one half of the circumference of the device. In order to inform the decisions made in this work regarding which pitches produce reasonable data it was decided to characterize the shielding.

The distance from the main radial line of Langmuir probes to the bottom edge of the probe plates on which they are mounted is approximately 1.2 cm. Since there are two sets of plates on each of the top and bottom of the machine, the pitch must be greater that $2.4\,{}^{\mathrm{cm}}/_{\mathrm{rev}}$ (centimeters per revolution) in order for the main row of probes not to be shielded by its complementary plate set. This will assure that the magnetic field lines have a path to the opposite end of the machine.

For comparison with the experimental results, the data were compares with calculated values of the pitch. These data are based on a fit equation produced by a

magnetic field line tracing program. The equation is given by:

$$\text{Pitch} = \frac{560 B_z R^2}{B_\phi}, \tag{5.1.1}$$

where B_z and B_ϕ represent the vertical and toroidal field currents respectively, measured in amps and R is the radius of magnetic curvature in meters, yielding a value for pitch in centimeters per revolution. These theoretical values of the pitch are presented in Table 5.1.

Resistance (Ω)	Pitch (cm/rev)	Shielding Expected?
10	14.1	No
15	8.18	No
20	5.82	No
25	3.34	No
30	2.21	Yes
40	0.64	Yes

Table 5.1: Theoretical pitch and shielding at the MPD radius.

This shielding was measured by using one of the vertical lines of Langmuir probes with 1.0 cm spacing, in this case column 5 on plate U4. Unfortunately, probe U4-05 is disconnected and cannot take data, so the following probes were used: U4-04, U4-05A, U4-05B, U4-05C, U4-05D, U4-05E, and U4-05F. Data was taken at the longest connection lengths, for resistances of $R = 10\,\Omega - 50\,\Omega$. Once the data was taken, the FFTs were calculated and compared across the range of probes. While the data were taken using plate U4, the method is applicable at all radii. Since B_ϕ varies with r in the machine the pitch also varies across the radius. Theoretically then, a similar experiment could be conducted at multiple radii to illuminate the shielding effects across the entire radius. The results at a given radius will be generally applicable on both the top and bottom of the machine.

As seen in Figure 5.1, at higher pitches, such as 10 Ω the FFTs agree precisely, leading to the conclusion that no shielding is taking place. At lower pitches, such as 25 Ω, the FFTs of probes U4-04 and U4-05A agree quite well, but not the others, indicating that shielding may be occurring for probes somewhere between one and two centimeters. At 30 Ω the shielding is more pronounced, and at 35 Ω it is clear that

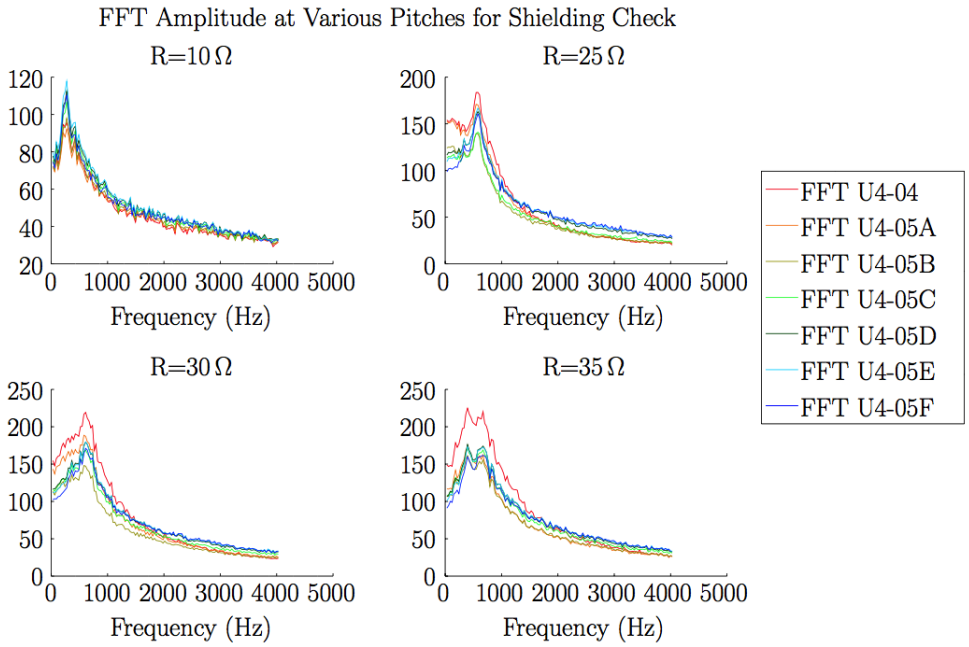

Figure 5.1: FFT amplitudes for the probes used in the shielding test

shielding is severely affecting the probes at all spacings. Hence the decision was made to only use data taken at pitches with resistances from 2.7 Ω to 25 Ω due to shielding at lower pitch. It should be noted that the experimental data from Figure 5.1 aligns exactly with the theoretical expectation from Table 5.1.

5.2 Magnetic Field Line Alignment

There are two possible approaches that can be used to find the value of $k_{\|}$ in the Helimak plasma. For one it is necessary to align a probe from the MPD on the same magnetic field line as one of the fixed plate probes. From this, the cross–phase can be measured directly and $k_{\|}$ computed by following the procedure outlined in Section 2.3.6. The other approach requires an accurate knowledge of the $k_{\perp}$ component of the wavevector and an understanding of the manner in which the measured $k_{\|}$ varies as the MPD is moved. It was decided to use the first approach in this work.

In order for this approach to work, it is necessary that the two probes be aligned nearly exactly to avoid contamination of the parallel component by the perpendicular

component. This is particularly important in this case, when $k_{\|}$ is expected to be near zero and previous Helimak experiments have made it clear that typical values of $k_{\perp}$ in the device are quite large (see Chapters 6 and 7). Hence, even a slight misalignment of the probes while making measurements of $k_{\|}$ leads to a large amount of error.

As the MPD moves only in the vertical direction, the approach is to choose the correct probes that radially match the location of the MPD, then move the MPD and determine which vertical location places the probes on the same field line. This must be done separately for each pitch.

The initial attempt at alignment, following previously completed Helimak work, was to move the MPD over a range of vertical placements and compare the cross–correlations of the ion density signals between the probes on the MPD and probes on the probe plates. At the maximum value of this cross–correlation the probes were believe to be aligned. This was compared with a calculated value of the expected location of the maximum cross–correlation based on the magnetic field profile fit, given by Eq. (5.1.1). While these calculated values were similar to the experimental values for some pitches they were different for others. Another concern with this method was the inconsistency with the cross–correlation between adjacent probes. The final concern was the lack of consistency shown by the $k_{\|}$ values as the probes were moved off of the presumed–correct field line. Some sort of reproducible relationship was expected but none was observed.

Theoretically, the failure of this method may be due to several different reasons. One is that maximizing the cross–correlation of the signals, or in other words, maximizing the similarities between the ion densities in the two signals, is functionally equivalent to maximizing the wavelength between the probes. In this sense, the maximum cross–correlation naturally finds the longest wavelength, and the smallest $k_{\|}$, present in the device. This method may also fail because it measures the direction of the group velocity, which does not follow the field lines.

The correct alignment of the probes was achieved by the implementation of a suggestion from Dr. Gentle which has been termed "electron saturation field line testing," or ESFLT. The crux of this method relies on the assumption that strongly–driven electrons will stick closely to a given field line as they curve around the vessel. By so driving electrons and measuring the cross–correlation of that signal the correct alignment can be obtained. The results are in good agreement with expectations.

As a justification of the theory the electron curvature drift can be compared with the electron transit time at the electron thermal velocity. The average electron drift in a curved magnetic field, calculated as the combination of the traditional curvature drift, $\mathbf{v}_r$, and the grad–B drift, $\mathbf{v}_{\nabla B}$ is given by [15]:

$$|\bar{\mathbf{v}}_{R+\nabla B}| = \frac{\rho_e}{R_c} v_{e,th}, \tag{5.2.1}$$

where ρ_e is the electron Larmor radius, R_c is the radius of magnetic curvature, and $v_{e,th}$ is the electron thermal velocity. Using typical Helimak parameters, this value comes to 101 m/s. The electron thermal velocity, meanwhile, is 1.33×10^6 m/s. This means that electrons will cover the distance between the plate probe and the MPD, 2.47 m, in approximately 1.86 μs, during which time the maximum drift due to curvature will be 0.188 mm. This is more than an order of magnitude smaller than the size of the probes used to collect the electrons. Hence, over the required distance the electrons will follow the field lines nearly exactly.

The procedure for implementing ESFLT is as follows. In normal Langmuir probe operation the bias supplied to the probes may be swept in order to determine the equilibrium density, electron temperature, and floating potential profiles (see Chapter 4.1). This swept voltage is predominantly negative in order to sample the ion saturation region of the probe curve. The electron saturation region cannot be reached, even for high positive bias values. However, for ESFLT the plate probes are swept to high positive bias values in order to create a "slosh" of electrons moving back and forth along the field line. These electrons, with their small Langmuir orbits, are able to follow the field line very closely. Hence, by maximizing the cross–correlation of the voltage signals between the wall probes and the MPD it is possible to align the probes accurately enough in order to make $k_\parallel$ measurements. A sample of the profiles produced is seen in Figure 5.2. Here, z is measured by inspection with a two meter stick that has been mounted next to the MPD on top of the Helimak.

For reference, the z values that correctly align the MPD for each pitch used are shown in Table 5.2

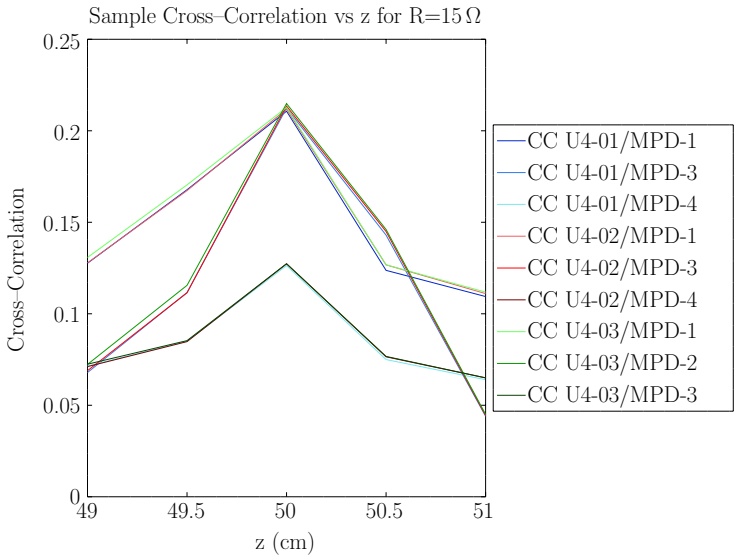

Figure 5.2: Sample cross–correlation maximization plot for R=15 Ω

Pitch (Ω)	z (cm)	Pitch (Ω)	z (cm)
25	48.5	20	49
15	50	10	51
5	55	3.6	57.5
3.3	58	2.7	60

Table 5.2: Values of z for the MPD which maximize the cross-correlation at each pitch.

Chapter 6

Grounded Results and Analysis

This chapter presents the major results of this dissertation for the case when the applied bias plates are grounded. While the data presented are interesting in their own right, they also provide a standard of comparison for the data in the biased cases found in Chapter 7. The analysis of the data is broken up into four sections. Section 6.1 analyzes the $k_{\|}$ measurements while Section 6.2 analyzes the $k_{\perp}$ measurements. Section 6.3 analyzes the power spectra and Section 6.4 discusses the bicoherence measurements and possible three–wave interactions.

6.1 Parallel Wavenumber

In the grounded case the $k_{\|}$ values for each of the non–shielded pitches are shown in Table 6.1 and Figures 6.1 and 6.2.

	Pressure (μT)			
R (Ω)	10	20	30	40
2.7	-0.0117	0.0141	0.0209	0.0115
3.3	-0.000677	0.0168	0.0171	0.0196
3.6	0.0249	0.0366	0.0284	0.0363
5	0.00372	-0.0251	-0.0250	-0.0151
10	-0.00895	-0.0347	-0.0403	-0.0226
15	0.0714	0.0991	0.114	0.143
20	0.0852	0.0847	0.0776	0.0479
25	0.0764	0.0572	0.0807	0.0660

Table 6.1: $k_{\|}$ values (m^{-1}) for all pitches and pressures

The data pattern is quite consistent between 10, 20, and 30 μT, while the pattern is slightly different at 40 μT. Hence, Figure 6.1 at 20μT is representative of all three of the lower pressures. For all pressures, there are two easily distinguished groupings of points. The values of the wavenumber at the lower resistances, 2.7, 3.3, 3.6, 5, and 10 Ω cluster around $k_{\|} = 0$. Within the range of the error bars, most of the points in this range equal zero, though an exception is noted at a pitch of 3.6 Ω in Figure 6.1. For the lower pitches at 15, 20, and 25 Ω, the values of $k_{\|}$ are clearly

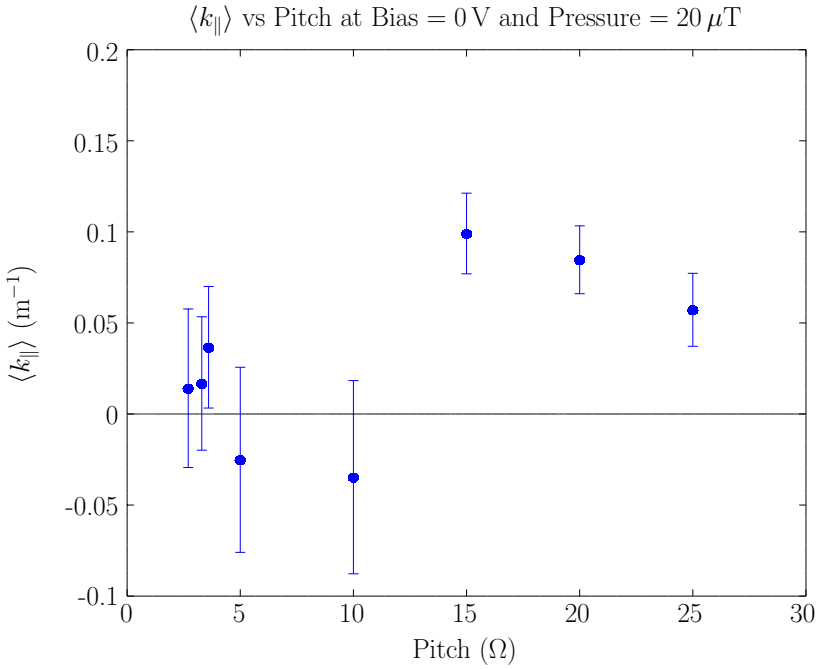

Figure 6.1: $k_\parallel$ versus pitch at a pressure of 20 μT

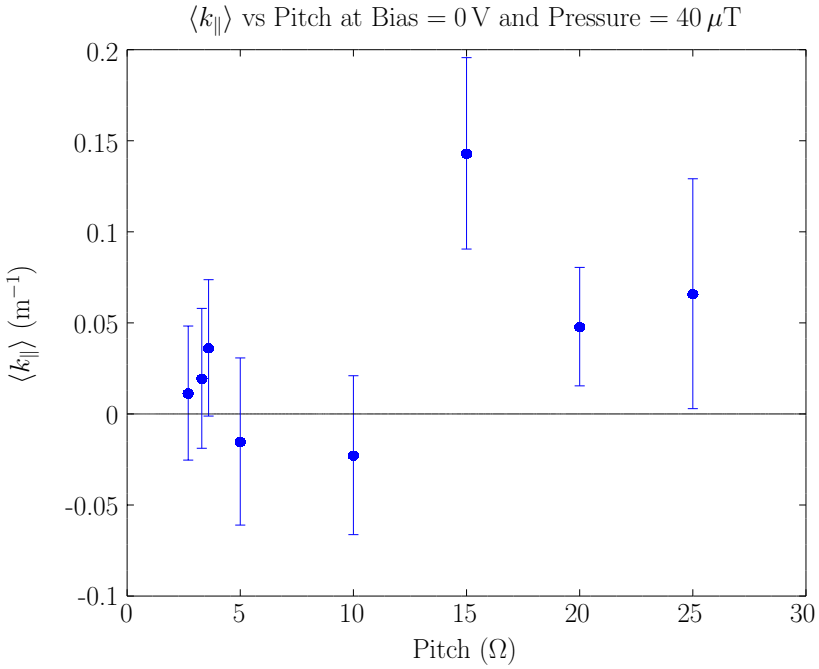

Figure 6.2: $k_\parallel$ versus pitch at a pressure of 40 μT

non–zero at pressures other than $40\,\mu$T. At $40\,\mu$T and a pitch of $25\,\Omega$, zero nearly sneaks into the range of the rather large error bars. Given the behavior of the plots at other pressures and the theory, as described in Section 3.3, it is likely that this is experimental error. However, this conclusion cannot be definitively drawn.

Hence, based strictly on the experimental measurement of $k_\parallel$ in the Helimak, it appears that a $k_\parallel = 0$ mode, which must be associated with the ideal interchange instability, dominates in the plasma for sufficiently high pitch. At lower values of pitch there is a transition to a different regime in which a mode with $k_\parallel \neq 0$, likely a drift wave, dominates.

As a further validation it is worthwhile to consider that while in ideal interchange turbulence the values of $k_\parallel$ must be identically zero this is unlikely in practice due to the limitations of finite machine size. The only way for $k_\parallel$ to actually equal zero is if $\lambda_\parallel$ goes to infinity. Given that this is impossible in a practical device one cannot actually expect to measure $k_\parallel$ values of zero.

The parallel size of the Helimak, as seen by the plasma, is variable and depends on the magnetic connection length. Naively, on may think that typical boundary conditions hold at the end plates that would hold the density constant there. However, when the plasma enters the sheath the boundary conditions are not well understood. While it is known that the Bohm sheath condition does not apply in the Helimak, it is not clear what a suitable replacement description would be. This provides an interesting light under which to consider the parallel wavelengths seen in the device.

Given that the connection length varies with the pitch of the field lines, one can consider the size of the parallel wavelengths with respect to the connection length with each pitch. These values, given as $L_c/\lambda_\parallel$ are given in Table 6.2.

R (Ω)	$L_c/\lambda_\parallel$	R (Ω)	$L_c/\lambda_\parallel$
2.7	0.0567	10	0.468
3.3	0.0800	15	2.30
3.6	0.186	20	2.77
5	0.167	25	3.26

Table 6.2: Connection length as a fraction of parallel wavelength for all pitches

Clearly, the naive assumption that a fixed number of half–wavelengths fit inside the vessel must be relaxed. For $5\,\Omega$, for example, $\lambda = {}^{2\pi}/_{k_\parallel} = 249\,\text{m}$, while the magnetic connection length is 41.7 m, meaning that only about 17% of one wavelength

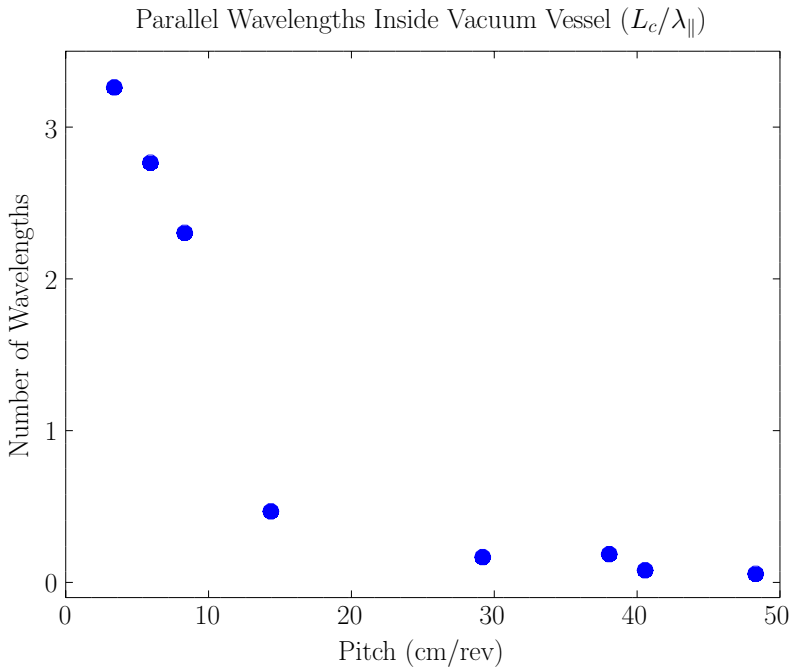

Figure 6.3: Minimum theoretical value of $k_\parallel$ versus pitch

is contained in the vacuum vessel. For the higher pitches this percentage ranges from 6% at 2.7 Ω to 47% at 10 Ω. At the lower pitches, however, this percentage averages out to about 280%, meaning that almost three complete wavelengths fit inside of the vacuum vessel, further confirming the previously stated results.

The number of wavelengths that fit onto with the magnetic connection length is plotted versus pitch, this time as centimeters per revolution, in Figure 6.3. Here again, as in Figure 6.1 above, it is clear that there are two regimes. At high pitch only a fraction of one wavelength fits inside of the vacuum vessel. This is both an interesting observation about the boundary conditions and also further evidence that the Helimak, while a finite–sized device, generates instabilities that are the physical equivalent of the theoretical, global, interchange instability. At low pitch, a more localized, though still large, instability dominates. This instability fits about two to three of its wavelengths inside of the vacuum vessel.

It can thus be concluded that the ideal interchange mode, or its close cousin, dominates in the Helimak plasma at high pitch with R=2.7, 3.3, 3.6, 5, and 10 Ω. Based on the experimental data alone there are several candidate modes that could

dominate at the lower pitches with R=15, 20, and 25 Ω. However, the theory predicts that several of these modes are not relevant for Helimak plasmas, leaving one to conclude that drift waves dominate at those pitches (see Section 3.3 for a discussion of the relevant theory).

6.2 Perpendicular Wavenumber

As described in Section 3.3, a knowledge of $\langle k_\perp \rangle$ is useful in analyzing instabilities. While the interchange instability has no constraints on $k_\perp$ the growth of drift waves depends strongly on it. The maximum theoretical growth rate of drift waves occurs at $k_\perp \rho_s \approx 1.26$. Given $\rho_s = 2.05\,\mathrm{cm}$ we find that the growth rate is maximum for $k_\perp \approx 61\,\mathrm{m}^{-1}$. In Figure 6.4 we note that, at $20\,\mu\mathrm{T}$, $k_\perp$ at the outer radii of the machine, such as near the location of the MPD, is approximately $30 - 40\,\mathrm{m}^{-1}$. While not shown, this value varies between 30 and $60\,\mathrm{m}^{-1}$across all pressure values. At radii further in, Figure 6.5 shows that the value of $k_\perp$ is less consistent, varying between 20 and $60\,\mathrm{m}^{-1}$, covering regions both where drift waves may be expected to be stronger and regions where they may be expected to be weaker.

These values of $\langle k_\perp \rangle$ would suggest a fairly large growth rate for drift waves, varying from $\approx 58\%$ to $\approx 99\%$ of the maximum value, as seen in Figure 3.4. Hence, a large $k_\parallel \neq 0$ component is expected for almost all pitches. However, as noted in Section 6.1, this is not the case. The relative flatness of the curves in Figure 6.4 at most resistances reveals that the change in regime is not simply related to a change in favorability for drift waves. For instance, the $k_\perp$ values at 5 Ω and 25 Ω are similar, yet it has been shown that these pitches represent two different instability regimes. Hence, the overly simply explanation that the regime shift follows a change in $k_\perp$ that increases the drift wave growth rate can be discarded as not supported by the evidence at hand. The presence of favorable $k_\perp$ for drift wave growth coupled with a lack of drift waves at high pitch suggests that the instability of the interchange mode previously identified does not allow the plasma density gradient to ever steepen to the point where drift waves can take effect. In other words, despite the favorable conditions, no drift waves arise because no drivers of drift wave instability are present.

A useful question that can be asked here is how accurate the average is as a measure of $k_\perp$. This can be addressed by observing the dispersion relations for

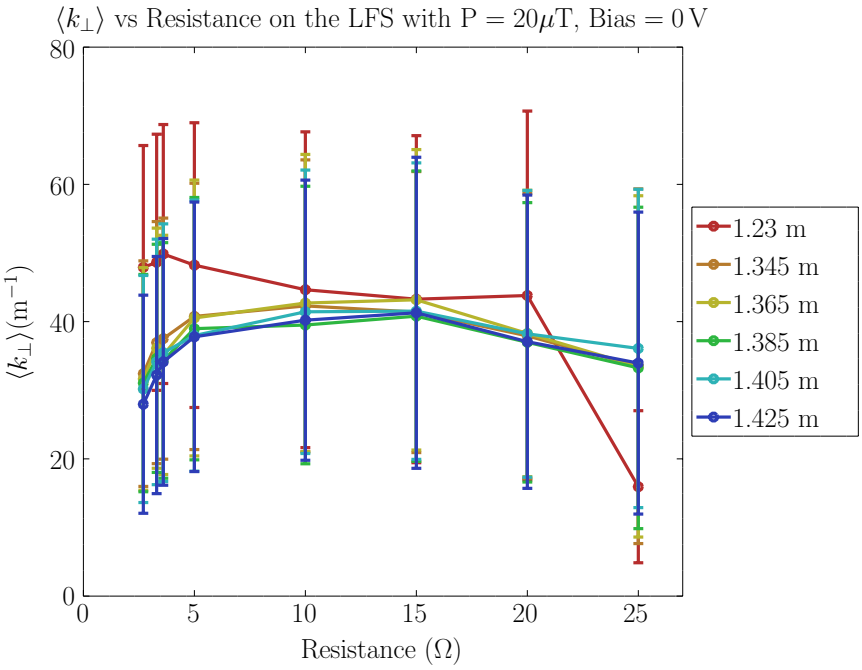

Figure 6.4: Perpendicular wavenumber vs resistance on the LFS with P=20μT

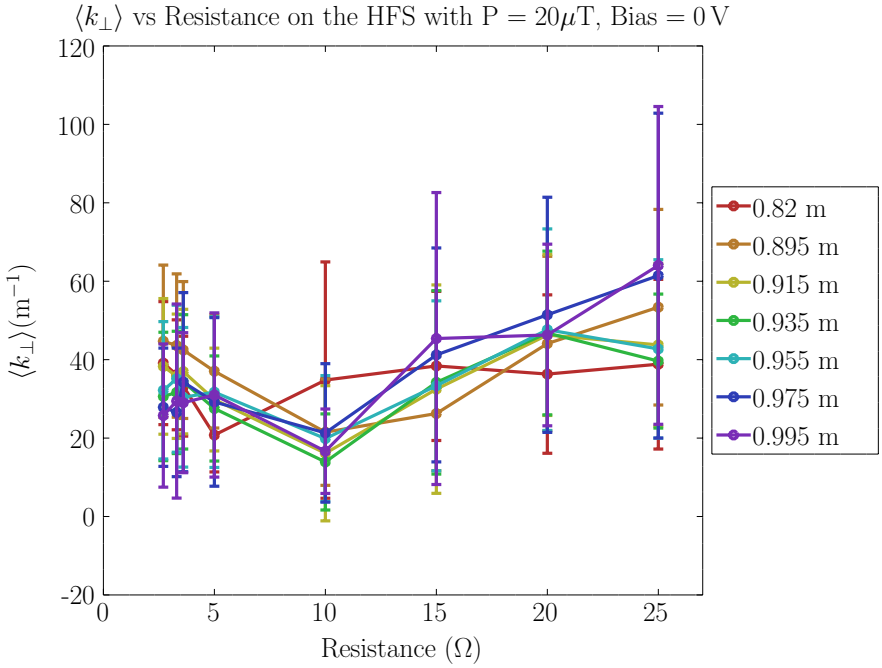

Figure 6.5: Perpendicular wavenumber vs resistance on the HFS with P=20μT

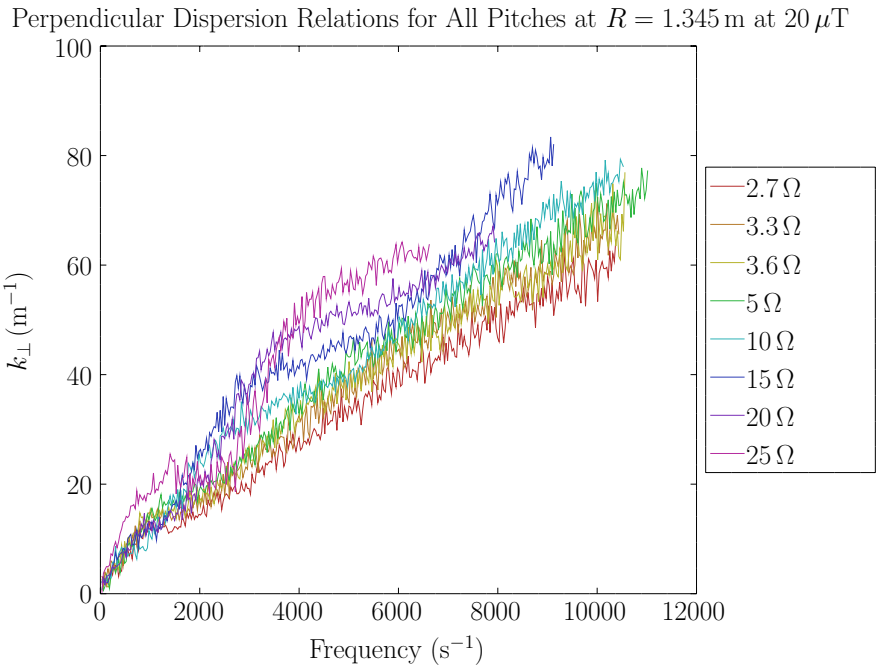

Figure 6.6: Dispersion relations for all pitches at radius of 1.345 m with no bias at a pressure of $20\,\mu\mathrm{T}$

various channels as discussed in Section 2.3.6. While the pressure plays an interesting role, in general the dispersion relationships are more linear on the LFS than on the HFS. Figure 6.6 shows the dispersion relations for all pitches at $R = 1.345\,\mathrm{m}$. The dispersion relations are all mostly linear, with the degree of linearity decreasing as the pitch is decreased. As discussed in Section 3.2, the maximum growth rate for drift waves will theoretically occur at $k_\perp \approx 61\,\mathrm{m}^{-1}$. Based on Figure 3.4, the drift wave growth rate will be greater than 75% of its maximum value in the range $k_\perp \approx 37 - 100\,\mathrm{m}^{-1}$ and greater than 50% of its maximum value from $k_\perp \approx 28 - 140\,\mathrm{m}^{-1}$. Hence, the growth rates will be large for almost all values of $k_\perp$ shown in Figure 6.6 and thus using the average, which also indicates a large growth rate, seems reasonable.

For the dispersion relations shown in Figure 6.6 the phase velocities vary between $572.3\,\frac{\mathrm{m}}{\mathrm{s}}$ at $25\,\Omega$ and $1000.8\,\frac{\mathrm{m}}{\mathrm{s}}$ at $2.7\,\Omega$.

The dispersion relations on the HFS, as shown in Figure 6.7, are not as linear as those on the LFS. They are also less consistent, with the dispersion relations near the density maximum displaying messy, extremely nonlinear behavoir. Interestingly, for the plotted radius the dispersion relations for high pitch are no longer significant

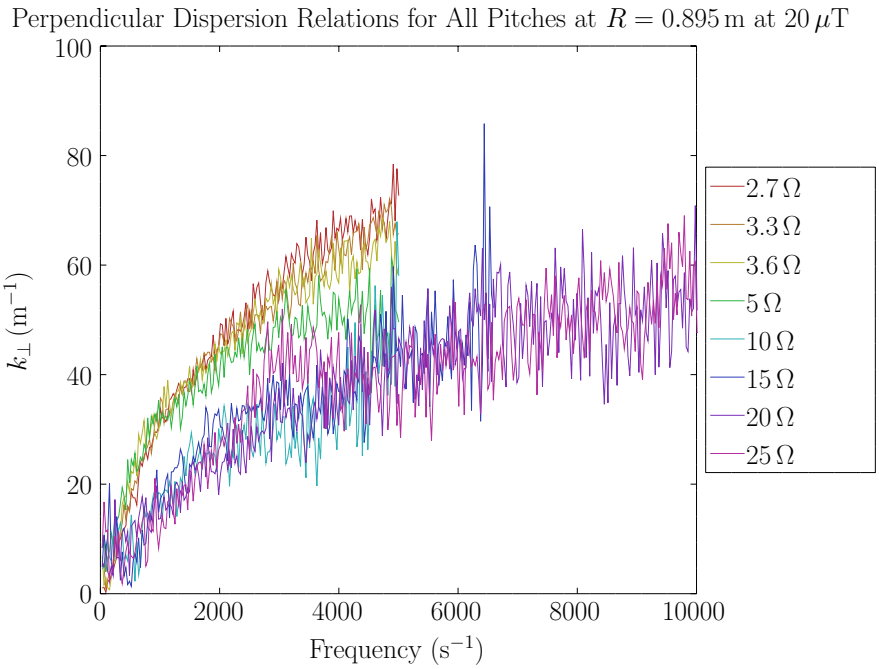

Figure 6.7: Dispersion relations for all pitches at radius of 0.895 m with no bias

past approximately $5000\,\mathrm{s}^{-1}$. As described in Section 2.3.6, this is an indication that the coherency between the two probes drops to too low a value at higher frequencies. This stands in stark comparison to Figure 6.6 in which the dispersion relations are significant until nearly $10000\,\mathrm{s}^{-1}$. For the lower pitches the trend is the opposite, with the coherency staying high until a frequency of nearly $20000\,\mathrm{s}^{-1}$ though, noticeably, the signals are much noisier than on the LFS. Insofar as linear regression can be performed for the preceding curves the phase velocities are seen to lie in the range from $362.1\,\frac{\mathrm{m}}{\mathrm{s}}$ at $2.7\,\Omega$ to $1118\,\frac{\mathrm{m}}{\mathrm{s}}$ at $25\,\Omega$.

The consistency of these results between different probes on the HFS and LFS not shown here, along with the differences as the gas feed pressure is varied, paint an interesting picture. The dispersion relations on the HFS are inconsistent, often nonlinear, and generally noisy, while those on the LFS are linear at high pitch and approximately linear at low pitch. The low pitches are more linear at lower pressure and less linear at higher pressure, as seen by comparing Figures 6.6 and 6.8, taken at a pressure of $40\,mu\mathrm{T}$. Calculating the phase velocities at this higher pressure shows that the range is lower than that at $20\,\mu\mathrm{T}$ with values falling between $319.5\,\frac{\mathrm{m}}{\mathrm{s}}$ at $25\,\Omega$

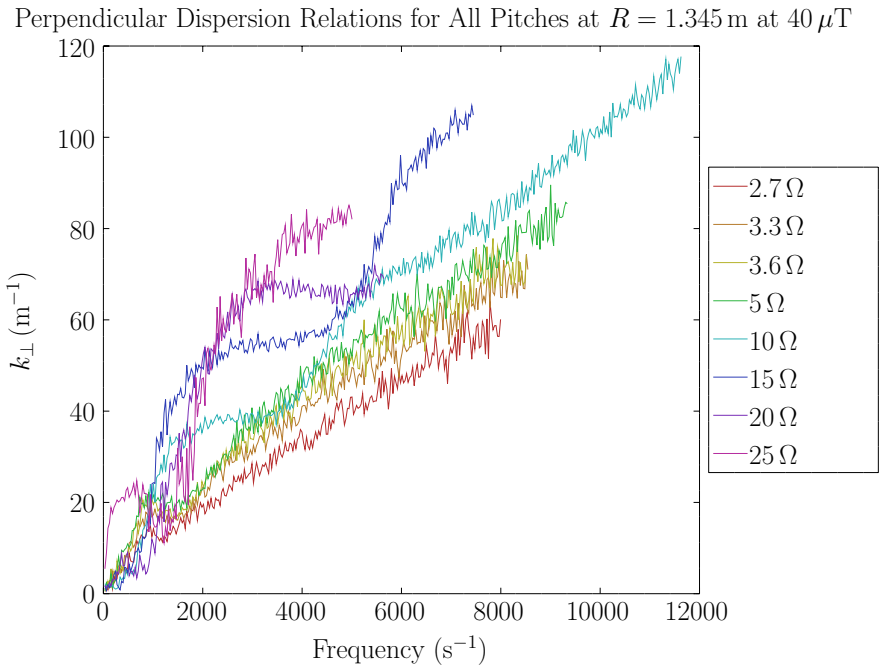

Figure 6.8: Dispersion relations for all pitches at radius of 1.345 m with no bias at a pressure of $40\,\mu\mathrm{T}$

and $793.9\,\frac{\mathrm{m}}{\mathrm{s}}$ at $2.7\,\Omega$.

While the reasons for these differences are not immediately apparent it does seem clear that $k_\perp$ on the LFS is affected by changes in pitch. While not as obvious when looking at the average values (Figure 6.4) as it is for $k_\parallel$, an examination of the dispersion relations (Figures 6.6 and 6.8) reveals differences in the nature of the instability at different pitches. Unfortunately, with the given data it is impossible to use $k_\perp$ to help specifically identify the instability. Theoretically, drift waves have short vertical wavelengths (large $k_\perp$) and interchange instabilities have longer vertical wavelengths (small $k_\perp$) [8]. However, while the nature of the dispersion relations change with pitch, the actual values of $k_\perp$ do not change significantly.

6.3 Power Spectra

As discussed in Section 2.3.3, the power spectrum is a useful tool for examining which frequencies appear in a given signal as well as their relative magnitudes. While the most interesting features of the following power spectra can be seen at all

pressures, the traces are especially enlightening at $40\,\mu$T where the features are most discernible, as seen in Figures 6.9 and 6.10.

Figure 6.9 shows the power spectra for all pitches at a radius of 0.82 m on the HFS. For the highest pitches the power spectra are relatively featureless. For lower pitches, however, there is a large peak near 1500 Hz that varies in relative amplitude while remaining stationary in frequency. However, the entire signal at these pitches is very low. Due to its location on the HFS this cannot be due to an interchange instability, which are stable in regions in which the density gradient and radius vector point in opposite directions. There is, however, the possibility of a drift wave existing on the HFS, driven unstable by the plasma resistivity or magnetic curvature. However, if this were the case it would be expected that the direction of propagation would be opposite that on the HFS. As shown in Figures 6.6 and 6.7 this is not the case, leaving one to conclude that this is the result of turbulence broadening from the LFS.

On the other hand, Figure 6.10 shows significantly different results. This data is from a probe at a radius of 1.305 m, close to the location of the MPD, on the LFS. Here, the power spectra for the lowest pitches are relatively featureless, being dominated by a low frequency peak. As the pitch is raised, however, features begin to appear. At $15\,\Omega$ a bump appears at $f \approx 3000$ Hz. As the pitch continues to increase this bump grows in relative magnitude while also decreasing in frequency until it comes to dominate the spectrum at $3.6\,\Omega$ and $f \approx 1000$ Hz. Its spectral width also decreases from nearly 2000 Hz to about 600 Hz. Figure 6.11 shows the same set of probes at $20\,\mu$T for comparison. While the same bump is seen to appear at $15\,\Omega$ its movement inward and rise in power are far less distinctive. Instead of appearing as a larger peak at $5\,\Omega$ it appears as small bump on the side of the main peak. Eventually, however, it does come to dominate the spectrum, again at $f \approx 1000$ Hz

Clearly, and reasonably, the plasma behaves differently on the HFS and LFS of the machine. The HFS is dominated, when it has any features at all, by a single frequency, essentially locked in place at the lowest pitches. Hence, the instability present here does not have a frequency that depends on magnetic connection length once it is established or, equivalently, on the spacing between magnetic field lines. Interestingly, the peak is most dominant where the spacing between field lines is small, suggesting that this peak may be related to cross–field movement of plasma. The

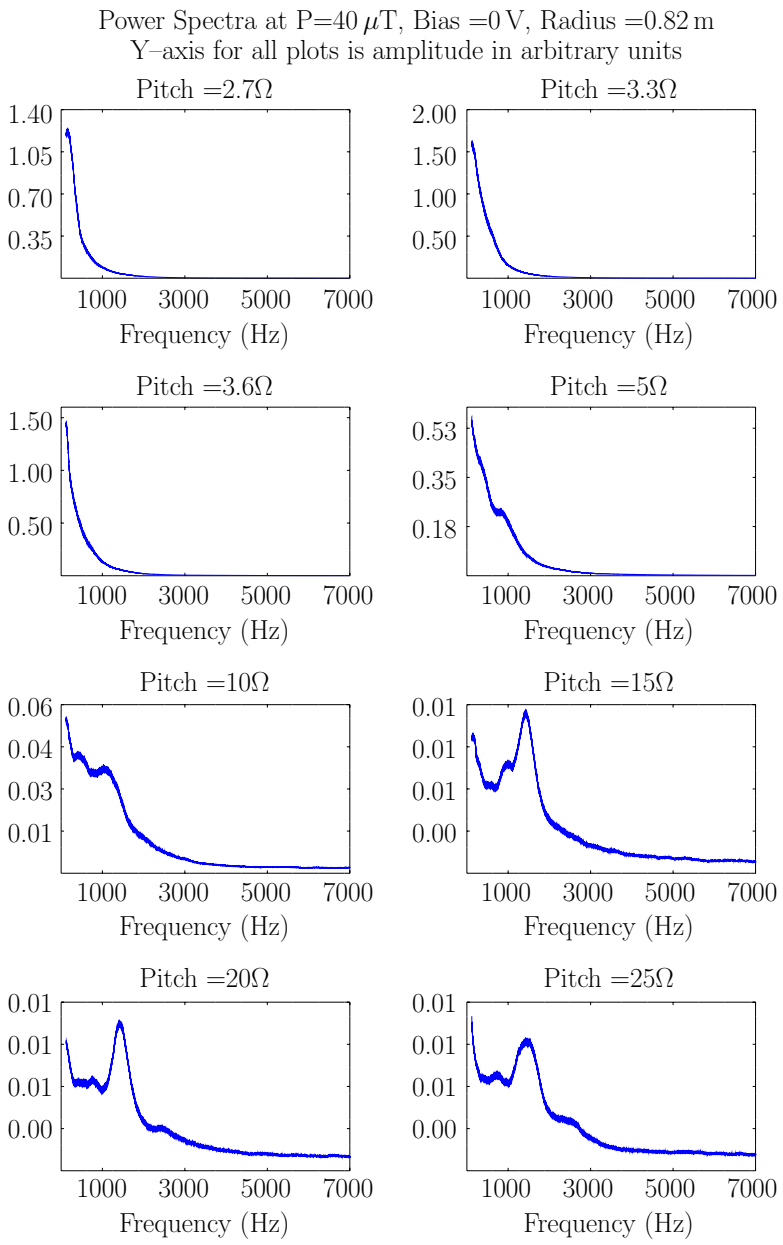

Figure 6.9: Power spectra for all pitches at radius of 0.82 m and P = 40 μT

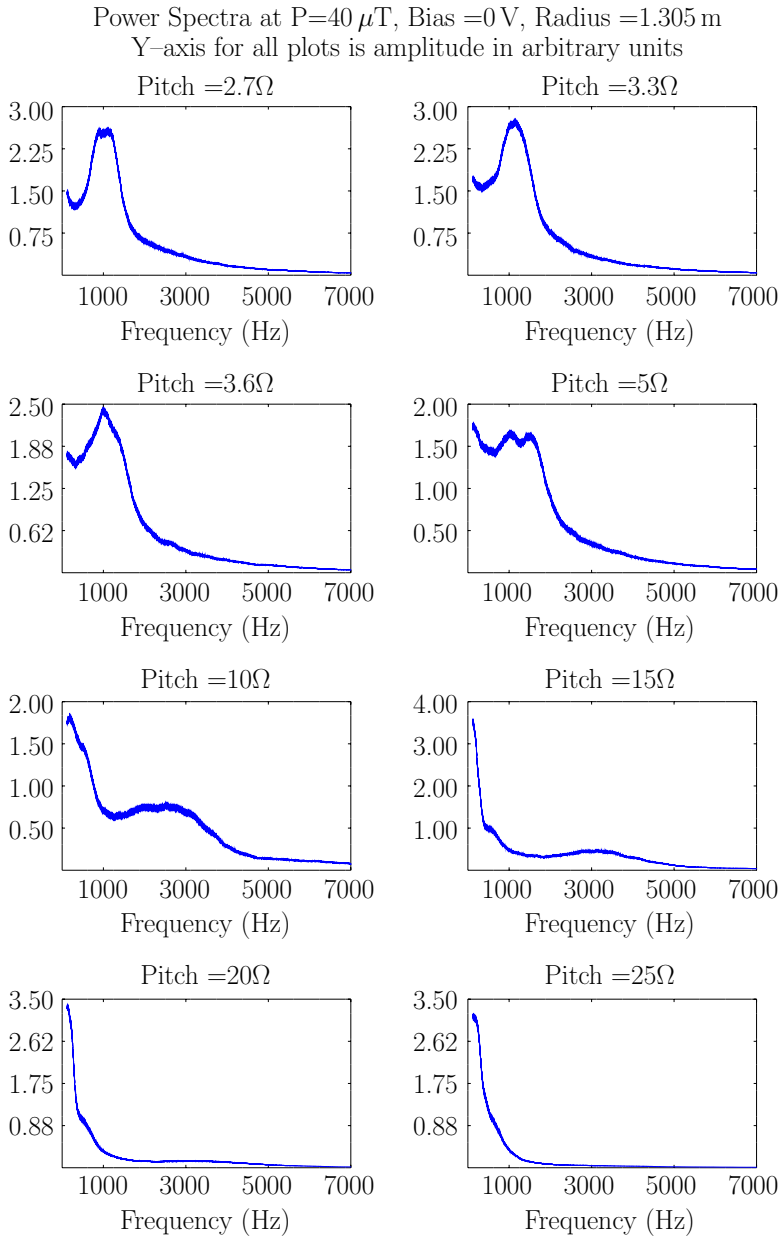

Figure 6.10: Power spectra for all pitches at radius of 1.305 m and P = 40 μT

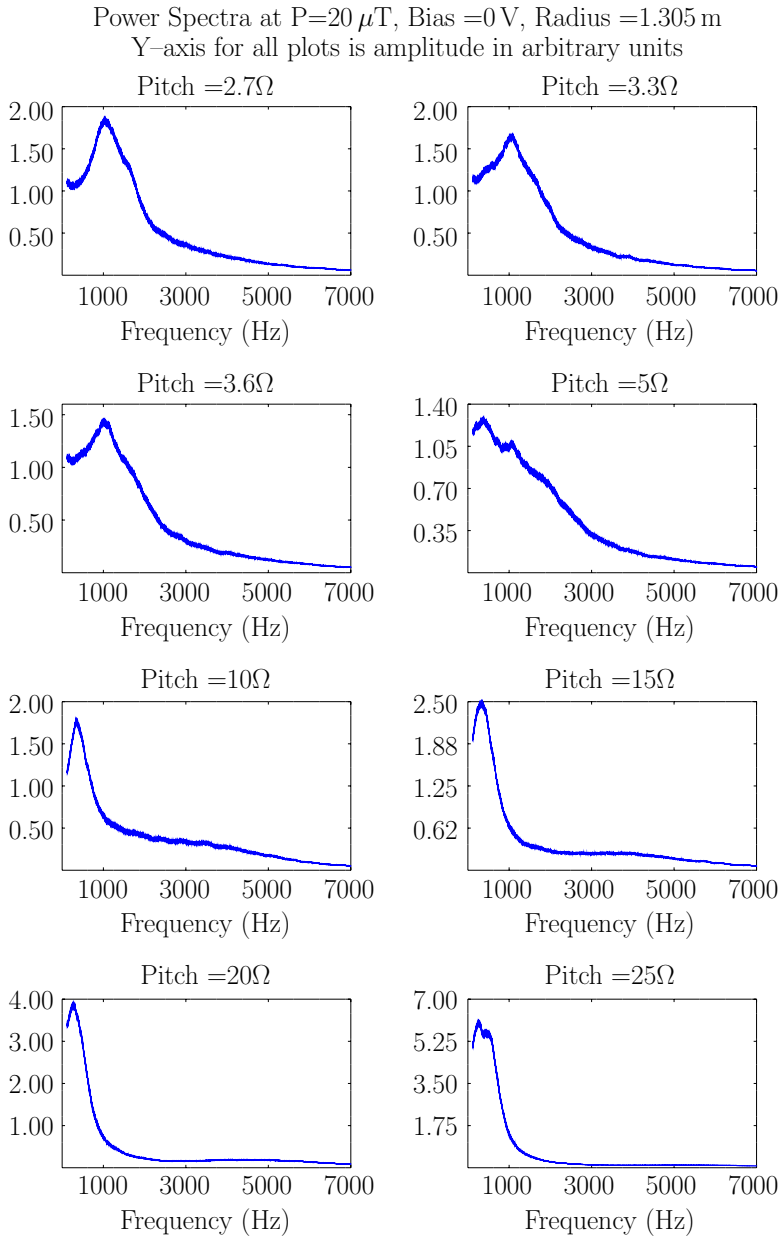

Figure 6.11: Power spectra for all pitches at radius of 1.305 m and P = 20 μT

moving peak on the LFS, conversely, is most dominant at larger field line spacing, where cross–field transport should be more limited, and hence may represent a mode that is disrupted by such transport. The movement of the peak frequency also indicates that said frequency is correlated with the magnetic connection length, or else of some parameter associated with it.

Given the results of Sections 6.1 and 6.2 it is seems reasonable to identify the stationary mode on the LFS as a drift wave and the mode in motion as an interchange instability that dominates at high pitch. The interchange instability is itself a zero–frequency mode. Hence, any measured frequency that can be associated with it must necessary be that of a bulk plasma motion which would create a measurable non–zero frequency in the laboratory frame while allowing the interchange mode to maintain zero frequency in the plasma frame. Such bulk velocity measurements have been taken on the Helimak over a more limited parameter space and more limited radial extent than that depicted here. While not yet definitive, the preliminary results are encouraging that, in general, higher pitches tend toward lower bulk flow velocities in the grounded case [18]. Measured over the same distance, lower velocities imply that there is a lower bulk frequency for higher pitches, in good agreement with Figures 6.10 and 6.11. Hence, spectroscopic measurements further support the identification of the growing instability on the LFS with an interchange mode moving along with the bulk plasma.

In a 2008 paper, Poli et. al. found a similar result on both the HFS and LFS of TORPEX, a Helimak–like device with similar magnetic geometry and a significantly smaller plasma volume [16]. They identified the stationary peak on the HFS as a drift wave and the moving peak on the LFS as an interchange instability.

6.4 Bicoherence

As discussed in Section 2.3.7, the bicoherence can be a useful means of examining nonlinear interactions in the plasma. For the strongest coupling seen in the following figures, the bicoherence (a normalized measure that can take on values from 0 to 1) has a maximum between 0.25 and 0.35. Hence, while not exceptionally strong, there is evidence of some weak three–wave nonlinear coupling in the Helimak plasma. For the grounded case there are significant differences as the gas feed pressure, and

hence the collisionality, is increased. There are also major differences, as expected, at different field line pitches. All of the bicoherence plots are reported for probe U4-02. Though not exactly the same probe, this probe is close to those used for the power spectra and hence the bicoherence plots can be usefully compared with the power spectra on the LFS in Section 6.3

At the highest pitches and low collisionality, the interactions are mostly focused near the origin, as shown in Figure 6.12, at $20\,\mu$T. Only low frequencies interact with each other, as would be expected for an interchange instability in the plasma frame. As the pitch is lowered a transition takes places whereby the interactions spread to higher frequency. At the lowest pitches, such as at $25\,\Omega$ as shown in Figure 6.13, the coupling is far more prevalent. Here, waves at all frequencies are tied to the low frequency wave at $\approx 500\,$Hz. It is interesting to note that the higher bicoherence at frequencies of less than 500 Hz is present in both figures. However, at low pitch that high level of coupling has extended to a much larger range. Hence, the three wave coupling is present over a much wider frequency range at lower pitch.

These plots can be compared with the power spectra in Figure 6.11. At $25\,\Omega$ the peak near 500 Hz is present in both figures. The other frequencies present, however, carry little power and are therefore only nominally interesting. It is possible, based on Figure 6.13, that the power spectrum is so low because the power is being transferred to the lower frequencies. The opposite holds true at $5\,\Omega$ where the peak is broad at low frequency but only a few frequencies around zero show any signs of coupling in Figure 6.12.

At higher collisionality, however, the relationships are quite different. As seen in Figure 6.14, at $40\,\mu$T and high pitch the zero interaction are still present, but complimented by interactions at higher frequencies. In particular, frequencies above 1.5 kHz shown a strong relationship with the frequency at 1.5 kHz that drops off fairly slowly toward higher frequency. As this is a three–wave interaction, the coupling of two waves of 1.5 kHz should lead to a rise in energy of the 3 kHz wave, which is where the bump seen in the power spectrum arises at lower pitch. Hence, it is possible that the wave is being generated at higher frequency then shifting in frequency by different amounts at different pitches. The relationships at lower pitch are also different than at $20\,\mu$T as shown in Figure 6.15. Here, the relationships with 500 Hz no longer exist and have been replaced with relationships between the highest, $4-5\,$kHz and lowest,

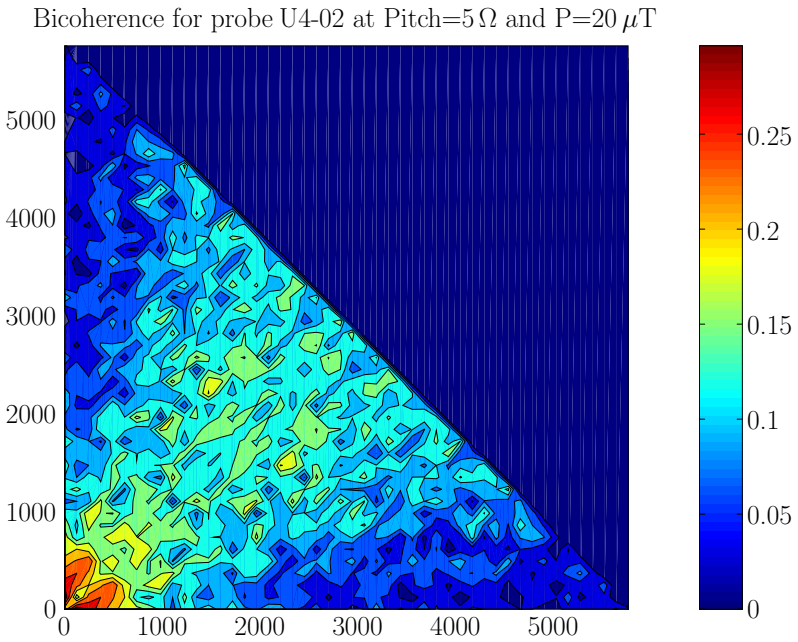

Figure 6.12: Bicoherence for a pitch of 5 Ω at 20 μT in the grounded case.

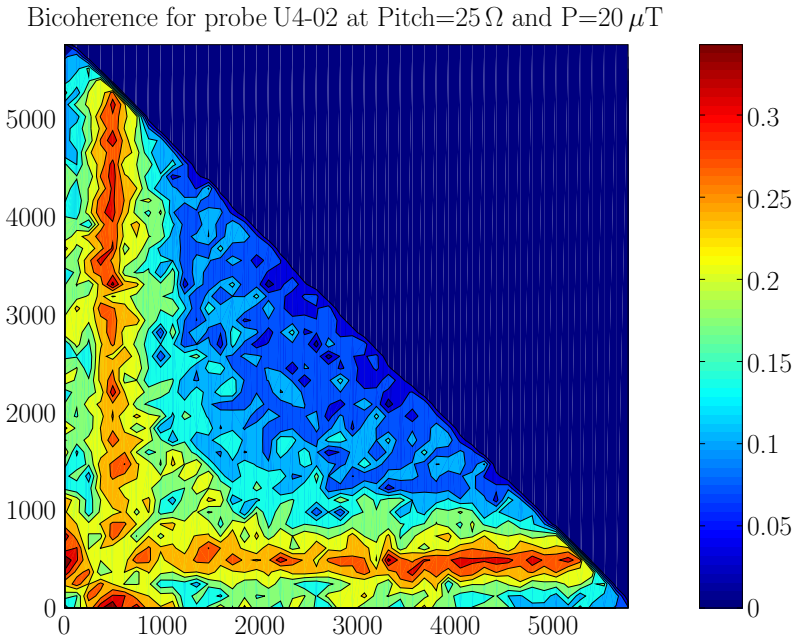

Figure 6.13: Bicoherence for a pitch of 25 Ω at 20 μT in the grounded case.

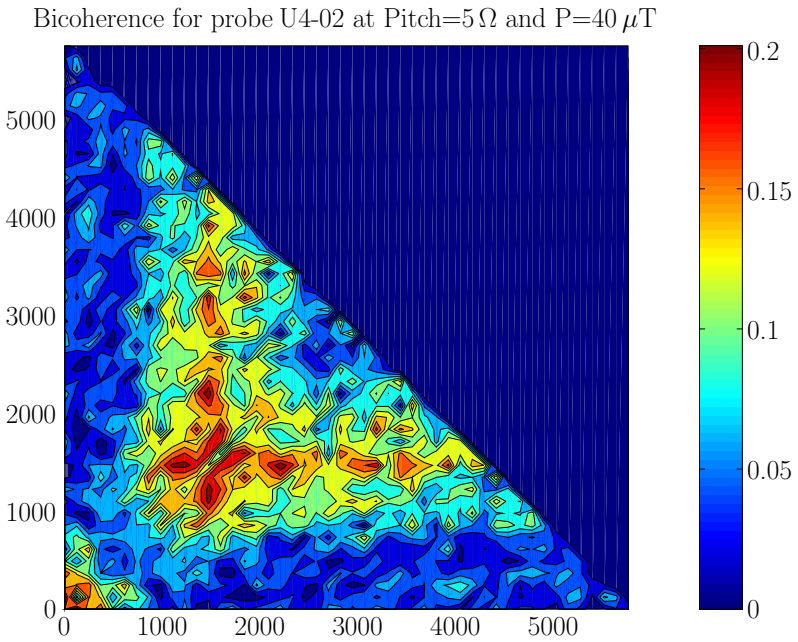

Figure 6.14: Bicoherence for a pitch of 5 Ω at 40 μT in the grounded case.

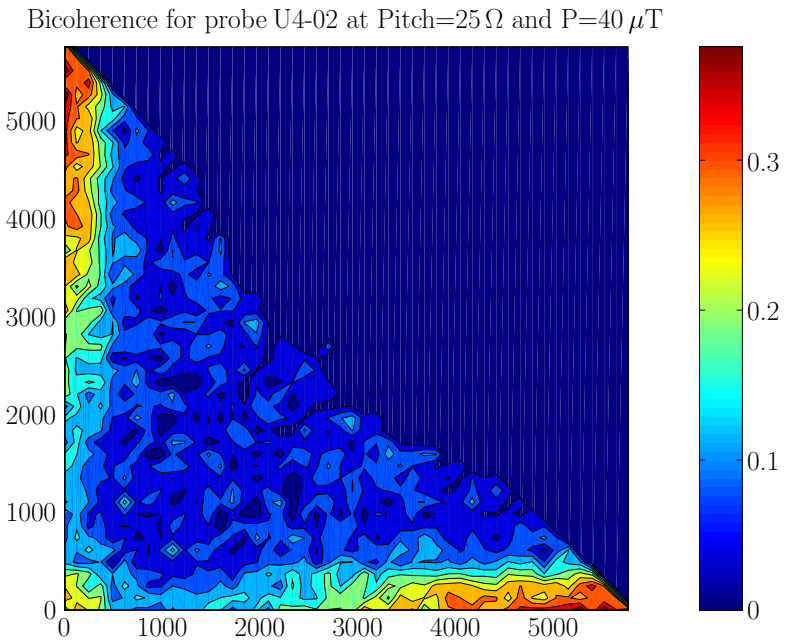

Figure 6.15: Bicoherence for a pitch of 25 Ω at 40 μT in the grounded case.

0 Hz, frequencies plotted.

The data points at $40\,\mu$T can be compared with the power spectra in Figure 6.10. As seen in that figure at $5\,\Omega$, there are two low peaks near 1.0 and 1.5 kHz. This peak near 1.5 kHz lines up well with the maximum seen in the bicoherence (Figure 6.14). While the power spectrum drops off quickly beyond that point, the bicoherence tells us that the tail is correlated with the decreasing power at those frequencies. For the power spectrum at $25\,\Omega$ there is little power in the $4-5$ kHz range that shows up in the bicoherence in Figure 6.15, though the peak at zero frequency is well–represented, just as the peak at 500 Hz is for lower pressure. Hence, while these interactions may be coupled, they appear to be relatively uninteresting due to their lack of power.

Chapter 7

Bias Results and Analysis

This chapter builds on those results presented in the previous chapter by applying bias to a subset of the bias plates, as explained in Section 4.2.2. The characteristics of the instabilities are strongly affected by the presence of both positive and negative bias. The analysis of this chapter is broken into the same four sections as that of the previous. Namely, Section 7.1 analyzes the $k_{\parallel}$ measurements, Section 7.2 analyzes the $k_{\perp}$ measurements, Section 7.3 analyzes the power spectra, and Section 7.4 discusses the bicoherence measurements.

7.1 Parallel Wavenumber

The simple relationship between $k_{\parallel}$ and pitch that was identified for the grounded case in Section 6.1 no longer holds when negative bias is applied. At $20\,\mu$T, the application of $-5\,$V of bias produces the changes seen in Figure 7.1.

The general shape of the figure at low magnitudes of negative bias is quite similar to that for the grounded case, Figure 6.1. However, the four highest pitches have moved towards more negative values by an average shift of $0.078\,\mathrm{m}^{-1}$. At higher pitch the values have remained reasonably constant, except for 25Ω which now shows $k_{\parallel} = 0.015\,\mathrm{m}^{-1}$, which places it within the range of error of being equal to zero.

As the bias voltage is lowered further all of the calculated $k_{\parallel}$ values move toward the negative, nearing a saturation point as the bias approaches $-20\,$V. These data are shown in Figure 7.2. As seen in the figures, the higher–pitched values move a slightly larger distance than the lower–pitched ones. The $k_{\parallel}$ of four highest pitches have shifted by an average of $-0.234\,\mathrm{m}^{-1}$, or by 1000% of their grounded values. Meanwhile the $k_{\parallel}$ of the three lowest pitches have shifted by only $-0.166\,\mathrm{m}^{-1}$, approximately two–thirds of the high pitch change, or by 200% of their grounded values. Clearly the application of negative bias affects the higher–pitched values, previously shown to be an interchange instability, more than it affects the lower–pitched, drift wave values. Some possible reasons for this will be discussed below.

At the highest magnitude negative biases, the $k_{\parallel}$ value of the three highest pitches saturate eventually at $k_{\parallel} \approx -0.27\,\mathrm{m}^{-1}$. This value is clearly non–zero, in-

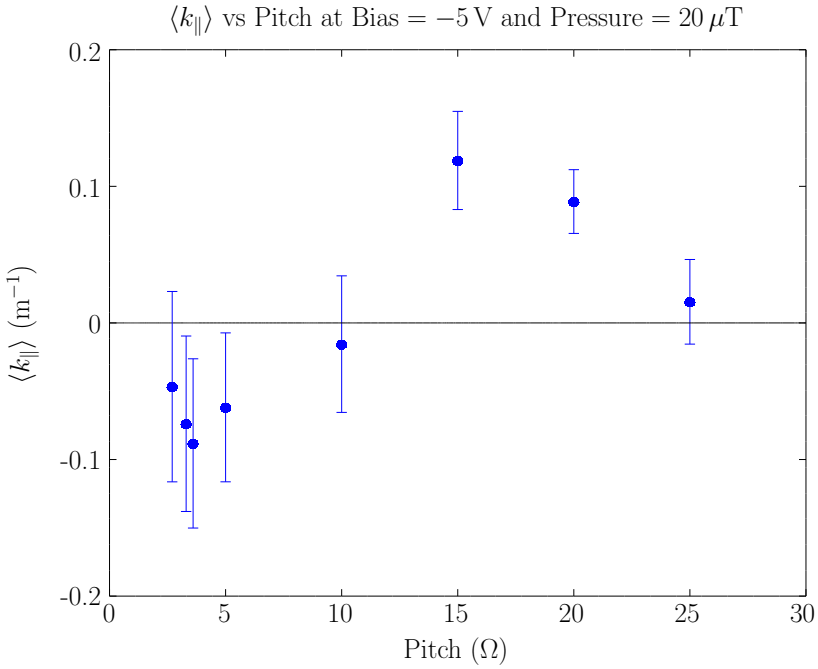

Figure 7.1: Parallel wavenumber with −5 V of applied bias

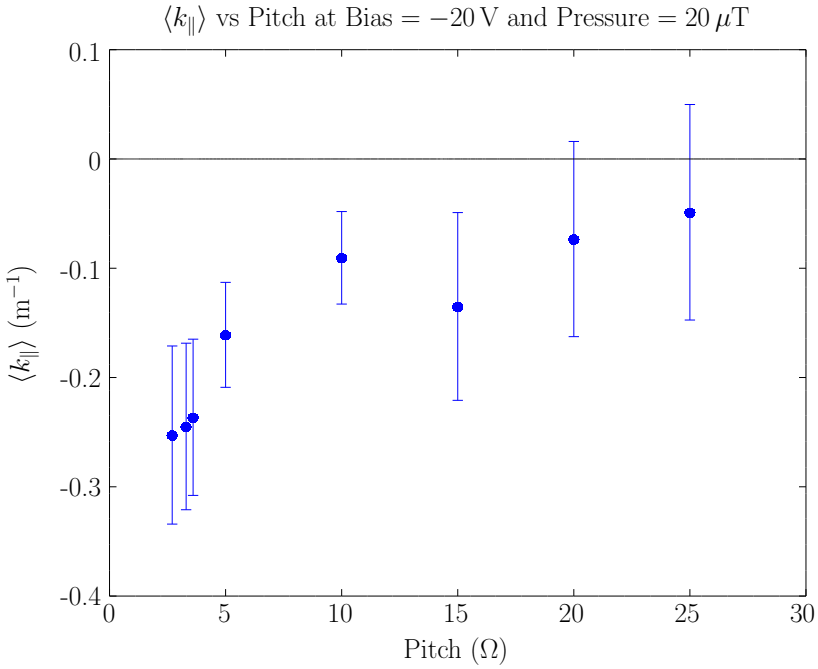

Figure 7.2: Parallel wavenumber with −20 V of applied bias

dicating a complete shift in the nature of the instabilities with the application of negative bias. The shape of the wavenumber "curve" has also changed, with the values taking on a nearly linear relationship. Interestingly, the $k_{\|}$ values at the lowest pitches, 20 and 25 Ω are now within range of equaling zero themselves.

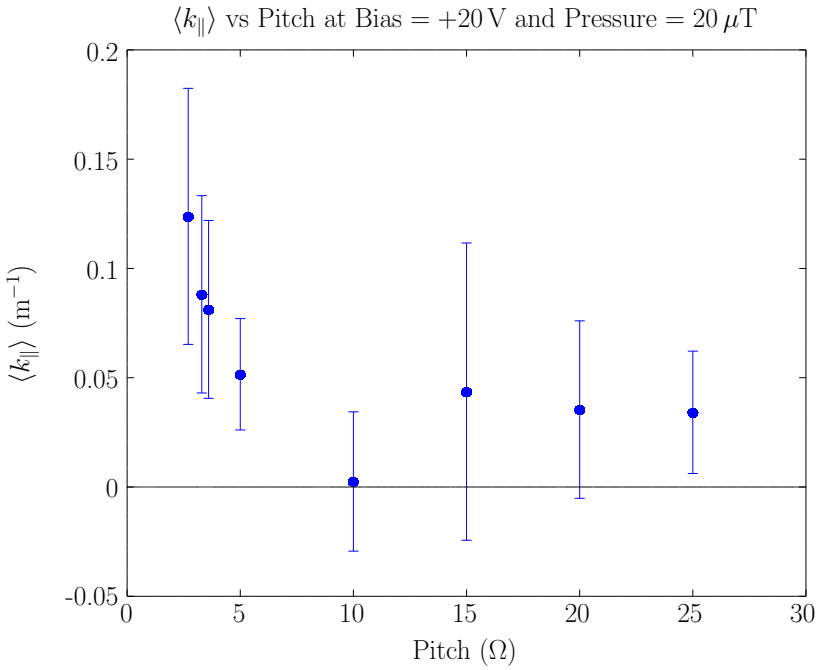

Figure 7.3: Parallel wavenumber with +20 V of applied bias

For positive applied bias the opposite effect occurs at high pitch (again, compare with Figure 6.1). As shown in Figure 7.3, for a bias of +20 V there is an overall shift of the high–pitched $k_{\|}$ values in the positive direction. The lower pitches have all moved slightly towards zero, as in the case of negative bias. They again fall in the range of equaling zero themselves. The shifts are not so great as for the negative case. Here, the magnitudes of $k_{\|}$ for the five highest pitches have shifted by an average of 0.068 m^{-1}, or by 267% of their grounded values while the $k_{\|}$ of the three lowest pitches have shifted by -0.043 m^{-1}, again approximately two–thirds of the high pitch change, or by 53.0% of their grounded values. The shift at low pitches is in the same direction but of smaller magnitude than that for negative bias while the shift at high pitches is of much smaller magnitude in the opposite direction. As in the negative case, $k_{\|}$ at the highest three pitches is very clearly non–zero, with an

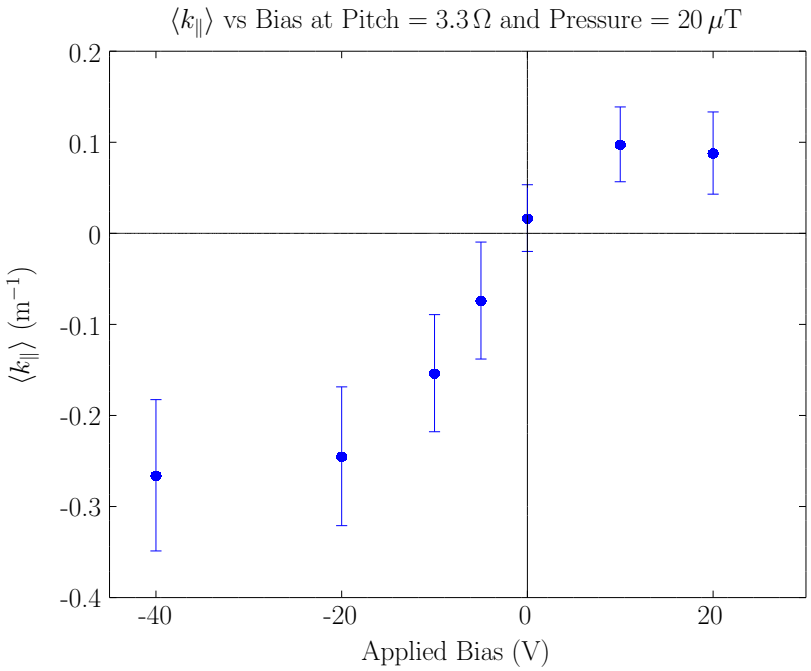

Figure 7.4: Parallel wavenumber at a pitch of 3.3 Ω versus bias

average at $k_\parallel \approx 0.0978\,\mathrm{m}^{-1}$.

Another interesting set of comparison plots is produced by plotting $k_\parallel$ against the applied bias at a given resistance. For example, Figure 7.4 shows the changes that occur at a pitch of 3.3 Ω as the biased is varied from zero and Figure 7.5 shows similar results at a pitch of 20 Ω. Here, Figure 7.4 is emblematic of the relationships of similar plots for all high pitches and likewise for Figure 7.5 and all low pitches.

The most striking feature of Figure 7.4 is its piecewise linear shape. Between −20 and 10 V $k_\parallel$ varies linearly with applied bias (though an extra measurement at a positive bias value less than 10 V would be useful). Above 10 V and below −20 V $k_\parallel$ "saturates," which is reminiscent of the general bias reduction saturation that occurs near similar bias values (see Section 4.2). Indeed, it appears that the two are correlated at high pitch. While it is easy to speculate that $\Delta n/n$ decreases as $k_\parallel$ is moved from zero and saturates as it reaches a maximum absolute value, this data unfortunately does not indicate whether one of these effects causes the other or whether they both have another cause altogether. Determining this relationship would be interesting future work.

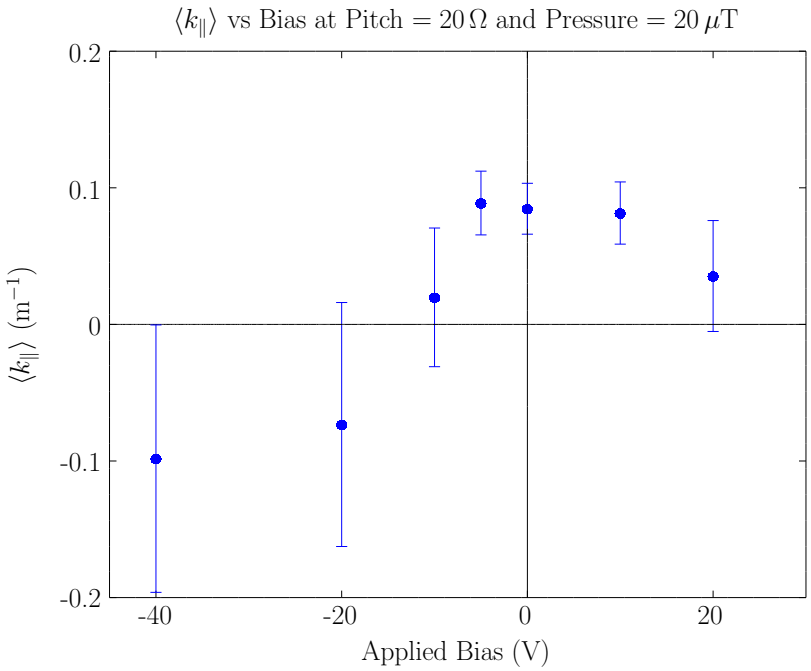

Figure 7.5: Parallel wavenumber at a pitch of 20 Ω versus bias

Figure 7.5, meanwhile, does not display the same linear relationships. Unlike Figure 7.4, which clearly shows that $k_\parallel(\Phi_{bias} = 0) \approx 0$, Figure 7.5 confirms the assertion from Chapter 6 that $k_\parallel(\Phi_{bias} = 0) \neq 0$ at low pitch. The linear relationships are not present and there does not exist similar evidence of $k_\parallel$ saturation. It is clear from the comparison of these two figures that the high and low pitches operate in entirely different regimes. While the exact catalyst of the change cannot be identified, it must be related to the change in pitch, whether it be the actual difference in pitch itself, the magnetic connection length, or the distance (Δz) between the same field line after one transit around the vessel.

It is also worth noting that the changing $k_\parallel$ values produce λ values closer to the physical size of the machine for high pitch (2.7, 3.3, 3.6, 5, and 10 Ω). Table 7.1 shows a comparison of λ and machine size for all pitches at -20 V and $+20$ V.

Whereas λ/L_c can be significantly greater than one for high pitches with grounded plates, with high positive bias the values are all close to two, indicating that one–half of a wavelength fits inside the device (the obvious exception is at 10 Ω, a large outlier). As discussed in Section 6.1, this means that λ reaches its maximum

R (Ω)	λ_{Gnd}	$\lambda_{+20\,V}$	$\lambda_{-20\,V}$	λ_{Gnd}/L_c	$\lambda_{+20\,V}/L_c$	$\lambda_{-20\,V}/L_c$
2.7	444	50.7	24.9	17.6	2.01	0.987
3.3	374	71.3	25.7	12.5	2.37	0.855
3.6	171	77.3	26.6	5.36	2.42	0.831
5	250	122	39.0	5.99	2.92	0.936
10	181	2480	69.5	2.14	29.3	0.820
15	63.4	144	46.6	0.434	0.986	0.319
20	74.2	177	85.7	0.362	0.864	0.418
25	110	184	128	0.307	0.513	0.360

Table 7.1: Comparison of λ and pitch at multiple bias voltages (all λ values are given in meters)

theoretical value but does not surpass it at positive bias, unlike in the grounded case. At strong negative bias λ is approximately equal to L_c, meaning that one full wavelength fits in the device. At lower pitches, despite a few oddities, the values are more constant, as expected, given the more modest effects of bias on $k_\parallel$.

The general, though not exact, agreement of these values at high pitch is likely more than an interesting coincidence and may shed light on the effects that the bias has on the plasma. It is possible, based on the above data, that the bias forces certain boundary conditions at the plates which constrain the formation of larger wavelengths and therefore restrict the growth of the previously identified ideal interchange instability. The difference between positive and negative bias may be related to the different flow patterns that have been observed spectroscopically at different biases [18]. The variations in these flow patterns may cause different wavelengths to be the most unstable at different bias values. Though the exact mechanism by which this could happen is unknown it seems to merit further experimental and theoretical consideration.

The bias may also act in other ways to limit the growth of the interchange instability. While it has been shown that turbulence reduction in the Helimak is not correlated with the increased velocity shear due to the applied bias [20], it remains possible that the bias acts to break up the previously interchange–dominated global flows into smaller "cells" that are then dominated by an instability with shorter wavelength and predictably larger $k_\parallel$. It is certainly possible that a form of an interchange instability still exists, but is rendered invisible by the non–zero $k_\parallel$ components of the other instabilities present.

While the exact explanation may be unclear, it is clear that the bias allows for the growth of instabilities other than the ideal interchange instability and thus changes the turbulent regimes of the Helimak plasma. It is also clear that the application of bias affects the interchange instability at high pitch to a disproportionately higher degree than it does the drift wave present at low pitch. This agrees well with spectroscopic data from the Helimak. This data indicates that the application of bias has a global impact on the plasma. The interchange instability is a global mode, hence it seems reasonable that the global effects of bias would influence it more strongly than the more localized instability drift wave.

7.2 Perpendicular Wavenumber

7.2.1 Low–Field Side

As shown in Figure 7.6, $k_\perp$ becomes messy when negative bias is applied to the LFS. For the radii further out, $k_\perp$ increases with low pitch while for the radii further in it decreases at lower pitch. For the low values of $k_\perp$ at high pitch and large radius the drift wave growth rate is only about 20% of its maximum value while near the radius of the MPD it is considerably larger.

Meanwhile, Figure 7.7 shows that, for the most part, the probes at several radii track each other closely at positive bias with an overall decrease as pitch decreases. Interestingly, the lowest pitches, 20 and 25 Ω, have $k_\perp$ values near 15 m^{-1} which corresponds with drift wave growth rates of less than 10% of the maximum value. Hence, the possibility of drift waves seems to be less important at low pitch and positive bias.

Due to the difficulties of directly comparing the values in Figures 7.6 with those in Figure 6.4, Figure 7.8 shows the difference between the biased value of $k_\perp$ and its grounded value for each bias value at a radius of 1.345 m, close to the location of the MPD. Values of $\Delta k_\perp$ greater than zero indicate that $k_\perp$ increases with the application of bias while values less than zero indicate that $k_\perp$ decreases when bias is applied.

Figure 7.8 then gives a simple indication of the changes in $k_\perp$ with the application of different bias values. It is seen that the highest magnitude negative values, -20 and -40 V, correlate with an increase in $k_\perp$, or a decrease in perpendicular

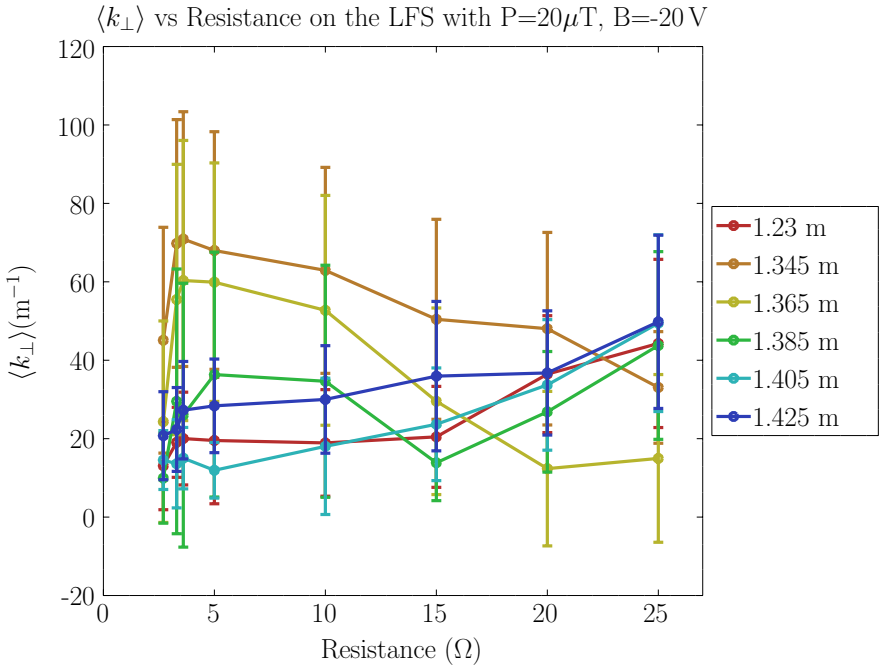

Figure 7.6: Perpendicular wavenumber on the LFS vs resistance at several radii with Bias $= -20$ V and P $= 20\mu$T

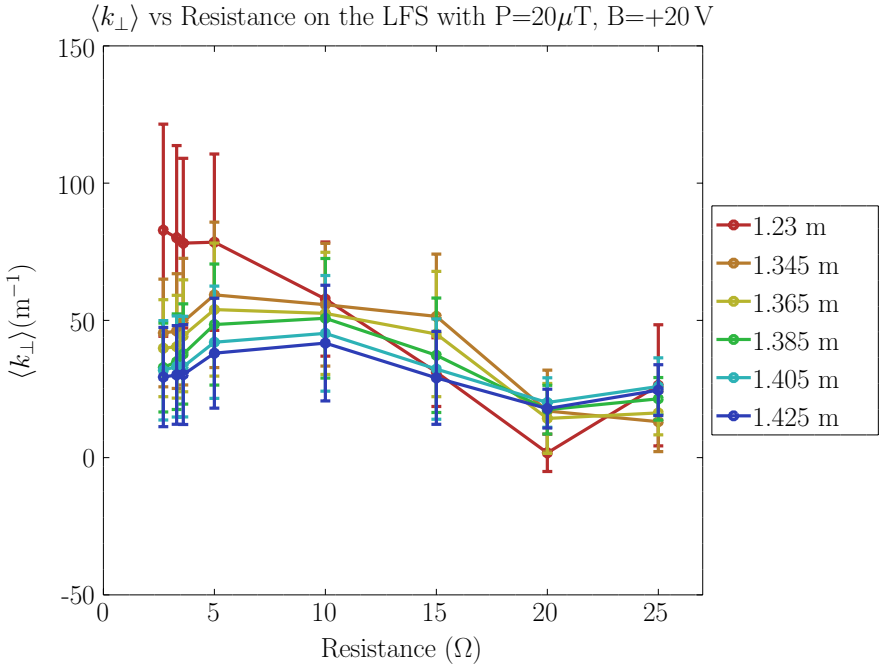

Figure 7.7: Perpendicular wavenumber on the LFS vs resistance at several radii with Bias $= +20$ V and P $= 20\mu$T

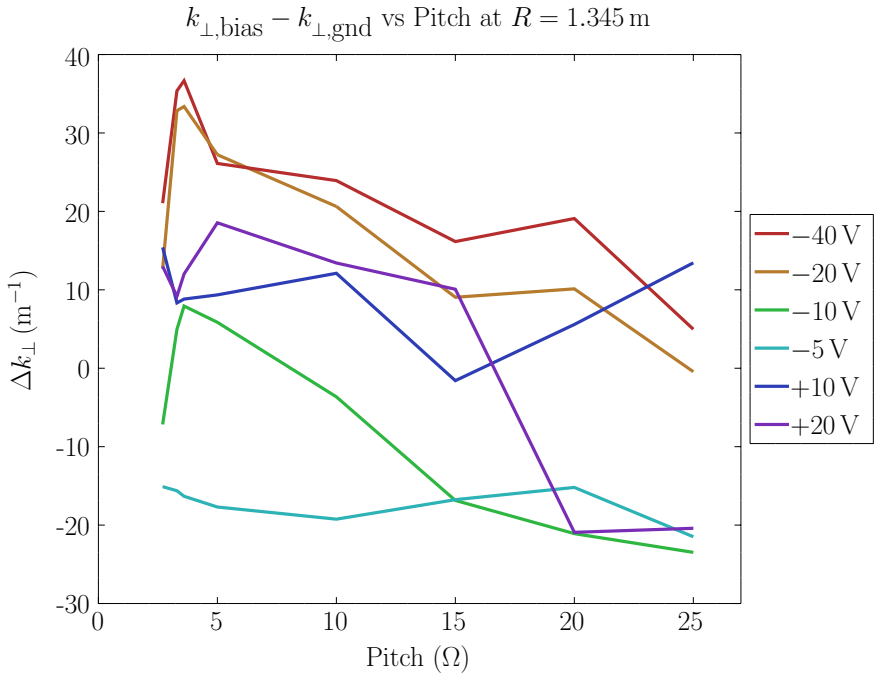

Figure 7.8: Difference between biased and grounded perpendicular wavenumbers on the LFS vs pitch at several radii with P = 20μT

wavelength. Hence, large negative bias is related to a chopping of the perpendicular component of the wave into smaller segments. This wavelength shortening is more impactful at higher pitch where $k_\perp$ increases by a larger amount. The behaviors of the other biases are less consistent. At small magnitude negative values, $-5\,\text{V}$, $k_\perp$ actually decreases compared to ground for all pitches while at the intermediate value, $-10\,\text{V}$, the decrease is clear for low pitch and $k_\perp$ either decreases by a smaller amount or increases at high pitch. A decrease in $k_\perp$ implies an increase in the wavelength of the perpendicular component of the wave. Such an increase is an indication of a wave with larger spatial extent.

The effect of positive bias is also inconsistent. The application of both 10 and 20 V of positive bias is correlated with a small increase in $k_\perp$ at high and medium pitches. At the lowest pitches, however, 20 V of bias actually relates to a decrease in $k_\perp$ while 10 V relates to a further increase. As indicated in the figure, $k_\perp$ is affected by bias. Most bias values, both positive and negative, change $k_\perp$ by between 10 and $20\,\text{m}^{-1}$, which corresponds to a change in $\lambda_\perp$ of between than 0.314 and 0.628 m. Compared with a vertical plasma height of 1.6 m these shifts represent a change of a

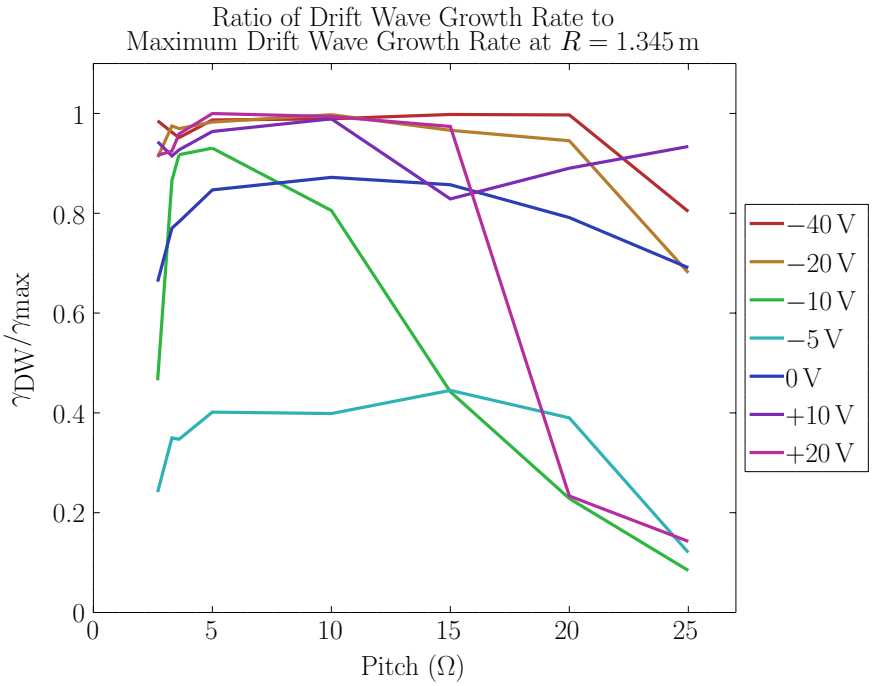

Figure 7.9: Normalized theoretical growth rate of drift waves on the LFS vs pitch at several radii with P = 20μT

substantial fraction of the available space.

As one final test of the effects of the application of bias on the LFS, consider Figure 7.9 which shows the normalized theoretical growth rates of the drift wave as a function of $k_\perp$. This has been calculated from Eq. (3.2.6) by calculating the corresponding curve (shown in Figure 3.4), normalizing its maximum value to one, and then finding the growth rate corresponding to each $k_\perp$ value represented in Figure 7.8. Hence, a value of 1 indicates that the given drift wave growth rate is equal to the maximum, a value of 0.5 indicates that the growth rate is one–half of the maximum, and so forth.

It is seen for most combinations of pitch and bias that the drift wave growth rate is high. This includes in the grounded case. However, as shown in Chapter 6, drift waves do not dominate the plasma in those conditions. At the biased cases, however, with $k_\parallel$ values far from zero at high pitch, the high drift wave growth rates may contribute to a drift wave dominated regime. For some other combinations, particularly at $-5\,\mathrm{V}$ and all pitches, and at $-10\,\mathrm{V}$ and $20\,\mathrm{V}$ at low pitches, the drift wave growth rate is much smaller than its maximum value. While it is still possible,

of course, that drift waves dominate there, it is also possible that the observed effects come from some other instability or combination of instabilities.

7.2.2 High–Field Side

Figures 7.10 and 7.11 show the values of $k_\perp$ on the HFS at the same conditions shown in Figures 7.6 and 7.7 for the LFS.

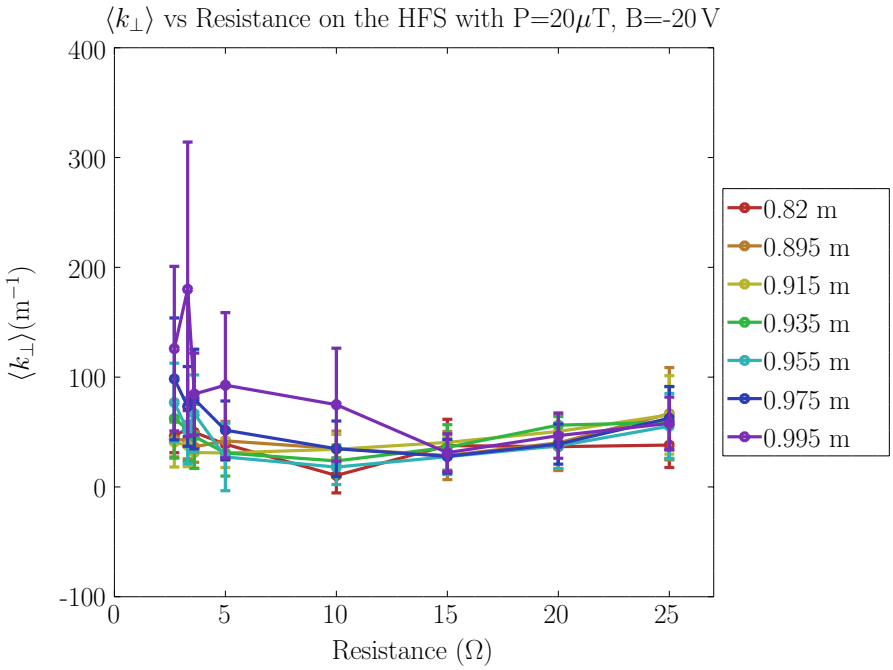

Figure 7.10: Perpendicular wavenumber on the HFS vs resistance at several radii with Bias $= -20$ V and P $= 20\mu$T

As with the LFS, it is helpful to examine a plot of the differences between biased and grounded $k_\perp$ in order to more easily identify the differences when bias is applied. This plot is shown in Figure 7.12.

Compared with Figure 7.8 there are several differences in how $k_\perp$ on the HFS reacts to bias. First of all, Figure 7.12 shows that $k_\perp$ reacts similarly to all of the different negative biases. While not exactly the same, the traces follow one another much more closely than on the LFS. This is likely because the higher magnetic fields mean that the strength of the electric field is less important in determining $\mathbf{E} \times \mathbf{B}$ flows, leading to less variation. The values of $\Delta k_\perp$ are also less variable than on the

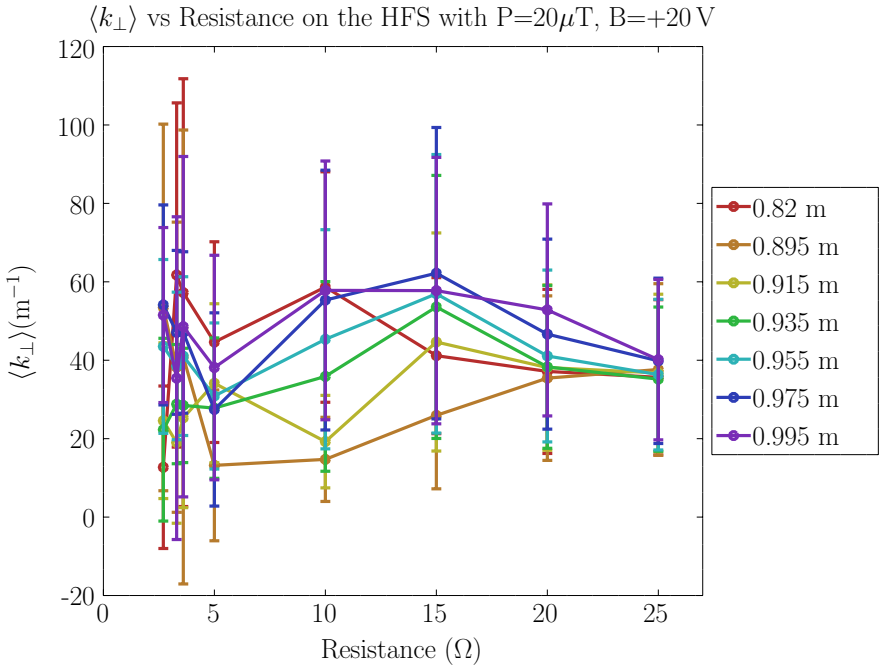

Figure 7.11: Perpendicular wavenumber on the HFS vs resistance at several radii with Bias = +20 V and P = 20μT

LFS for negative bias. In this case, the maximum variation is by about 10 m^{-1} and most of the variation is an increase in $k_\perp$ corresponding to a decrease in $\lambda_\perp$.

The trends for positive bias, meanwhile, do not closely follow either each other or those for negative bias. While scattered, they predominately show a decrease in $k_\perp$ and an increase in $\lambda_\perp$. The shifts only agree with each other at low pitch.

Finally, Figure 7.13 shows the normalized theoretical growth rates of the drift wave on the HFS as a function of $k_\perp$ (similar to Figure 7.9). Overall, the growth rates shown are not as consistently high as on the LFS. For positive bias at high pitch, with the exception of the very highest pitches at 20 V, the growth rates are only a small fraction of their maximum value.

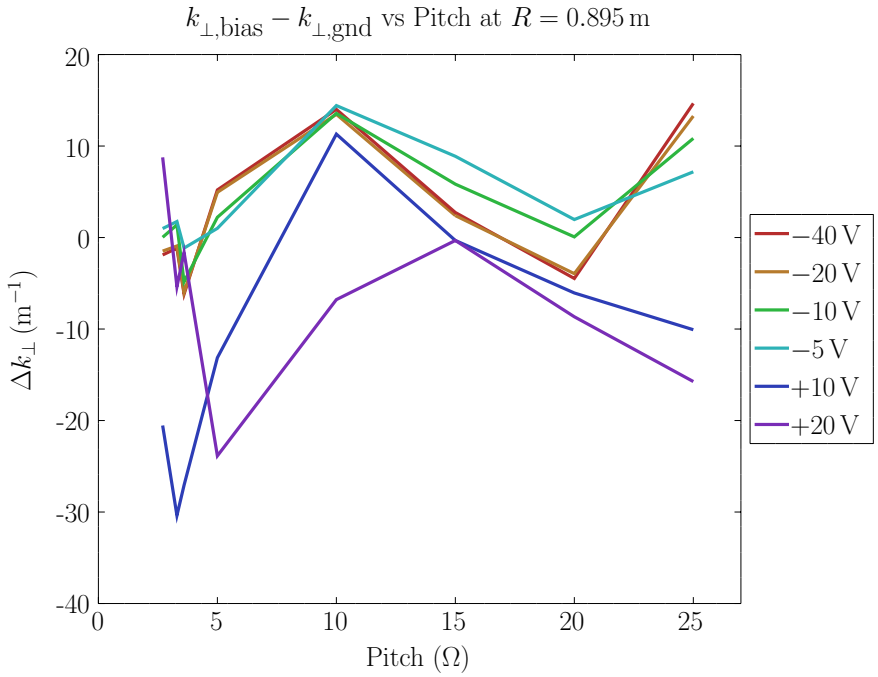

Figure 7.12: Difference between biased and grounded perpendicular wavenumbers on the HFS vs resistance at several radii with P = 20μT

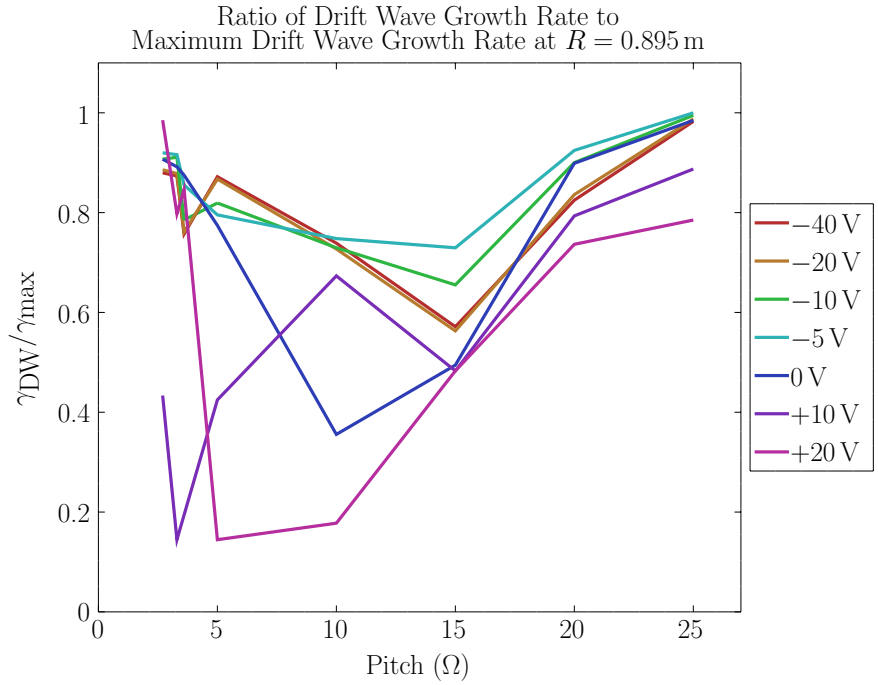

Figure 7.13: Difference between biased and grounded perpendicular wavenumbers on the LFS vs resistance at several radii with P = 20μT

7.3 Power Spectra

The power spectra for the biased cases are revealing. They display wide variation with bias voltage, radius and pitch.

7.3.1 Low–Field Side

On the LFS of the Helimak there is a stark difference in the power spectra from those of the grounded case as discussed in Section 6.3. Here, the 20 μT case will be used as an example because its power spectra are not substantially different than those at other pressures in any of the cases that will be discussed.

The most striking difference between Figure 6.11 from Section 6.3 and Figure 7.14 below is the magnitude of the amplitudes. In the grounded case the power spectrum peak amplitudes were all greater than one and some were as large as five. In the cases with negative bias and in particular the case at $-40\,\mathrm{V}$ shown the magnitude is never greater than 0.5 and often smaller than 0.1. The application of negative bias is thus correlated with a reduction in the power available at all frequencies. Along with the drop in turbulent amplitudes (see Section 4.2) there is a corresponding drop in the power of the turbulent fluctuations, likely due to the same, unknown, mechanism.

Though at lower amplitude, the same shapes and patterns are seen in the strongly negatively biased power spectra ($-20\,\mathrm{V}$ and $-40\,\mathrm{V}$). As with the grounded case there is a small bump that appears at low pitch that then grows in power and becomes the new peak power at high pitch. This growing frequency is shifted to marginally lower frequency than in the grounded case. The appearance of this similar feature is unexpected. If the identification of this peak as an interchange instability is to be believed then it would be expected to disappear when the interchange instability is not longer dominant, as discussed in Section 7.1. The other possibility is that the interchange instability is still present in the biased case but that its power has been incredibly reduced, in agreement with the preceding paragraph. However, one would expect to see the presence of some other mode in the power spectrum that corresponds to the new dominant instability with nonzero $k_{\|}$. No viable options are readily apparent in Figure 7.14.

Adding to the confusion is the fact that at lower magnitudes of negative bias ($-5\,\mathrm{V}$ and $-10\,\mathrm{V}$) the spectra are featureless. They have similar magnitudes to those

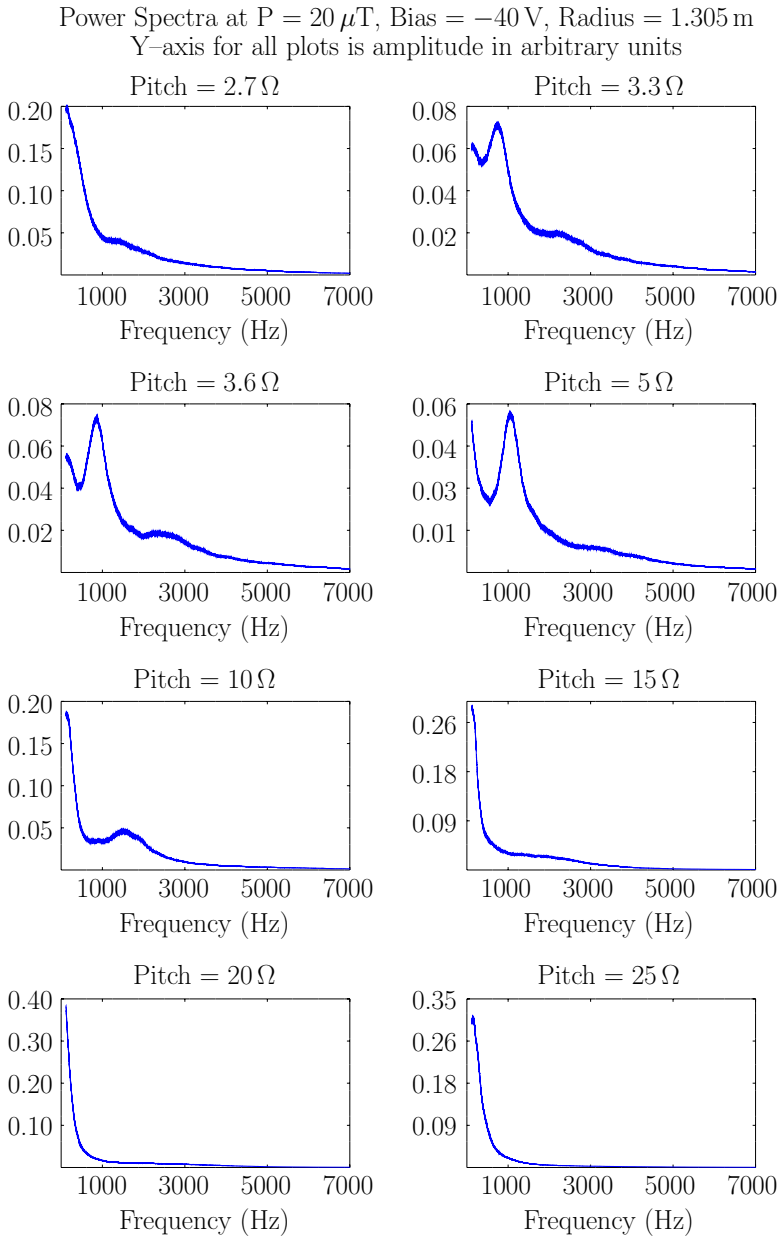

Figure 7.14: Power spectra for all pitches at radius of 1.305 m and P = 20 μT with −40 V of applied bias

at strong bias but without any of the growing and changing peaks. This is especially odd given that these cases experience less bias reduction.

In contrast to the spectra at negative bias those at positive bias show an entirely different character than the grounded case. This can be seen in Figure 7.15, taken at a bias of +10 V. The spectra at +20 V are similar.

Unlike at negative bias, the maximum amplitudes in Figure 7.15 are not substantially reduced. Based on the data presented in Section 4.2, these probes are located near the transition from reduced to amplified turbulent amplitude but remain in a region of reduction. At all pitches the amplitudes are comparable between the positively biased and grounded cases.

The shapes, however, are markedly different at all but the lowest pitches. There is a bump that is first visible at 15 Ω at 6.0 kHz that grows in relative magnitude to become the dominant peak. However, it does not move all the way in towards zero at 2.7 Ω but instead has a frequency of 2.4 kHz at that pitch. This peak is also more dominant than the peaks at negative bias or ground with a magnitude of up to three or four times that of the relatively flat background profile. At the grounded case, for comparison, while the peaks dominant strongly over the power spectrum at high frequency there is always a low frequency exponential background that competes with them for dominance.

The power spectra are affected in some way at positive bias that provides for a similar shifting of frequency maxima at entirely different frequencies. It seems probable that the shifting is due to the same bulk fluid effect identified in the spectral data in Section 6.3 laid over an entirely different instability that does not tend as strongly to zero frequency at high pitch. Hence, these power spectra are more in line with hypothetical expectations that show a change in the dominant mode with the application of bias. Based on the results of Section 7.1 this is almost certainly a mode with much larger $k_{\|}$ than that of an interchange instability, possibly a drift wave.

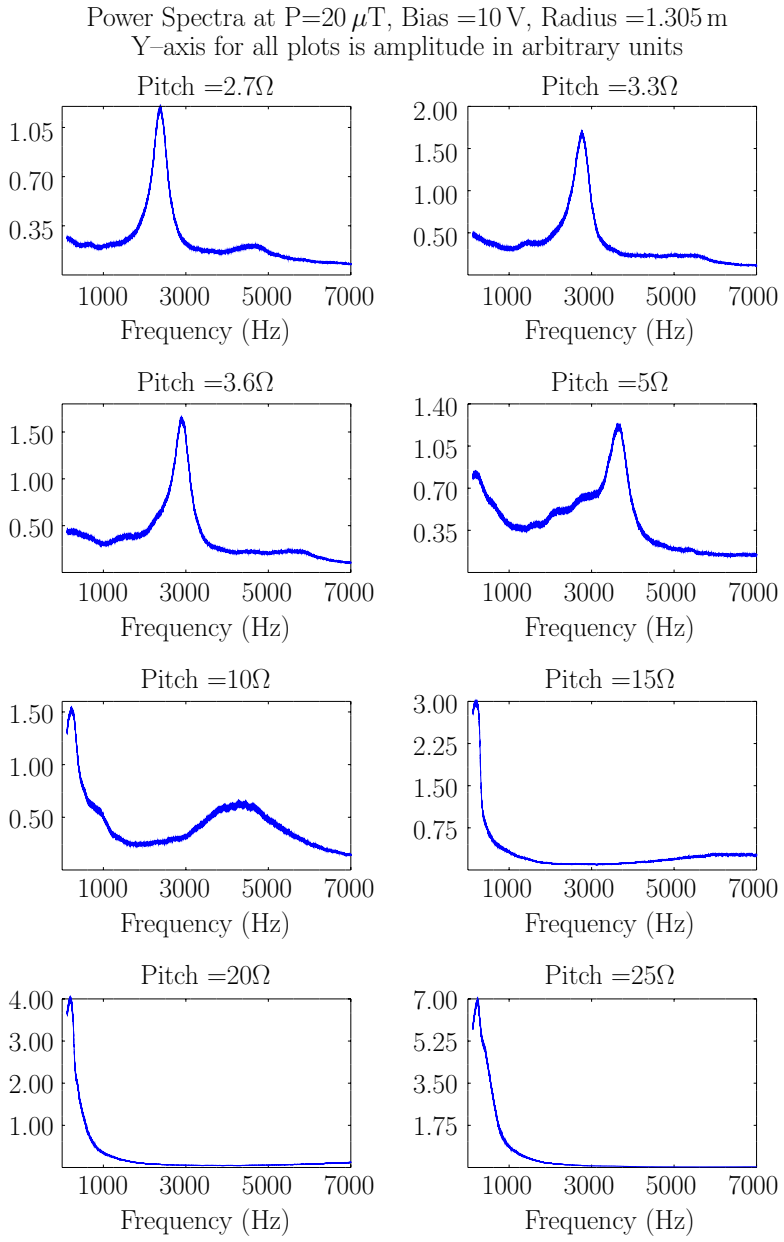

Figure 7.15: Power spectra for all pitches at radius of 1.305 m and P = 20 μT with +10 V of applied bias

7.3.2 High–Field Side

On the high–field side (HFS), the power spectra share some similarities with those presented for the grounded case in Section 6.3. As seen in Figure 7.16, the large peak that was present for low pitches in the grounded case is still present for the slightly negatively biased case, though the spectra themselves are more noisy and show several additional peaks. Again, in all of the cases mentioned below, the spectra at high pitch are relatively featureless.

As the magnitude of the negative bias is increased little changes for the spectra at $20\,\mu$T. The main peak, when present, remains fixed at $\approx 2.5\,$kHz, as seen in Figure 7.16. This is shifted significantly from the grounded case where the major peak occurs at $1.4\,$kHz. This peak is also close to the shifting peak present in Figure 7.14 on the LFS at the highest pitches where it moves in the range of $2.4 - 2.9\,$kHz. Importantly, however, there is almost no power at these pitches and only slightly more at high pitch. Hence, while the plots may be interestingly shaped, practically they reveal almost nothing. While some of the high pitches, which remain featureless, have somewhat more power at different conditions, nowhere is there much power at low pitch.

At positive bias the previously stationary peak shifts outwards to frequencies in the range of $2.8 - 4.3\,$kHz. This is vaguely reminiscent of the behavior on the LFS at positive bias, though the relationship is not as clean. These values are also more dependent on collisionality than the other frequencies reported here. At $40\,\mu$T the frequency peaks fall in the range of $2.1 - 3.0\,$kHz, which provides some of the only evidence of a strong dependence on collisionality seen in these experiments. However, the same caveat applies as to the negatively biased case, namely, there is almost no power in the spectra at low pitch so drawing too many conclusions from the data is not advised.

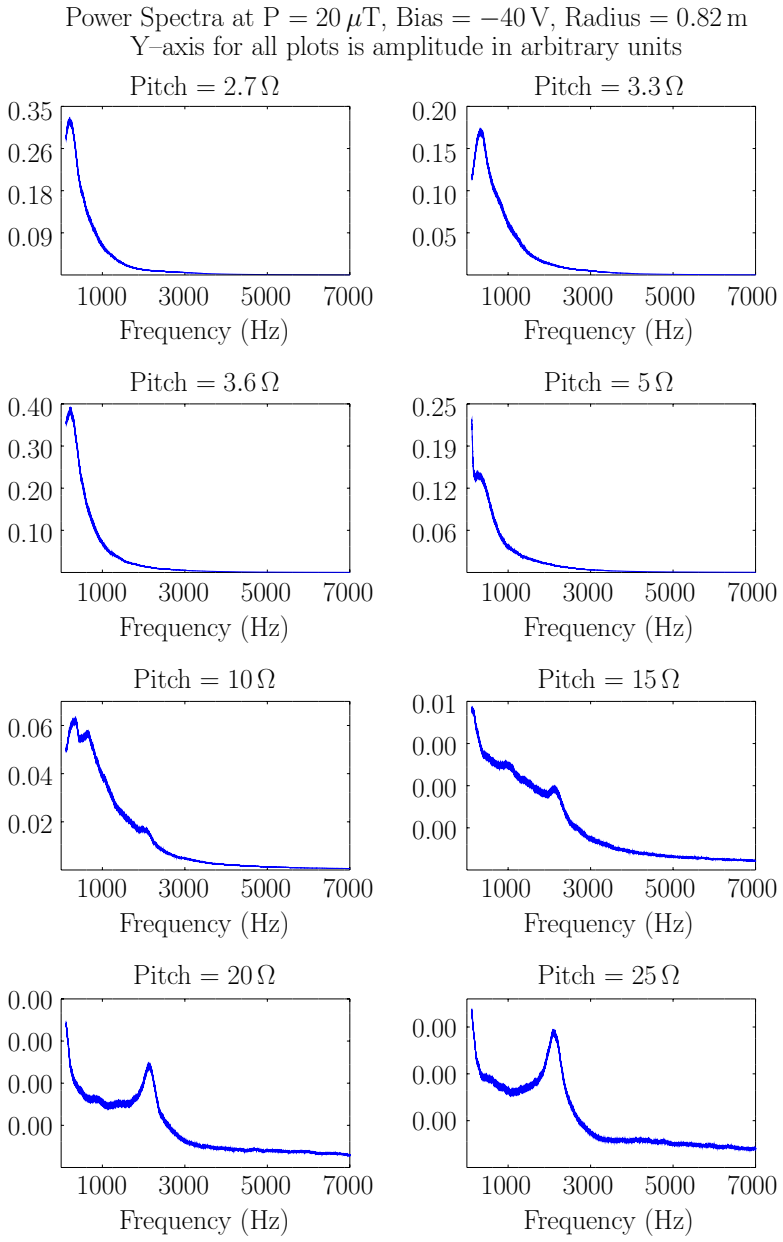

Figure 7.16: Power spectra for all pitches at radius of 0.82 m and P = 20 μT with −40 V of applied bias

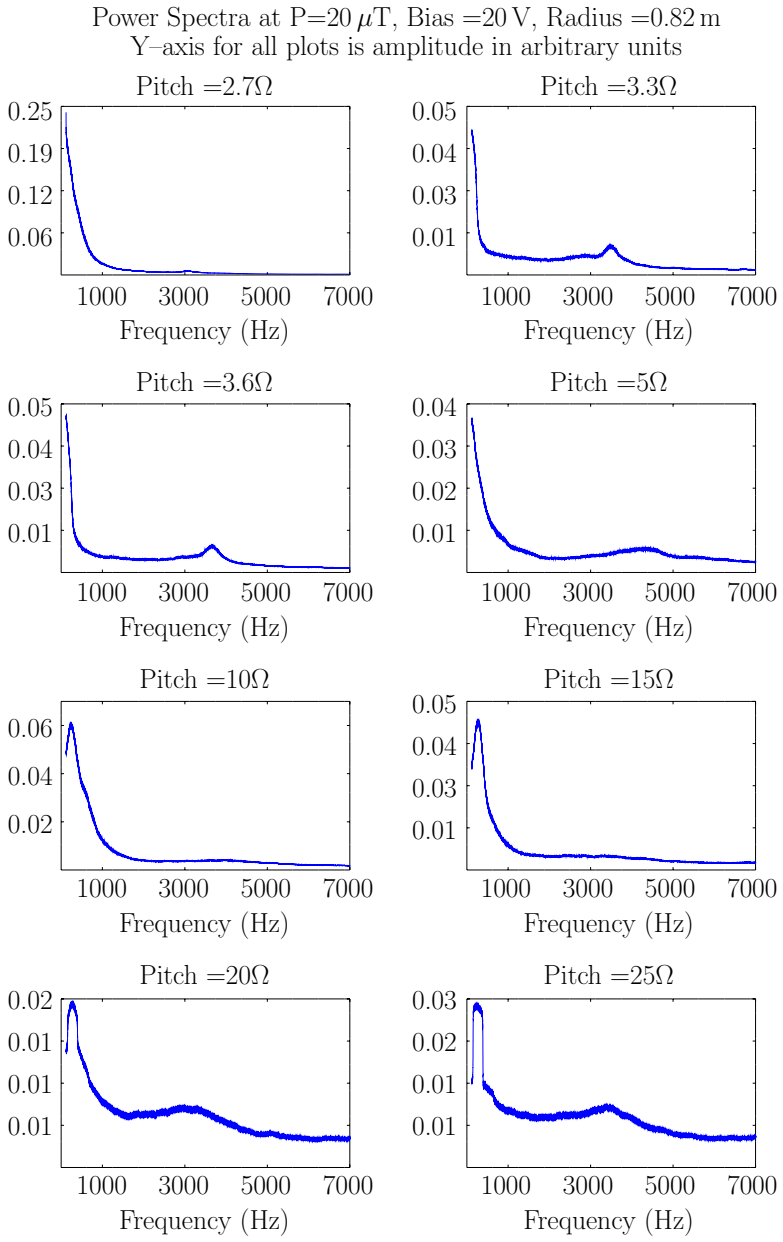

Figure 7.17: Power spectra for all pitches at radius of 0.82 m and P = 20 μT with +20 V of applied bias

7.4 Bicoherence

For the biased cases the bicoherence spectra have generally different forms than those of the grounded case, though often with similar levels of coherence, falling in the range of $0.2 - 0.3$ for the highest peaks. As mentioned in Section 6.4, while not overly high, values in this range are high enough to be theoretically interesting as they imply that some weak coupling is occurring between waves of different frequencies.

Figure 7.18 shows the bicoherence at high pitch and $-40\,\mathrm{V}$ of bias. At smaller magnitudes of negative bias the bicoherence amplitude is twice as strong in the middle region of the spectrum. As the magnitude of the bias is increased those amplitudes decrease, leaving only high regions near the edges of Figure 7.18. This bicoherence spectrum lacks the region of high correlation below 500 Hz and has replace it with a relatively high region between 1 and 2 kHz and 0. Figure 7.14 indeed shows relatively high power peaks at both 0 and 1.1 kHz. While these power spectra have exceptionally low amplitudes, it appears that what little power does occur there is the result of weak coupling of the two largest frequency peaks. These results are interesting to compare with the grounded case, Figure 6.12. In this case, it appear that the higher coupling of frequencies near the origin has spread to higher frequencies through the addition of negative bias.

As seen in Figure 7.19, the bicoherence is nearly empty at extreme negative bias and low pitch. This represents a complete change from the grounded case at low pitch, shown in Figure 6.13. The previously high coupling between 500 Hz and all frequencies has been pushed to the edges and now appear as a less–widespread coupling between some frequencies and zero. The medium–high values near near 4.5 kHz and 500 Hz are actually higher at lower magnitudes of negative bias but become less important as the bias magnitude is increased. However, no comparable changes are seen in the power spectra, perhaps because of the low power levels at high frequency. The high peak near the origin, however, is visible as the only peak in the corresponding subplot of Figure 7.14.

The bicoherence spectra at positive bias are conceivably more interesting due to the higher power levels present in Figure 7.15. Indeed, Figure 7.20, while at $+20\,\mathrm{V}$ instead of $+10\,\mathrm{V}$, can be favorably compared with Figure 7.15 (the choice was made to use $+10\,\mathrm{V}$ for the power spectra because the traces were cleaner and more readable while still showing the same features as the spectra at $+20\,\mathrm{V}$). Figure 7.20 shows weak

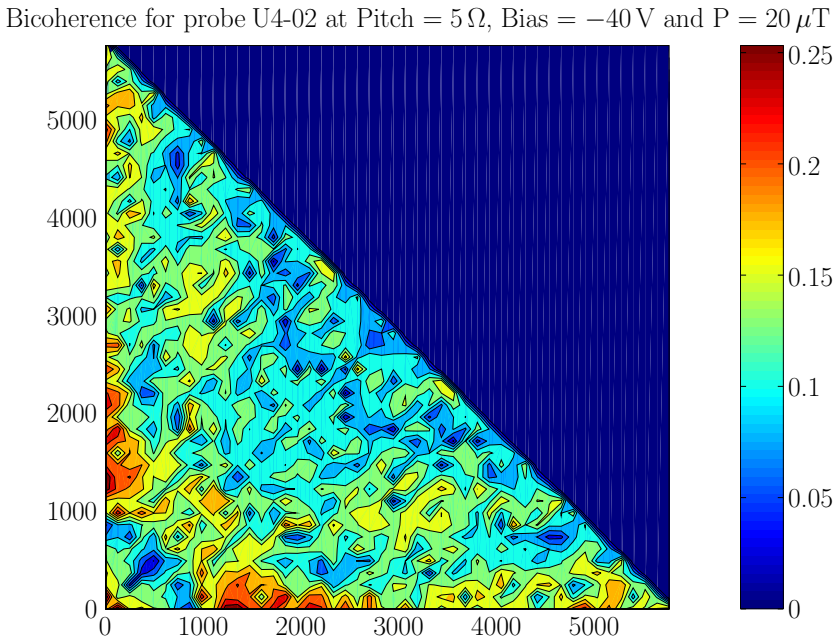

Figure 7.18: Bicoherence for a pitch of $5\,\Omega$ at $20\,\mu$T with $-40\,$V of bias.

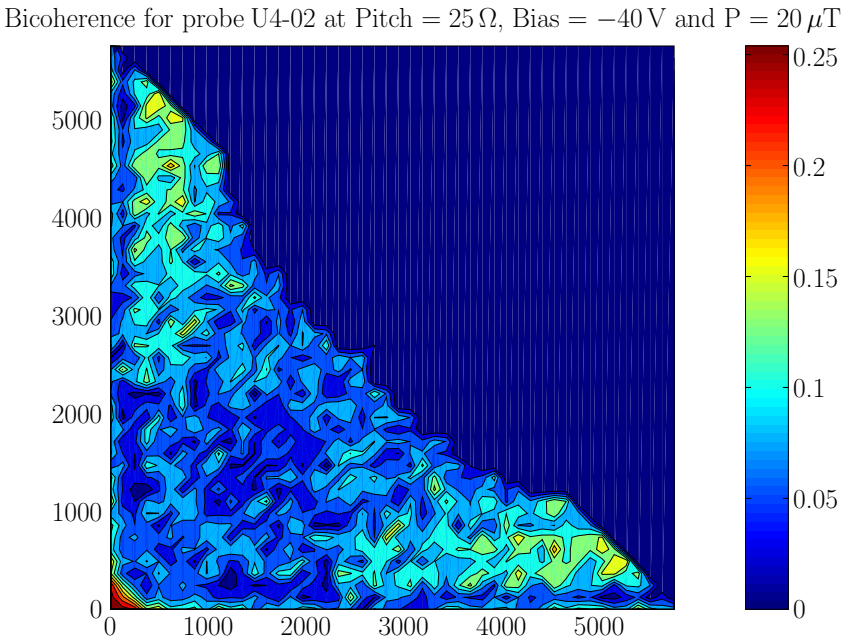

Figure 7.19: Bicoherence for a pitch of $25\,\Omega$ at $20\,\mu$T with $-40\,$V of bias.

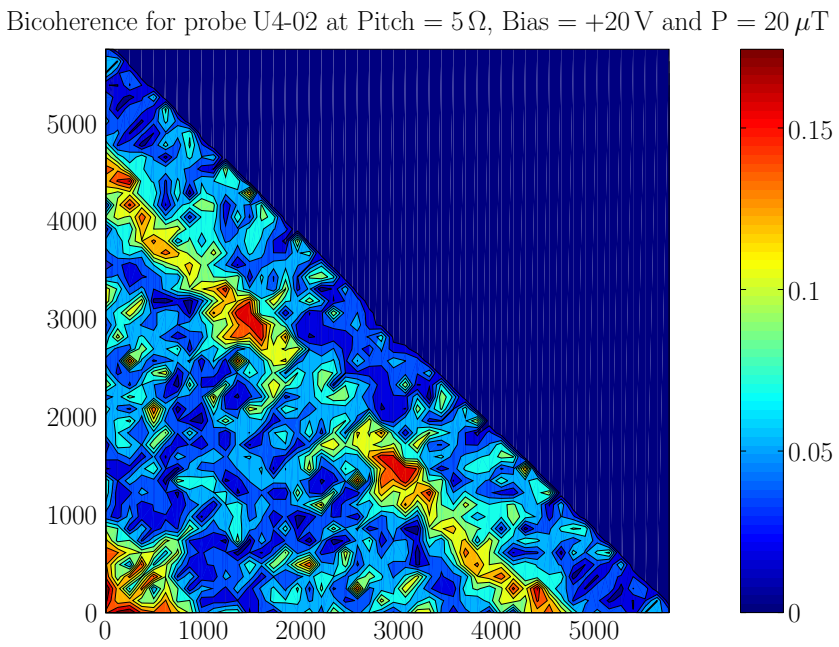

Figure 7.20: Bicoherence for a pitch of 5 Ω at 20 μT with +20 V of bias.

coupling for a range of frequencies that add to 4.5 kHz. The strongest set of additive frequencies is at 3.0 kHz and 1.5 kHz. The largest peak in the power spectrum occurs at 3.7 kHz, though there are smaller subpeaks visible at numerous smaller frequencies. It seems that there is certainly weak coupling going on between the frequencies at positive bias and high pitch which possibly contribute to the growth of the dominant frequency. As discussed in the previous section, this frequency is unusual for several reasons and may represent a different instability than those previously identified. Figure 7.20 also shows the common high coherence values near the origin, though in this case the relatively high amplitudes extend out from zero to nearly 1 kHz, which may be related to the relative broadness of the low frequency peak in Figure 7.15. This figure also, like Figure 7.18 at high pitch and negative bias, shows a transformation from the grounded case, Figure 6.12.

At positive bias and low pitch, Figure 7.21 shows the highest bicoherence amplitudes in this work with values above 40%. However, these high amplitudes are extremely limited in their range of applicability, appearing only near the origin and at the intersection of slightly positive values with the range $4.5-5.5$ kHz. Comparison

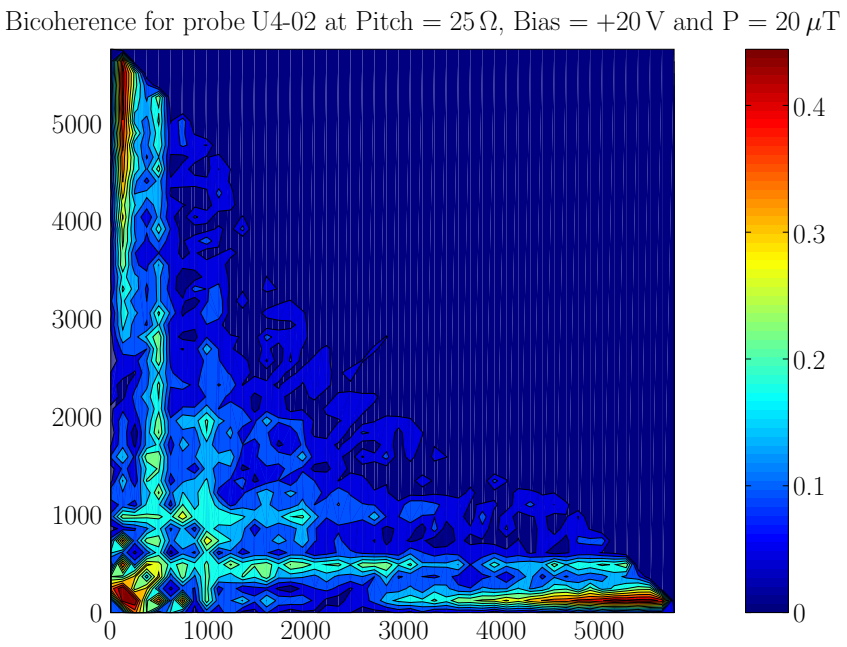

Figure 7.21: Bicoherence for a pitch of 25 Ω at 20 μT with +20 V of bias.

with Figure 7.15 show that the only significant power is near the origin, as frequencies of less than 1 kHz. This figure also shows some of the same characteristics as Figure 7.19, namely high bicoherence near the origin and thin bands along the axes. It is interesting that the two bicoherence spectra at low pitch share more in common than the two at high pitch (Figures 7.18 and 7.20). This seems to be an indication that the coupling, and hence the mechanisms of power sharing between instabilities of different frequencies, are less variable with bias at low pitch than at high pitch. This is in line with previous observations, especially of $k_{\|}$, that the high pitches are more affected by bias than are the low pitches.

Chapter 8

Conclusion

As most of the conclusions that this work has to offer have already been supplied in their respective sections, this final chapter will serve to gather those conclusions into one place before making several summary remarks. This chapter will also contain brief descriptions of interesting follow–up experiments that could be completed in the off chance that this dissertation falls into the hands of any future Helimak graduate students.

8.1 Concluding Remarks

One of the purposes of this dissertation was to answer the question of which instabilities dominate in the Helimak plasma. Various articles in the literature throughout the years, both those dealing directly with the Helimak and those more closely aligned with similar devices, have theoretically disagreed on the exact nature of the instabilities. Other articles have dealt more closely with the way the instabilities and turbulence actually behave without giving deference to their provenance. While these have all been worthwhile and exceedingly interesting efforts, this dissertation has been written under the following two assumptions: 1) Experimental work, coupled with appeals to theory and simulation, is better adapted to answer the question of instability dominance than either theory or simulation on their own and 2) Knowledge of the exact nature of the instabilities, one may say "putting a name to a face," can only help and not hurt in the attempts to mitigate and understand said instabilities.

To answer, then, the question at the heart of this work, it has been shown in Chapter 6 that two distinct instability regimes exist when the bias plates are grounded. As most clearly depicted in Figure 6.1 and Table 6.1, at high pitch, defined in this case at 2.7, 3.3, 3.6, 5, and $10\,\Omega$, the values of $k_{\|}$ are, within reasonable experimental error, equal to zero. The modes have wavelengths much longer than the size of the device and thus constitute a close experimental approximation to the theoretical ideal interchange mode. This result couples well with the the power spectra shown in Section 6.3. The patterns of frequency peaks in these spectra compare favorable with spectroscopic data to indicate that this instability is moving in concert

with the bulk plasma. This is an additional indication that the ideal interchange mode dominates at these pitches.

For lower pitches, given by 15, 20, and 25 Ω, the measured values of $k_{\|}$ in Figure 6.1 and Table 6.1 are clearly nonzero. Their spectra also behave, in general, quite differently, leading to the conclusion that some other mode dominates at low pitch.

These results agree well with theoretical and computational work by Ricci and Rogers as discussed in Section 3.3, which posited that the ideal interchange mode would dominate at high pitch and that drift waves would dominate at low pitch with the resistive interchange instability playing no part in the Helimak. With this theoretical background, it seems plausible to conclude that drift waves dominate the Helimak plasma at the low pitches mentioned above.

When bias is applied the results change considerably. As shown in Chapter 7, in particular Figures 7.2 and 7.3, it is obvious that the previously discussed relationships do not hold. First and foremost, in the regions of interest negative bias leads to turbulent reduction (Section 4.2.2), while positive bias leads to some reduction and some amplification. This is seen in the power spectra in Section 7.3 in which the amplitudes are greatly reduced from the grounded case. The profiles are also strongly affected by bias (see Section 4.1). Indeed, an average decrease in the magnitude of the density gradient may be partially responsible for the reduction of turbulence.

While the values of $k_{\|}$ change only slightly for bias as low pitch, the corresponding values at high pitch change by extraordinary amounts and clearly no longer equal zero. Thus, it appears that the ideal interchange instability is destroyed with the application of bias. It is also clear that the application of bias does not affect all pitches equally. The fact that the low pitches maintain a relatively constant $k_{\|}$ seems to indicate that whatever effect the bias has on the plasma does not act to eliminate drift waves, though a study of the turbulent amplitudes shows that it can reduce their magnitude. The nature of the instability, however, does not appear to have changed substantially.

An interesting side effect of the bias is shown in Table 7.1 where it is revealed that bias limits the instability wavelengths at high pitch to either once or twice the value of the magnetic connection length. Not only does this represent an extreme shortening of the wavelength, but it also appears that bias fixes some sort of sheath

boundary condition on the plasma, though the mechanism is not currently known. With the wavelength bounded it is not free to grow large enough for the ideal interchange mode to take over. Hence, while it is possible that a drift wave has taken over, it seems more likely that a sort of "pseudo" interchange instability dominates. This "pseudo" interchange mode does not have a long enough wavelength to yield an effectively zero value for $k_{\|}$, but does grow to fill the size made available to it by the newly–imposed boundary conditions. This hypothesis is support by the power spectra at negative bias which shows a similar shape and patter to those for the grounded case. The addition of positive bias, on the other hand, appears to fundamentally change the nature of the turbulence. New peaks arise in the power spectra which may indicate a different instability.

This data is summarized in Figure 8.1, which shows a contour plot of the value of $k_{\|}$ under all conditions at $20\,\mu$T of pressure. The applied bias is shown on the x axis and the pitch on the y axis. The pitch, while labeled with the usual resistance values, has those values spaced according to the value of centimeters per revolution that each of those pitches implies at the radius of the MPD (see Appendix A). Here, all values of $k_{\|}$ for which zero falls within the error bars have been binned as exactly zero so that the patterns may be more readily seen.

The remaining questions on this front is clear: What causes the shift in regime? Why does the plasma behavior differ based on the pitch of the magnetic field lines? While no exact answer is to be forthcoming from this work, there are scattered pieces of evidence that may, with additional work, form a coherent picture. In Chapter 4 it was clearly shown that even the basic profiles of ion density, electron temperature, and floating potential vary with pitch under certain conditions. If nearly all quantities vary with this one parameter there must be something fundamentally important about the pitch. There are several different but equivalent ways to consider the pitch in the machine. One is to simply think of it as the complement of the angle at which the field lines strike the probe plates. This view seems the least useful here. Another is to consider the pitch as the magnetic connection length. High pitch is then related to short connection length and vice versa. However, it has been abundantly shown that the correlation lengths along field lines are not a substantially large percentage of the total magnetic connection length.

Hence, the view of the pitch that may be most interesting here is that it

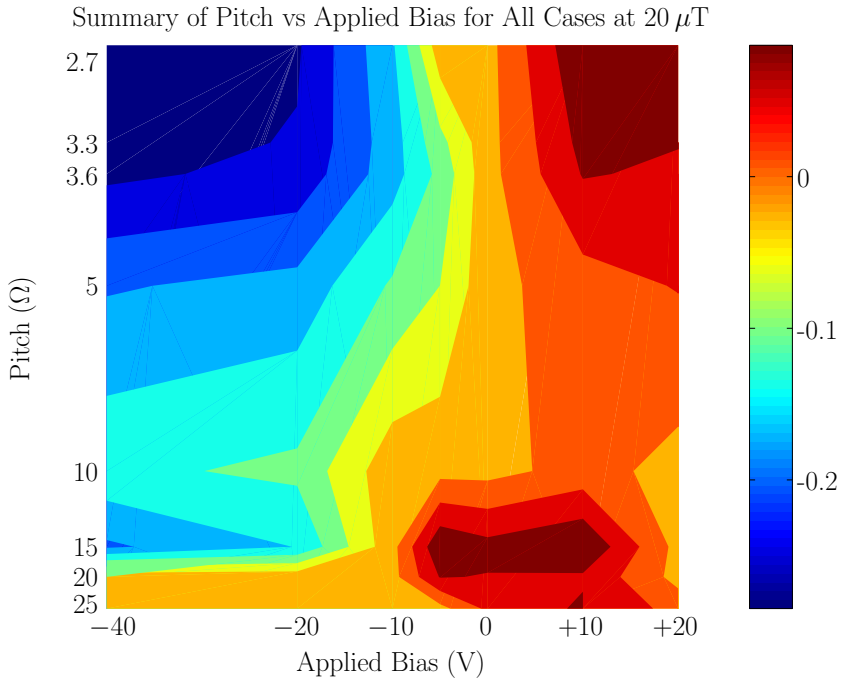

Figure 8.1: Turbulent amplitudes in the grounded case

represents the distance, Δz between one field line and itself after that field line has completed one circuit around the vacuum vessel. In this sense, high pitch represents a large gap between the field line and itself while lower the pitch results in "squeezing" the magnetic field line against itself. It is interesting to note that the regime shift occurs right as Δz approaches ρ_s, the Larmor radius at the sound speed. It seems probable that the shift in regime is caused by the increased ability of the plasma at these pitches to jump across the field from one line to the next. This may enable higher levels of transport that can disrupt the wavenumbers of the instabilities.

In this regard, more work is needed, experimentally, theoretically, and computationally to understand the behaviors of the plasma in these conditions.

8.2 Future Work

As any guest to the Helimak has noticed, the Helimak vacuum vessel has more blank ports than ports currently in use. There are myriad experiments that can and will be attempted on the device. Thus, this list is not meant to be exhaustive. It mentions only a few of the experiments related to the present work that could shed

additional light on question of turbulent regimes and their effects in Helimak plasmas.

- An expansion of the collaborative experiments currently being undertaken with West Virginia University will allow for direct measurement of the plasma potential (see Section 2.2). This will allow for accurate measurement of the transport parameters in the device, which can shed light on the instabilities causing the transport.

- Previous work has established a connection between the interchange instability and blobs [21]. Confirmation of the extensive of blob–like structures in the Helimak may be able to strengthen the conclusions about the dominance of the interchange instability in the device.

- Spectroscopic measurements at larger radius and a more comprehensive parameter scan will be useful in examining the bulk flow patterns and relating them to the data seen in the power spectra presented in Chapters 6 and 7.

Appendix A

Table of Pitches and Radii

This appendix provides tables relating the pitch resistances to both the actual magnetic field line pitches in units of centimeters per revolution and to the magnetic connection lengths, in units of meters. This has been done for increments of ten centimeters across the radius of the device, at all pitches used in this work.

	Radius (m)							
R (Ω)	0.7	0.8	0.9	1.0	1.1	1.2	1.3	1.4
2.7	13.9	18.2	23.0	28.4	34.3	40.8	47.9	55.6
3.3	11.7	15.2	19.3	23.8	28.8	34.3	40.2	46.7
3.6	10.9	14.3	18.1	22.3	27.0	32.2	37.8	43.8
5	8.4	11.0	13.9	17.1	20.7	24.7	29.0	33.6
10	4.1	5.4	6.8	8.4	10.2	12.1	14.2	16.5
15	2.4	3.1	4.0	4.9	5.9	7.0	8.3	9.6
20	1.7	2.2	2.8	3.5	4.2	5.0	5.9	6.8
25	1.0	1.3	1.6	2.0	2.4	2.9	3.4	3.9

Table A.1: Pitch values in centimeters per revolution for all pitches and a collection of radii

	Radius (m)							
R (Ω)	0.7	0.8	0.9	1.0	1.1	1.2	1.3	1.4
2.7	46.5	40.7	36.2	32.6	29.6	27.1	25.1	23.3
3.3	55.4	48.5	43.1	38.8	35.3	32.3	29.8	27.7
3.6	59.1	51.7	46.0	41.4	37.6	34.5	31.8	29.5
5	77.0	67.4	59.9	54.0	49.0	44.9	41.5	38.5
10	157	137	122	110	99.6	91.3	84.3	78.3
15	270	236	210	189	172	157	145	135
20	379	332	295	265	241	221	204	190
25	662	579	515	463	421	386	356	331

Table A.2: Magnetic connection length, L_c, in meters for all pitches and a collection of radii

Bibliography

[1]J. Wesson, *Tokamaks*, 4th ed. (Oxford University Press, 2011).

[2]K. Gentle, and H. He, "Texas helimak", Plasma Science and Technology **10** (2008).

[3]J. C. Perez, W. Horton, K. Gentle, W. Rowan, K. Lee, and R. Dahlburg, "Drift wave instability in the helimak experiment", Phys. Plasmas **13**, 032101 (2006).

[4]S. Luckhart, *The helimak: a one dimensional toroidal plasma system*, tech. rep. UCSD-ENG-069 (University of California, San Diego, 1998).

[5]P. Ricci, and B. Rogers, "Transport scaling in interchange-driven toroidal plasmas", Phys. Plasmas **16**, 062303 (2009).

[6]B. Li, B. Rogers, P. Ricci, and K. Gentle, "Plasma transport and turbulence in the helimak: simulation and experiment", Phys. Plasmas **16**, 082510 (2009).

[7]B. Li, B. Rogers, P. Ricci, K. Gentle, and A. Bhattacharjee, "Turbulence and bias-induced flows in simple magnetized toroidal plasmas", Phys. Rev. E **83**, 056406 (2011).

[8]P. Ricci, and B. Rogers, "Turbulence phase spaced in simple magnetized toroidal plasmas", Phys. Rev. Let. **104**, 145001 (2010).

[9]K. Gentle, *Helimak plasma*, Helimak laboratory internal Excel spreedsheet.

[10]P. M. Bellan, *Fundamentals of plasma physics* (Cambridge, 2006).

[11]R. L. Merlino, "Understanding langmuir probe current-voltage characteristics", Am. J. Phys. **75** (2007).

[12]N. Hershkowitz, "How langmuir probes work", in *Plasma diagnostics*, Vol. 1, edited by O. Auciello, (Academic Press, Inc, Cambridge, 1989) Chap. 3, pp. 113–183.

[13]K. Lee, "Experimental characterization of drift-wave experimental characterization of drift-wave turbulence in the sheared, cylindrical slab", PhD thesis (The University of Texas at Austin, 2009).

[14]Y. Kim, and E. Powers, "Digital bispectral analysis and its applications to nonlinear wave interactions", IEEE Transactions on Plasma Science **PS-7** (1979).

[15]F. F. Chen, *Introduction to plasma physics and controlled fusion*, 2nd ed., Vol. 1 (Springer, 2006).

[16]F. Poli, P. Ricci, A. Fasoli, and M. Podestà, "Transition from drift to interchange instabilities in an open magnetic field line configuration", Phys. Plasmas **15**, 032104 (2008).

[17]D. Jassby, "Transverse velocity shear instabilities within a magnetically confined plasma", Physics of Fluids **15** (1972).

[18]W. Rowan, K. Gentle, C. Williams, M. Brookman, and K. Liao, "Comparison of turbulence reduction with flow velocity shear in a simple magnetic configuration, the helimak", In prep.

[19]L. Gramer, *Kelvin–helmholtz instabilities*, `https://www.rsmas.miami.edu/users/isavelyev/GFD-2/KH-I.pdf` (visited on 03/09/2017).

[20]K. Gentle, W. Rowan, C. Williams, and M. Brookman, "Turbulence in the cylindrical slab", Phys. Plasmas **21**, 092302 (2014).

[21]P. Zhu, C. Sovinec, and C. Hegna, "The formation of blobs from a pure interchange process", Physics of Plasmas **22**, 022311 (2015).

Vita

Chad Blaine Williams was born in Austin, Texas in 1988 to Clark and Melissa Williams while Clark was a Ph.D. student in the chemical engineering department at UT. After growing up in Charleston, West Virginia, he graduated from Cinco Ranch High School in Katy, Texas, in 2006. Following his freshman year at Brigham Young University in Provo, Utah, he spent two years as a full–time missionary for the Church of Jesus Christ of Latter–day Saints in Milan, Italy. Two more years at BYU and a wedding to the former Leilani Wight later he enrolled in the Ph.D. program in physics at the University of Texas at Austin in August, 2011. He began working with Dr. Kenneth Gentle on basic plasma physics research during his second semester and never looked back. In March, 2016 he and Leilani welcomed their son, Faraday Williams, into the world.

Address: chad.blaine.williams@gmail.com

This dissertation was typed by the author.